Functional polymers with embedded nanoparticles

Henrik Mauroy

Thesis submitted for the degree of
Philosophiae Doctor

Department of Physics
University of Oslo

June 2013

Series of dissertations submitted to the
Faculty of Mathematics and Natural Sciences, University of Oslo
No. 1395

ISSN 1501-7710

Cover: Inger Sandved Anfinsen.
Printed in Norway: AIT Oslo AS.

Produced in co-operation with Akademika Publishing.
The thesis is produced by Akademika Publishing merely in connection with the thesis defence. Kindly direct all inquiries regarding the thesis to the copyright holder or the unit which grants the doctorate.

Abstract

The present thesis presents experimental work on functional polymers with embedded nanoparticles. The work was specifically aimed at synthesizing and characterizing anisotropic bulk polymer-clay nanocomposites (PCNs) with aligned clay nanoparticles, and is divided into two main parts:

Nanocomposite hydrogels (NC-gels)

The poly(N-isopropylacrylamide)/Laponte-clay nanocomposite hydrogel (NC-gel) is a type of hydrogel where the polymer network is cross-linked by Laponite clay nanoparticles instead of organic cross-links. In this work a preliminary study on the feasibility of using external electric fields to induce alignment of the Laponite nanoparticles, in such an NC-gel, was conducted. We concluded that electric field alignment was highly inefficient on this system since it contained around 90 % water. Due to the high dielectric constant of water the alignment persisted only for a few microseconds.

During the work on the NC-gels a highly interesting phenomenon was discovered when small fractions of oxygen was allowed to come in contact with the reaction mixture while it polymerized. Complex interactions among clay, oxygen and the polymer were found to induce phase segregation of the mixture, into one polymer-rich and one polymer-deficient water-clay phase. This work is presented in Paper I.

Synthesis of a new type of ferro-NC-gels (FNC-gels) with embedded magnetic nanoparticles was performed. A detailed in situ small angle x-ray scattering (SAXS) study of both the NC-gels and FNC-gels was conducted to find evidence of structural anisotropy when the gels were synthesized inside magnetic fields. A study of a photopolymerization synthesis of the NC- and FNC-gels was also conducted, using riboflavin-5'-phosphate (R5P) as the initiator. With this we tried to find a simple setup for use during in situ SAXS studies that could replace the temperature induced free-radical polymerization technique we already employed, which used potassium peroxodisulphate (KPS) as initiator. The resulting photopolymerized gels showed inferior mechanical properties compared to the ones produced using KPS as initiator, and due to this we decided not to develop the synthesis further.

Solid PCNs

By incorporating clay nanoparticles in polymers large improvements in thermal and mechanical properties can be achieved, compared to the polymer alone, if the clay is well-dispersed in the polymer matrix. In this work a range of surface modified clays and solid polymer-clay samples were synthesized and carefully analyzed using different techniques. Several interesting findings from this work are presented in Paper II, Paper III and Paper IV. First of all, an almost linear correlation between the amount of clay surface charge, and the quantity of surfactant that each clay could incorporate, was established. The surface charge of the clays further proved to indirectly determine the level of improvements in high temperature resilience, and the extent of dispersion of the clay. Lower surface charge was seen to lead to increased dispersion of clay in polystyrene-clay nanocomposites (PSNCs), which resulted in larger improvements in thermal properties. The exact opposite, however, was seen in nylon 6/clay nanocomposites (N6NCs). In these materials both thermal and mechanical properties showed the largest improvements when the surface charge was high. The mechanical properties of the PSNCs, on the other hand, were inferior to pure polystyrene, but interestingly a low surface charge induced the least reduction.

In situ heating studies of dispersions of clay in liquid styrene (the monomer of polystyrene) indicated that almost full exfoliation prior to polymerization could be achieved when the surface charge was low.

Electric field guided self-assembly was utilized to align the clay nanoparticles into long chain-like structures during synthesis, for production of anisotropic polystyrene-clay nanocomposites. Wide angle x-ray scattering, x-ray computed microtomography, and optical microscopy were used to determine the microstructure of both aligned and non-aligned samples. This self-assembly technique was, however, not compatible with the nylon 6/clay nanocomposites. The reason for this was investigated further and was concluded to be related to a large increase in the dielectric constant of ε-caprolactam (the monomer of nylon 6) as it was melted. When this occurred the dielectric constant became higher than for the clay particles, and polarization of the clay particles could thus not take place.

Sammendrag

Denne avhandlingen beskriver mitt arbeid for Ph.D. graden ved Fysisk institutt ved Universitetet i Oslo. Det eksperimentelle arbeidet ble utført under veiledning av professor Kenneth D. Knudsen og professor Geir Helgesen, ved Fysikkavdelingen ved Institutt for energiteknikk (IFE), Kjeller, i perioden mellom august 2009 og oktober 2012. Arbeidet ble finansiert av Norges forskningsråd gjennom FRINAT prosjektet 191564/V39.

Målsettingen var å syntetisere og karakterisere anisotropiske polymer-leire-nanokompositter (PCNS) der leirepartiklene ble opplinjert til kjeder ved hjelp av eksterne elektriske eller magnetiske felt. Det ble jobbet med to forskjellige typer nanocompositter. Den første typen var myke vannabsorberende hydrogels der polymerkjedene var kryssbundet av Laponitt-leirepartikler i stedet for organiske molekyler. Vi oppdaget under dette arbeidet at når små mengder oksygen var til stede under polymerisering segregerte prøvene til en polymerrik og en polymerfattig fase. Årsaken til dette var komplekse interaksjoner mellom leire, oksygen og polymer. Dette er presentert videre i Artikkel I.

Den andre typen nanokompositter var faste polymerer med leirepartiklene innkapslet mellom polymerkjedene. En rekke overflatemodifiserte leirer og polymer-leire nanokompositter, både opplinjerte og ikke-opplinjerte, ble syntetisert og analysert i detalj ved bruk av forskjellige teknikker. Flere interessante funn fra dette arbeidet er presentert i Artikkel II, Artikkel III og Artikkel IV. For det første ble det funnet en nesten lineær sammenheng mellom mengden av overflateladning i hver leire, og mengden av surfaktant de kunne ta opp. Overflateladningen bestemte ytterligere indirekte graden av forbedring i termisk utholdenhet. Lavere overflateladning førte til økt dispergering av leirene, som resulterte i større forbedringer for polystyren-leire nanokompositter (PSNCs). Det motsatte ble imidlertid observert for nylon 6/leire nanokompositten (N6NCs). I disse materialene ble både termiske og mekaniske egenskaper forbedret mest når overflateladningen til leira var høy. For de opplinjerte PSNC-prøvene viste det seg at opplinjeringen førte til dårligere mekaniske egenskaper på grunn av en mer heterogen mikrostruktur. N6NC-prøvene var på den annen side ikke mulige å opplinjere med teknikkene som ble utviklet i dette arbeidet.

I kapittel 1 presenteres motivasjonen for arbeidet, sammen med en kort introduksjon til de ulike materialene som er studert. En beskrivelse av de forskjellige eksperimentelle teknikkene som ble anvendt, så vel som de ulike instrumentene som ble brukt presenteres i kapittel 2. I kapittel 3 presenteres et sammendrag av resultatene, samt en kort gjennomgang av ikke-publiserte arbeider. Avsluttende konklusjoner og tanker om videre arbeid er presentert i kapittel 4. Videre forklarer kapittel 5 hva mine bidrag er til de vitenskapelige publikasjonene vedlagt i kapittel 6. I Appendix A er bruksanvisningen for den modifiserte høytemperaturovnen til bruk ved *in situ*-røntgeneksperimenter lagt ved, mens i Appendix B foreligger Matlab-koden til et dataprogram skrevet for å utføre manipulasjon av store røntgendatasett.

Acknowledgements

After nearly four years of working with this Ph.D. I have met and interacted with a lot of people on the way. Many of whom I am truly grateful.

First and foremost I would like to thank my supervisor Dr. Kenneth Dahl Knudsen. I am forever indebted to him for guiding me through these four years. He has always taken the time to help me, usually whenever I have found it convenient. His strong involvement in writing the papers has also been invaluable, and I must say he is a shining example of the ultimate supervisor.

I am also grateful for all help from my second supervisor Prof. Geir Helgesen. More than once he has helped solving puzzles with his ingenuity and thoughtful insights.

I would also specifically thank Prof. Jon Otto Fossum for letting me play around in his lab, and giving me the opportunity to visit conferences at exotic locations.

Furthermore my thanks go to Fredrik Hage for performing preliminary TEM-investigations of several samples, and for fruitful discussions around small things, Jussi-Petteri Suuronen for performing the XMT-experiments, my father Sverre for providing bent angular Al-plates for the low-temp. electrodes, Dr. Henrik Hemmen for helping pushing me towards the finish line and being my trusted interpreter during our numerous trips to France and Brazil, Elisabeth Lindbo for all help with the papers and interesting discussions during night shifts, Thomas Haraldsen for helping with fabrication of Al-rods for the high-temp.electrodes, Nils Jørgen Svendsen for fruitful high-voltage discussions, Ole Tore Buset for helping with practicalities at NTNU, Prof. Arne Mikkelsen for helping with the TEB experiments, and all the people at the physics department at IFE for our encouraging atmosphere.

Almost last, but absolutely no least, my gratitude is directed at two of my trusted co-authors on several papers, Dr. Zbigniew Rozynek at NTNU and Dr. Tomás Plivelic at Max-Lab.

Most of all, I wish to thank my family and friends for accepting my lifestyle during the last four years. I guess you are really fed up with my Ph.D. now;)

Lastly, my thanks go to my beloved grandmother, Aase. Now I'm one step closer to your prediction from 1983! Tusen takk bestemor!

Preface

The present thesis describes my work for the Ph.D. degree at the Department of Physics, University of Oslo. The experimental work was carried out under supervision by Prof. Kenneth D. Knudsen and Prof. Geir Helgesen, at the Physics Department at Institute for Energy Technology (IFE), Kjeller, in the period between August 2009 and October 2012. Some of the work was performed at the Physics Department at the Norwegian University of Science and Technology (NTNU) in Trondheim, at Max-Lab in Lund, Sweden, and at The European Synchrotron Radiation Facility (ESRF) in Grenoble, France. The work was funded by The Research Council of Norway through the FRINAT project 191564/V39.

If not stated otherwise I am responsible for the experimental work, such as developing procedures for syntheses, and assembling custom setups for various tasks. All figures shown in this thesis were also created by me unless stated otherwise.

In chapter 1 our motivation to the work is explained together with a short introduction to the various materials studied. Chapter 2 follows with a brief explanation of the scientific background and the different experimental techniques employed, as well as a description of the various instruments being used. In chapter 3 a synopsis of the results is presented, including presentations of non-published work. Chapter 4 presents some concluding remarks and chapter 5 presents my contribution to the scientific papers attached. Appendix A presents the short user manual for the custom high-temperature furnace commissioned during this work. Appendix B presents the Matlab code to a program written to perform manipulation of large x-ray data sets.

List of papers

I **Oxygen-Controlled Phase Segregation in Poly(N-isopropylacrylamide)/Laponite Nanocomposite Hydrogels**

Henrik Mauroy, Zbigniew Rozynek, Tomas S. Plivelic, Jon Otto Fossum, Geir Helgesen and Kenneth D. Knudsen. *Langmuir*, **2013**, 29(1), 371-379.

II **The effect of clay surface charge on the emerging properties of Polystyrene-clay nanocomposites**

Henrik Mauroy, Tomas S. Plivelic, Elisabeth L. Hansen, Jon Otto Fossum, Geir Helgesen and Kenneth D. Knudsen. *(Accepted by Journal of Physical Chemistry C, 27 August **2013**)*

III **Anisotropic polystyrene-clay nanocomposites: Synthesis, characterization and mechanical properties**

Henrik Mauroy, Tomas S. Plivelic, Jussi-Petteri Suuronen, Jon Otto Fossum and Kenneth D. Knudsen. *(In preparation)*

IV **Synthesis and characterization of nylon 6/clay nanocomposites using different 2:1 smectic clays**

Henrik Mauroy, Jussi-Petteri Suuronen, Kenneth D. Knudsen. *(In preparation)*

V **Dipolar ordering of clay particles in various carrier fluids**

Zbigniew Rozynek, Henrik Mauroy, Rene C. Castberg, Kenneth D. Knudsen and Jon Otto Fossum. *Cuban Journal of Physics, Revista Cubana de Fisica*, **2012**, 29(1E), 37-41

VI **Different Aspects of Electrically Activated PP/Clay Nanocomposites**

Zbigniew Rozynek, Suédina M L Silva, Ernesto N. de Azevedo, Geraldo J. da Silva, Henrik Mauroy, Jon Otto Fossum, Tomâs S Plivelic *(In preparation)*

VII **Complex coacervate micelles formed by a C18-capped cationic triblock thermoresponsive copolymer interacting with SDS**

Wei Wang, Henrik Mauroy, Kaizheng Zhu, Kenneth D. Knudsen, Anna-Lena Kjøniksen, Bo Nyström, Sverre Arne Sande. *Soft Matter* **2012**, 8, 11514-11525.

Table of Contents

Glossary

CEC	Cation exchange capacity
Fh	Fluorohectorite
HT	Hectorite
KPS	Potassium peroxodisulphate ($K_2S_2O_8$)
Lp	Laponite
MMT	Montmorillonite
Mw	molecular weight
NCs	Nanocomposites
N6NCs	nylon 6/clay nanocomposites
PCN	Polymer Clay Nanocomposites
PE	polyethylene
PNIPAAM	poly(N-isopropylacrylamide)
PSNCs	polystyrene-clay nanocomposites
RT	Room temperature
R5P	riboflavin-5'-phosphate
SANS	Small angle neutron scattering
SAXS	Small angle x-ray scattering
Sdd	Sample to detector distance
WAXS	Wide angle x-ray scattering
XMT	X-ray computed microtomography

1 Introduction

1.1 Polymer clay nanocomposites (PCNs)

If you took a look around where you sit right now, chances are *very* high that you will get across an object made of plastic. Plastics are a type of functional materials and a cornerstone of daily life of the 21st century, as they can be found nearly everywhere, from mobile phones and drinking bottles to clothes and car interiors. These versatile materials are mostly made from synthetic polymers derived from petrochemicals, but can also be made of polymers from natural sources. Natural rubber, which most car tires are made of, and carbohydrates are examples of this.

Some of the reasons behind the enormous popularity of polymers are that they are cheap, lightweight, and the physical properties are highly tunable. By changing the molar weight (Mw) in polyethylene (PE) for instance, it can change from being the soft and flexible plastic found in grocery bags, to the much tougher type that soda bottle caps are made of.

Another route to strengthen plastics is to add a second component made of a different material, called filler, with different physical or chemical properties compared to polymers. These composite materials can have radically enhanced properties compared to their pristine polymer-brothers -and sisters, such as increased mechanical strength, impact, abrasion and corrosion resistance, or improved gas barrier properties. Improvement of the mechanical properties is highly dependent on a large interfacial area between the filler and matrix, and as such, anisotropic particles like fibers and lamellae are preferred as fillers due to their large specific surface area [1]. It is therefore not surprising that perhaps the most known polymer composite is glass fiber reinforced plastics, commonly only referred to as *glassfiber* in Norwegian. Here glass fibers are embedded in a polymer matrix in typically a 50:50 polymer to fiber volume ratio [2]. This tough composite is used for making boat hulls, body parts of cars, and cross-country poles to name a few applications [3-6].

The improved physical properties come at the cost of higher weight since the filler is usually made from materials with 2-4 times the density of the polymer matrix. Relatively recently (compared to the history and use of synthetic polymers) Okada et al. [7] developed a novel polymer composite made of nylon 6 with natural montmorillonite

(MMT) clay particles as filler. This material was revolutionary in the way that it only contained around 5 wt.% of filler, but performed equally well as conventional polymer composites. The low weight fraction was possible due to the large surface area of the clay particles, which were dispersed homogenously and randomly in the nylon 6 matrix as disc shaped nanoparticles measuring only 1 nm in thickness and around 30 nm in diameter. Clays have the unique property that their structure can easily be delaminated to form plate-shaped nanoparticles. The effective surface area can therefore reach several hundred square meters per gram [8]. Due to the nanometer sized filler particles this class of materials became known as *polymer clay nanocomposites* (PCN). Since then a range of PCNs have been explored where different sorts of polymers and nanoparticles have been used apart from clay, such as carbon nanotubes, metal oxide nanorods and nanospheres [1].

1.2 Motivation

The topic of PCNs was a natural direction to work along in this thesis due to several reasons. A collaborating group at NTNU had already for over a decade focused on clays [9-15], and for some time worked with electric field induced self-organization of clay particles in suspensions [10, 14, 16, 17]. Furthermore a former PhD-student at the department of physics at IFE, Eldrid Svåsand, had in her PhD-work on electrically conductive carbon nanocones [18] laid the foundation for another, at that time, ongoing project at IFE. This project, recently commercialized by the company CondAlign AS, focused on polymer films with embedded strings made of conducting nanoparticles.

With this underlying knowledge the resulting project of this thesis was therefore aimed at synthesizing and characterizing bulk PCNs with aligned clay nanoparticles. Alignment would be performed with the means of external electric or magnetic fields, and would lead to anisotropy in the physical properties of the resulting PCNs. Anisotropic properties are already utilized in plastic composites where the reinforcing fibers are laid or woven in specific directions before adding the polymer matrix. We found the prospect of obtaining the same results by self-assembly of nanoparticles highly motivating. Furthermore, to the best of our knowledge there was not any work in the literature where this route had been used before.

1.3 Materials

1.3.1 Choice of polymers

Since this thesis work was the startup of the activity on this class of functional polymeric materials at the Physics Department at IFE, we decided that in order to center the attention on the specific aspects mentioned above, i.e. introduction of anisotropic properties by manipulation of nanoparticle orientation via external fields, it would be wise to keep our study to known PCN-systems that could be prepared in our home lab. Furthermore, our home lab was not equipped to be a chemical processing plant, so we wanted to use polymers that could easily be polymerized without the need for upgrading our lab with expensive processing units often needed when synthesizing polymers. After a thorough literature search, three polymers were chosen based on two main criteria: Firstly the PCN-system had to be already known, and secondly be able to be polymerized in liquid form at near ambient conditions.

1.3.1.1 Poly(N-isopropylacrylamide) (PNIPAAM)

The first polymer, PNIPAAM, is a water soluble and biocompatible polymer most easily prepared via free-radical polymerization at room temperature of NIPAAM monomer dissolved in a polar solvent. Free-radical polymerization is initiated by radicals created by heating the monomer alone or from the homolytic cleaving of an initiator molecule. In this work PNIPAAM was made with the latter process by reaction with potassium peroxodisulphate (KPS) as illustrated in the scheme in Figure 1.

A particularly interesting feature of PNIPAAM is that it switches from being hydrophilic to hydrophobic above a certain critical temperature of around 30 °C in water, at which point the polymer chains contract from a loose coil conformation into denser hydrophobic entities [19, 20]. Cross-linked PNIPAAM creates free-standing hydrogels when dispersed in water, and has thus been proposed as a novel drug delivery system where the heat-induced shrinking could be utilized to control the release of drugs inside the body [19, 21]. Cross-linking is performed chemically by interconnecting the polymer chains with shorter organic molecules. This procedure leads to inhomogeneous structures with low mechanical integrity due to an unevenly distributed cross-link density [22].

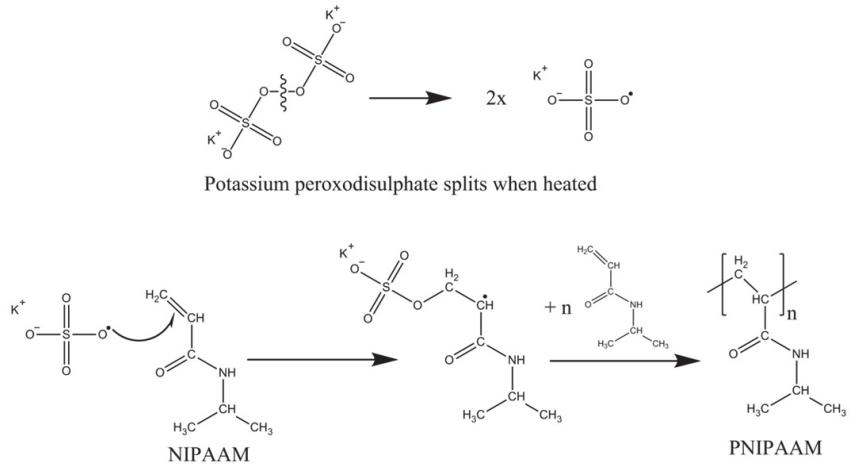

Figure 1 *Reaction scheme showing how the sulfate radical is created and how it reacts with the NIPAAM monomer to produce PNIPAAM.*

A type of nanocomposite hydrogels (NC-gel) that resolved the problem with inhomogeneities was invented by Haraguchi et al [23]. PNIPAAM was here polymerized in a water-dispersion containing a few weight percent Laponite clay. This resulted in a mechanically tough and rubberlike hydrogel with large reversible stretching abilities. In this type of PCN the clay particles were homogenously distributed in the swollen polymer matrix and linked together by the flexible polymer chains via hydrogen bonding between the surface of the clay and the amide groups of PNIPAAM [22]. In the present thesis these NC-gels were explored further.

1.3.1.2 Polystyrene (PS)

The second polymer, polystyrene, has been synthesized for more than a hundred years and is the fifth most used polymer worldwide with a yearly consumption of around 15 million tonnes [24]. PS is used in a range of products, but is probably best known as Styrofoam, used in food containers, packing materials and building insulation. PS is made from polymerization of styrene monomer through different macromolecular chain-building mechanisms: free-radical, ionic and coordination polymerization [24]. Free-radical polymerization, however, is the most commonly used method and uses peroxides or azo compounds as initiators. Styrene is liquid at ambient conditions, which enables PS to be polymerized in a one-pot method where the monomer itself also serves as the solvent. The resulting material is in the form of a solid block of polymer. Figure 2 shows the reaction

between benzoyl peroxide and styrene monomer, as used in this work, resulting in polystyrene.

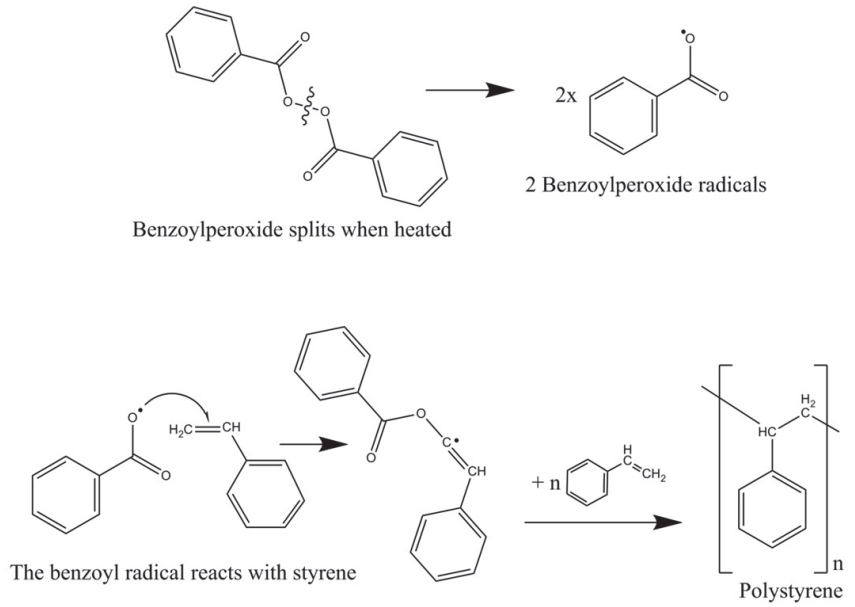

Figure 2 *Reaction scheme showing how the benzoyl peroxide radical is created and how it reacts with the styrene monomer to produce polystyrene.*

Due to the steric hindrance of the phenyl groups that PS forms during free-radical polymerization, amorphous structures are created with no clearly defined melting point, although above 100 °C the material softens considerably. Crystalline (syndiotactic) PS, on the other hand, has a melting point of 270 °C, but is more expensive to produce [24]. In this form every second phenyl group points in the same direction along the carbon backbone, whereas in amorphous (atactic) PS the phenyl groups are randomly distributed. The third form is isotactic PS (iPS) where all phenyl groups point in the same direction. iPS is semicrystalline and has three melting points in the range ~140-240 °C [25], dependent on the thermal history of the sample. Due to the extremely slow crystallization rate of isotactic PS [24], and the higher cost of crystalline PS, amorphous PS is the only form produced commercially.

Due to the amorphous nature of this polymer, PS-clay PCNs are of use as model compounds because any changes in overall properties will mainly be due to the additives

used. They have, in spite of extensive academic studies, not been commercialized [1]. One reason for this is the inherent difficulty of dispersing clay particles which are hydrophilic in the hydrophobic PS matrix. A workaround is to render the surface of the clay particles hydrophobic by coverage of organic surfactants which are miscible with styrene, which was the path chosen in this doctoral work.

1.3.1.3 Nylon 6

The third polymer, nylon 6, is also a popular industrial polymer. It is used in a number of applications such as fishing lines and the cord in weed trimmers, wheelchair wheels, automotive cooling fans, and as food packaging film [26]. Nylon 6 is made from ring opening polymerization of melted ε-caprolactam monomer at 260 °C as depicted in Figure 3. In this work 11-aminoundecanoic acid was used as the initiator together with small amounts of water.

Nylon 6 is semi-crystalline which means that the structure of the neat polymer can be viewed as a composite on its own with crystalline domains dispersed in an amorphous matrix. The polymer itself has excellent physical properties at elevated temperatures, and can in a glass-fiber reinforced composites retain these properties up to its melting point of around 220 °C [26]. Due to the polar amide group nylon 6 is, in contrast to PS, miscible with clay.

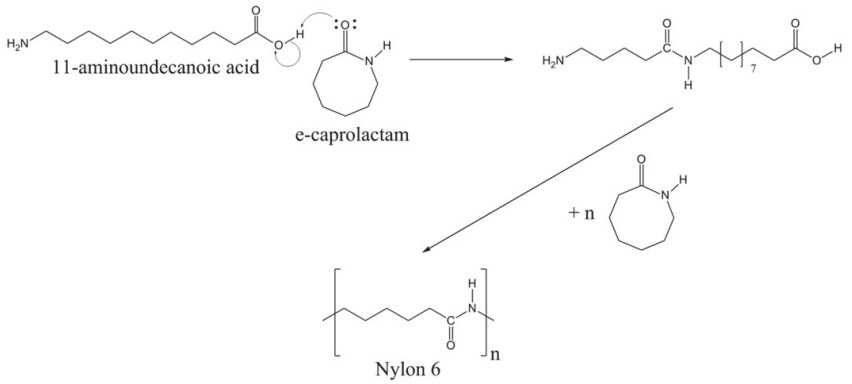

Figure 3 *Simplified reaction scheme showing ε-caprolactam donating an electron pair to the hydroxyl group of 11-aminoundecanoic acid. This reaction initiates the polymerization by creating a dimer that can continue to react with more ε-caprolactam to produce nylon 6.*

1.3.2 Clay

Clay is a type of minerals built up of layers consisting of silicate sheets stacked together with aluminium- or magnesium hydroxide sheets. The structure of the 2:1 clays used in this work have a single hydroxide sheet built up of edge-sharing octahedra (O-layer) sandwiched between two silicate sheets composed of corner-sharing tetrahedra (T-layer). Isomorphous substitution of the cations by cations with a lower valence leads to a net negative surface charge on the layers, which is counterbalanced by cations (M^+) placed between the layers. The sharing of cations between two layers leads to an effective attractive force between the layers. This force is counterbalanced by the repulsive force that the negatively charged surfaces exert onto each other. The 2:1 clays belong to the group of *micas*, but for simplicity they will be called *clays* throughout this thesis and in the attached papers.

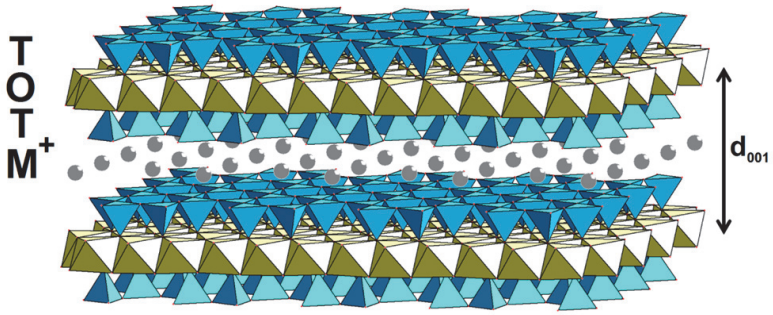

Figure 4 *The crystal structure of 2:1 clays showing two silicate sheets sharing counterbalancing cations (M^+).*

Figure 4 shows a section of the crystal structure of a typical 2:1 clay where two layers are bound together by sharing counterbalancing cations. The stacking of the layers is along the 001 crystallographic direction. The interlayer spacing of clays, d_{001}, is determined by the type of counterbalancing cations and molecules that are intercalated between the clay layers. Water molecules are easily intercalated because they make complexes with the cations, and are therefore almost always present in clays stored in normal atmospheres containing some humidity. Other gaseous molecules such as CO_2 can also be intercalated [27]. The d_{001}-spacing can readily be increased by substitution of the counterbalancing cations by large positively charged molecules, and this is easily monitored by x-ray diffraction. In the extreme case where the d_{001}-spacing increases to such a degree that the

attractive force holding the layers together diminishes significantly, the layers come apart and the clay is said to exfoliate. The Laponite clay studied in this thesis, for instance, exfoliates easily when dispersed in pure water. Exfoliation is a key to obtain well-dispersed clay nanoparticles for the production of high-performance PCNs.

Clay is hydrophilic and is thus immiscible with PS, but on the other hand mixes well with PNIPAAM and nylon 6. For a sufficient mixing of clay and PS the clay was in this thesis work surface modified by substituting the counterbalancing inorganic cations with organic ammonium cations.

1.3.3 PCNs production

There are two major methods for the production of PCNs. The first one is melt compounding and involves mixing a melted neat polymer with surface modified clay in a physical mixer under inert atmosphere. The industrial standard requires that more than 80 % of the clay layers are individually and uniformly dispersed in the polymeric matrix, with the rest forming short stacks [1]. Because of the requirement for liquid processing of polymers in the fabrication of PCNs, melt compounding can only be done with thermoplastics. The second method is called *in situ* intercalative polymerization, and can be utilized for both thermoplastics and thermosets. Here the clay is first mixed into a liquid monomer mixture which is later polymerized under inert atmosphere. This method leads to increased exfoliation compared to melt compounding, but is, however, not as easy to implement industrially. Products made from thermoplastic PCNs are usually prepared with injection molding where the melted PCN is injected into a mold under high pressure. Thermosetting PCNs, on the other hand, are prepared directly inside the mold.

2 Experimental

2.1 Sample preparation

2.1.1 Polymerization: Chemistry

Free radical polymerization is usually performed under inert atmosphere to prevent atmospheric dioxygen (O_2) to react with the radical end groups of the growing polymer chains. In the stable paramagnetic form of O_2 there is one unpaired electron in each of the two antibonding π^* orbitals giving rise to a radical-like behavior of the molecule. O_2 will therefore readily react with a growing polymer chain and stop the growth due to the much less reactive carbon-O_2* radical which is formed [28]. In this work all handling of the chemicals used for the preparation of PNIPAAM was performed inside a glove bag filled with either argon 5.0 or nitrogen 5.0 gas. The bag was emptied and filled with gas at least three times to lower the oxygen concentration inside. Polymerization was performed at room temperature inside several types of glass containers such as thin-walled capillaries, bottles and tubes. In Paper I the samples were all handled in controlled O_2-atmospheres ranging from 5 to 50 % pO_2.

For the preparation of PS the atmospheric O_2 did not pose a big threat to the polymerization reaction because the solubility of O_2 in styrene is low due to the nonpolar nature of styrene, and the elevated temperatures used for polymerization (70-100 °C). It was sufficient to keep the monomer solutions in sealed glass bottles or capillaries to obtain the desired products. A more detailed description of the preparation can be found in Paper II.

Preparation of nylon 6 was also performed inside sealed glass capillaries, but at higher temperatures than for PS (260 °C). Since nylon 6 is made from ring opening addition-polymerization the reaction is not dependent on any radical species during the course of polymerization, and thus O_2 would not perturb the reaction as in the cases with PNIPAAM and PS. A more detailed description of the preparation can be found in Paper IV

2.1.2 Polymerization: *In situ* electric field induced alignment

Clay particles suspended in a fluid with a lower dielectric constant will be polarized by an external electric field according to the following general, but simplified relation [29]:

$$p \propto \varepsilon_f \frac{\varepsilon_p - \varepsilon_f}{\varepsilon_p + 2\varepsilon_f} E \quad (1)$$

where p is the dipole moment, ε_f and ε_p are the dielectric constants of the fluid and the clay particles, respectively, and E is the applied electric field. A larger polarization, and thus a stronger force exerted by the electric field on the clay particles, occurs for large differences in dielectric constant between the clay and the fluid. Inside an electric field the clay is electrically polarized along the silica sheets [14, 30], i.e. their stacking direction, $\hat{\boldsymbol{n}}$, is perpendicular to the direction of the electric field. The polarization of the clay leads to attractive dipole-dipole forces between individual clay particles which results in chain formation.

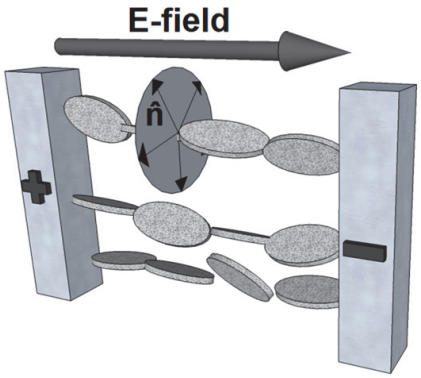

Figure 5 *Sketch of how the clay particles align in an E-field [31].*

Two custom electrode setups were developed for polymerization of the PS-clay NCs inside an electric field (Figure 6). They both consisted of two 60x80 mm parallel plate aluminium electrodes fixed together with nylon screws, spaced either 1.6 or 3.6 mm apart using small Teflon-washers around the screws. Wires were secured with steel screws to each of the electrodes. A large 1.5 mm thick Teflon sheet was fitted across the electrodes with holes to fit capillaries down into the electrode cell. During polymerization, the whole setup was lowered down into silicone oil in a glass beaker, which was put on top of a hot-plate. In

order to isolate the electrode cell from the surroundings it rested on the rim of the glass beaker via a pair of Teflon-flaps, protruding out from the electrodes. The setup could hold up to six capillaries at a time, which were loaded into the cell from the top in a standing orientation. Small washers made from heat-shrinkable tubing were fitted around the capillaries to prevent them from falling down through the spacing between the electrodes.

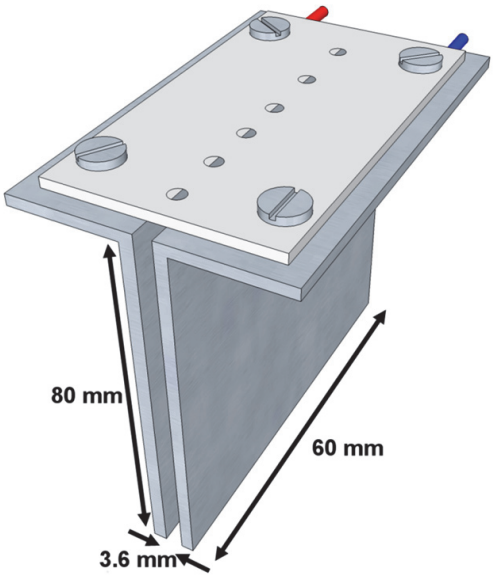

Figure 6 *Sketch of the electrode setup. The wiring is protruding out from the back.*

A BK Precision 4010A signal generator was used to produce a square wave signal which was fed to either a Trek 2210 Piezo high voltage amplifier (1000V), or to an AP-3B1 high voltage amplifier (3000V) from Matsusada Precision Inc. The resulting maximum field strengths for the different combinations of electrode setups are listed in Table 1.

Table 1. *Maximum electric field strength of the electrode setups*

HV-amplifier	1.6 mm electrode cell (V/mm)	3.6 mm electrode cell (V/mm)
Trek 2210	625	280
Matsusada AP-3B1	1875	830

2.1.3 Surface modification of clay

As mentioned earlier clay has a highly polar nature, thus in order to be compatible to nonpolar polymers, such as PS, they need to be surface treated. In this work the inorganic counterbalancing cations of the clays were exchanged with cetyltrimethylammonium bromide (CTAB), a molecule containing a positively charged ammonium head group and a tail of 16 carbon atoms, through a simple cation-exchange process: Clay and CTAB are dissolved in water separately. Upon mixing the two solutions the positive head group of the CTA^+ carbocation attaches to the surface of the clay, rapidly covering the clay platelets. The bromine anions are balanced by the inorganic cations of the clay (usually Na^+ or Ca^{2+}). Since the protruding nonpolar tail-groups of CTAB are immiscible with water the CTA^+-covered clay platelets quickly precipitate from the solution. Centrifugation and rinsing the precipitate several times is necessary to remove the inorganic bromine salts which are dissolved in water. A similar procedure was used to compatibilize clay further before mixing with ε-caprolactam for the synthesis of nylon 6/clay nanocomposites. 11-aminoundecanoic acid was here the surfactant.

2.2 X-ray scattering

The most important experimental tool used in this work has been small angle and wide angle x-ray scattering (SAXS and WAXS). Due to its relevance here a brief explanation of the principle and techniques is given in the following sections.

2.2.1 Principles

X-rays are scattered both elastically and inelastically from matter. The latter process is known as the Compton effect, and becomes progressively less pronounced as the x-ray energy is increased to above 10 keV, which is the typical energy used in SAXS/WAXS experiments [32]. The elastic scattering, however, is what will be referred to as x-ray scattering in the following sections.

Generally when a monochromatic electromagnetic wave scatters elastically off a particle the magnitude of its scattering vector is given by

$$q \equiv |\boldsymbol{q}| = \frac{4\pi}{\lambda} sin\theta \tag{2}$$

where $\boldsymbol{q}$ is defined as the difference between the propagation vectors of the incoming and scattered wave, θ is the angle of the scattered wave with respect to the incoming wave, and λ is the wavelength. If there is more than one particle, the amplitude, E_S, of the scattered waves measured by a detector is the sum of the scattered waves from all N particles of type j [33]:

$$E_S(\boldsymbol{R}, t) = -\frac{E_I}{\boldsymbol{R}} e^{i(\boldsymbol{kR}-\omega t)} \sum_{j=1}^{N} b_j(\boldsymbol{q}, t) e^{-i\boldsymbol{qR}j} \tag{3}$$

where $\boldsymbol{R}$ is the position of the detector in the far field, $\boldsymbol{q}$ is the scattering vector, $\boldsymbol{k}$ is the propagation vector of the incoming wave, and E_I and ω is the amplitude and frequency of the incoming electromagnetic wave, respectively. b_j is defined as the *scattering length* of particle j with the following expression

$$b_j(\boldsymbol{q}, t) = \int_{V_j} \Delta\rho(\boldsymbol{r_j}, t) e^{-i\boldsymbol{q}\boldsymbol{r}_j} d^3\boldsymbol{r}_j \tag{4}$$

where $\Delta\rho$ is a measure of the local density of scattering material (scattering length density) in a small volume dV_j inside the particle j at a position $\boldsymbol{r}_j$ relative to the particle's centre of mass (see Figure 7).

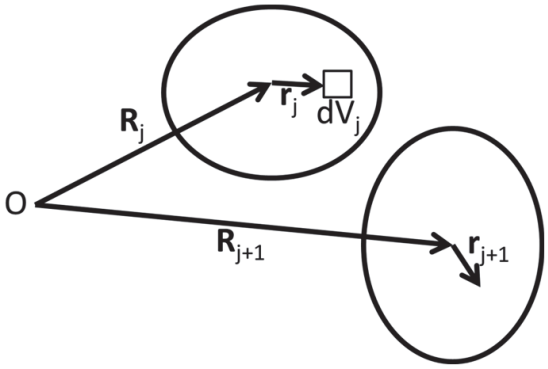

Figure 7 *Coordinates for discrete scatterers inside two particles relative to an arbitrary origin O.* $\boldsymbol{R}_j$ *is the position of the centre of mass of particle j and* $\boldsymbol{r}_j$ *is the position of volume element* dV_j *in particle j [33].*

In a scattering experiment the instantaneous intensity $I(\boldsymbol{q},t)$ measured by the detector is the square of the amplitude E_S being generated from N scatterers (eq.(3)). Omitting for simplicity the prefactors of eq. (3) we get

$$I(\boldsymbol{q},t) = |E_S(\boldsymbol{R},t)|^2 = \sum_{j=1}^{N}\sum_{k=1}^{N} b_j(\boldsymbol{q})b_k^*(\boldsymbol{q})e^{-i\boldsymbol{q}[\boldsymbol{R}j-\boldsymbol{R}k]} \tag{5}$$

In this step the phase information of the scattered waves is lost. It is therefore not possible to determine the positions of individual particles directly from taking the inverse Fourier transform of the scattered intensity. There is still, however, a large amount of information left in the measured intensity.

In a dilute system of identical scatterers the particles are, on average, widely separated so that their behaviors are uncorrelated. The exponential functions in eq. (5) will therefore all cancel out because particle j can take up any available position in the sample over time. The expression for the time averaged intensity is thus reduced to [33]:

$$\langle I(q)\rangle = N\langle|b(\boldsymbol{q})|^2\rangle \tag{6}$$

which can be rewritten as

$$\langle I(q)\rangle = N\langle|b(0)|^2\rangle P(q) \quad \text{with} \quad P(q) \equiv \frac{\langle|b(\boldsymbol{q})|^2\rangle}{\langle|b(0)|^2\rangle} \tag{7}$$

The *form factor P(q)* is defined such that $P(q)\rightarrow 1$ as $q\rightarrow 0$ [33], and is thus given directly by the measured scattering pattern and gives information of the shape of a given particle. The form factor for a homogeneous sphere with radius R, volume v and scattering length density ρ_0 is given by [34]:

$$P(q) = {\rho_0}^2 v^2 \frac{9(\sin qR - qR\cos qR)^2}{(qR)^6} \tag{8}$$

Similarly the corresponding form factor for a homogenous thin disc (such as a single clay platelet) with radius R is given by [34]:

$$P(q) = {\rho_0}^2 v^2 \frac{2}{q^2R^2}\left[1 - \frac{J_1(2qR)}{qR}\right] \tag{9}$$

where $J_1(x)$ is the first-order Bessel function.

The two form factors listed above falls off rapidly at large q , and it can be shown that the intensity may be represented by $I(q)\sim q^{-\alpha}$, where the exponent α is equal to 4 for spheres, 2 for thin discs, and 1 for thin rods [34]. The shape of the scattering curve, resulting from measuring the intensity over a range of angles, is thus seen to reflect the dimensionality of the scatterer.

2.2.2 WAXS/SAXS

Equation (5) can be applied for dilute systems consisting of either randomly dispersed particles or atoms. However, in concentrated systems, such as solids, the motion and therefore also the positions of the particles are usually highly correlated. The exponential functions in eq. (5) will now *not* cancel each other out, and for a system of identical scatterers (with equal scattering lengths $b_j(q) = b(q)$) the time averaged intensity for interacting particles becomes

$$\langle I(q)\rangle = b^2(q)\sum_{j=1}^{N}\sum_{k=1}^{N}\langle e^{-i\boldsymbol{q}[\boldsymbol{R}j-\boldsymbol{R}_k]}\rangle = Nb^2(0)P(q)S(q) \tag{10}$$

where $S(q)$ is the *static structure factor*, defined by [33]:

$$S(q) \equiv \frac{1}{N}\sum_{j=1}^{N}\sum_{k=1}^{N}\langle e^{-i\boldsymbol{q}[\boldsymbol{R}j-\boldsymbol{R}_k]}\rangle \tag{11}$$

$Nb^2(0)P(q)$ describes scattering from N uncorrelated particles and the structure factor $S(q)$ represents the modification of the intensity due to the spatial correlations of the particles, and the resulting interference between the scattered waves [33].

Since x-rays are scattered by the electrons of atoms the scattering length density $\Delta\rho$ in eq. (3) is in reality the density of electrons around the nucleus. $b(q)$ in eq. (10) can then be considered as the total *scattering power*, f_j, of the whole atom j, and eq. (10) can be rewritten as

$$\langle I(q)\rangle = f_j^2(q)\sum_{j=1}^{N}\sum_{k=1}^{N}\langle e^{-i\boldsymbol{q}[\boldsymbol{R}j-\boldsymbol{R}_k]}\rangle\,. \tag{12}$$

f_j is proportional to the atomic number Z and hence the scattered intensity increases with a square dependence on the element number through the periodic system. Light elements such as hydrogen and carbon, which are the main constituents of polymers, scatter much less than the heavier elements silicon, aluminium and oxygen found in clay. It is therefore possible to get sufficient x-ray signals from PCNs containing only a few weight percent of clay because the x-ray contrast between the clay and matrix is so high.

For periodic structures such as crystals the condition for constructive interference of the scattered waves is given by Bragg's law

$$\lambda = 2d_{hkl}sin\,\theta_{hkl} \tag{13}$$

where λ is the wavelength of the scattered wave, d_{hkl} is the spacing between adjacent hkl-planes in the crystal structure, and θ_{hkl} is the angle between the direction of the incoming and scattered waves, respectively (Figure 8). Experiments using this relation are commonly referred to as diffraction experiments.

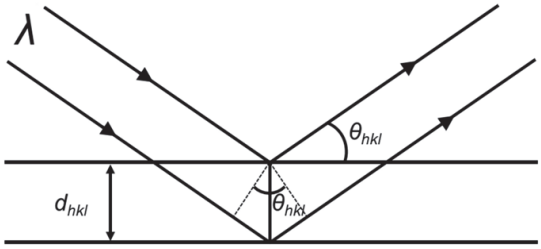

Figure 8 *Geometric representation of Bragg's law. Constructive interference of the two incoming rays occurs when the distance ABC is equal to an integral number of wavelengths.*

Since the wavelength determines the scattering angle and can vary between instruments, it is useful to represent Bragg's law in a universal form as

$$d_{hkl} = \frac{2\pi}{q_{hkl}} \tag{14}$$

where $q_{hkl} = (4\pi/\lambda)\sin(\theta_{hkl})$. The typical length scale of the periodic repetition distance d in crystals (e.g. clays) is on the order of $1 \cdot 10^{-10}$ m = 1 Å. With λ equal to 1 Å, the scattering angle 2θ is about 30°, and such experiments belong to the category of wide angle x-ray scattering (WAXS). For a larger repetition distance, such as the ordered arrangement of spherical microdomains in polymers (~100 Å), 2θ becomes as low as 0.6°. This is considered to enter in the range of small angle x-ray scattering (SAXS). The interlayer spacing in clays (d_{001}) is on the order of 10 Å, placing the scattering from clay on the borderline between WAXS and SAXS. A combination of the two techniques, which require somewhat different experimental setups, was thus needed when measuring the structure of the clays studied in this work.

2.2.3 Geometry

In a typical SAXS/WAXS experiment the x-ray beam is directed at the sample and the intensity of the scattered beams is measured by a two-dimensional detector in the forward direction (Figure 9). In powders and polycrystalline samples the particles or crystals can be assumed to be randomly oriented in all configurations. The scattering is then distributed on the surface of *Debye-Scherrer* cones with half opening angles of 2θ. Two-dimensional detectors, such as the ones used in this work, effectively make slices through these scattering cones, and the resulting scattering pattern is therefore built up of concentric

circles (Figure 9) A one-dimensional (1D) scattering curve, measured as intensity as a function of the scattering angle relative to the primary beam, is in this case obtained by integrating the 2D-scattering pattern radially outwards around the azimuth angle. The angular range, and thereby the measurable range of $\boldsymbol{q}$, can be tuned by adjusting either the wavelength and or the sample-to-detector distance (Sdd) for the experiment. Typically only the Sdd is changed because adjusting the wavelength is only possible with synchrotron instruments, unless one changes the x-ray source element.

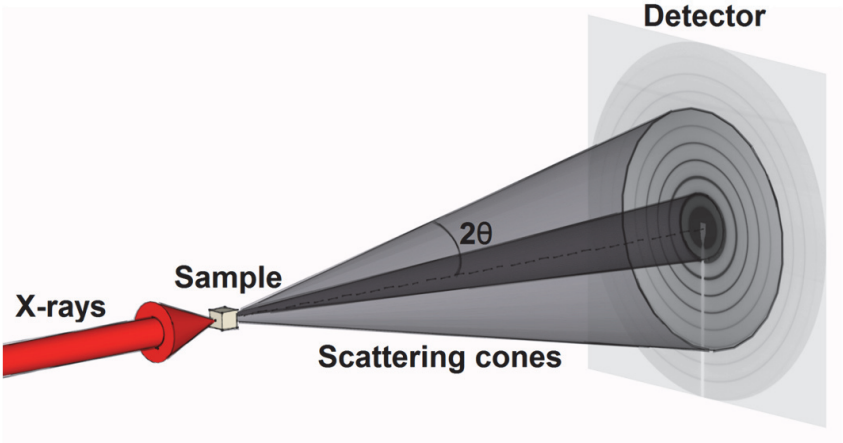

Figure 9 *Schematic view of the scattering geometry in SAXS/WAXS experiments. X-rays enter from left and are transmitted and scattered by the sample as Debye-Scherrer cones with half opening angle 2θ. The cones appear as concentric circles in the detector plane.*

2.2.4 Anisotropy

In scattering experiments the sample is usually rotated in order to average out effects from preferential orientation of crystals. Clay crystals, for instance, cleave along the 001 plane which results in platelet shaped particles with a high aspect ratio. As a result clay particles in powdered samples are prone to stack on top of each other in a nearly parallel fashion, i.e. their plate normals $\hat{\boldsymbol{n}}$ have almost the same directions. The Bragg scattering from the 001 plane of such a sample will therefore be much more pronounced for scattering angles with $\boldsymbol{q}$ parallel to $\hat{\boldsymbol{n}}$, as is shown schematically in the sketch in Figure 10. In certain experiments the anisotropy in the scattering pattern is a desired effect and as such the sample is not rotated. The anisotropy may e.g be employed to obtain information about the orientation of anisotropic particles inside a matrix, e.g. clay in PCNs, or needle shaped exclusions in alloys.

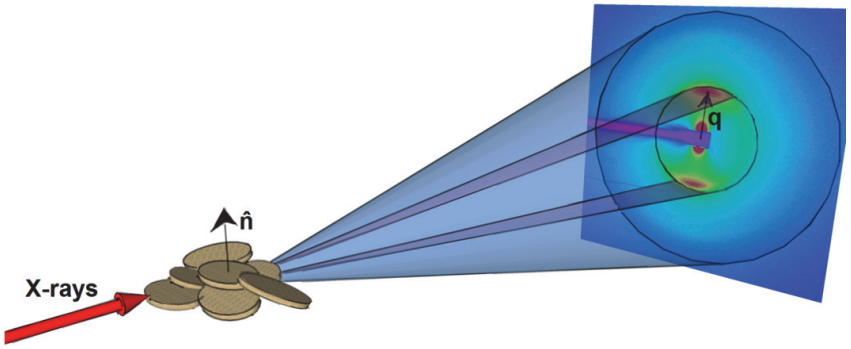

Figure 10 *Sketch of the diffraction pattern originating from highly oriented clay particles. Almost all scattering is along* ***q*** *parallel to the platelet normals* ***n̂****. A continuous band of small angle scattering along* ***n̂*** *originating from "reciprocal anisotropy" is also visible in the scattering pattern.*

A second type of anisotropy in 2D-scattering patterns is caused by size effects in the nanometer regime, and occurs as a direct consequence of the inverse relationship between the scattering pattern and real space ("reciprocal anisotropy"). A very thin rod (approx.1-200 nm) will produce scattering along a broad band directed at right angles to the length of the rod. The clay platelets in Figure 10 will for the x-rays look like thin rods and consequently scatter along a broad band in the direction of ***n̂*** in the small angle region. This anisotropy was used as a means of quantifying the structural anisotropy in samples studied in this work. By integrating the scattering patterns along narrow sectors aligned along ***q*** parallel and perpendicular to ***n̂***, pairs of 1D-curves differing noticeably in intensity was obtained (see e.g. section 3.1.3).

2.2.5 Radiation sources and instruments

2.2.5.1 NTNU

Laboratory-SAXS/WAXS data were collected with a NanoSTAR system from Bruker AXS at the Department of Physics at the Norwegian University of Science and Technology (NTNU). The system produces x-rays with a wavelength of 1.5418 Å using a sealed-tube CuK_α micro source, and is equipped with a two-dimensional multiwire grid "Xe" gas detector of 1024x1024 pixels. The x-rays are passed through a Göbel-mirror which creates a collimated and monochromatic beam. The beam is further collimated by three pinholes spaced approximately 75 cm apart. The final beam spot is 0.4 x 0.8 mm. The Sdd can be varied from 15 cm up to 115 cm covering a q-range of 0.2-25 nm^{-1}.

2.2.5.2 Dubble

Synchrontron-SAXS was performed at the Dutch-Belgian (Dubble) beamline at station BM26 at the European synchrotron radiation facility (ESRF) in Grenoble, France. This SAXS-setup is highly tunable in order to adjust the experimental parameters. The x-rays are produced by a synchrotron which accelerates electrons to relativistic speeds inside a large storage ring with a circumference of around 800 m. The circular travel path is divided into alternating straight sections and bending sections. When the electrons are deflected in the bending sections they emit a continuous spectrum of x-rays due to the centripetal acceleration they experience. The x-rays are used at different beamlines at regular spaced intervals around the storage ring, and the desired wavelength is selected by special optics through a series of monochromator crystals and slits. A typical setup used in this work at Dubble employed a wavelength of 1.5 Å and an Sdd of 4 meters. This resulted in a q-range of ~0.07-1.6 nm^{-1} making information on a length scale, $d = 2\pi/q$, up to around 90 nm available. The detector used was a two-dimensional gas filled wire-detector with 512×512 pixels constructed by the ESRF technical staff.

2.2.5.3 I911-4

Synchrotron-SAXS/WAXS studies were also performed at the I911-4 SAXS station at Max-Lab at The University of Lund, Sweden. This instrument operates with a fixed wavelength of 0.91 Å and a two-dimensional detector of 2048×2048 pixels from MAR research. The Sdd was adjusted between 0.9 and 1.9 meters resulting in a q-range of ~0.15-8 nm^{-1} corresponding to a maximum length scale of around 40 nm.

2.2.5.4 X-ray computed μ-Tomography (XMT)

Because the absorption x-ray contrast between clay and the carbon-based matrix in PCNs is so high (absorption approx. proportional to Z^4 [32]) most of the x-ray signal comes from the clay alone. It is therefore possible to perform "conventional" x-ray imaging of the clay alone in these materials with a visualization technique called x-ray computed micro-tomography (XMT). The sample is here placed inside a cone of monochromatic x-rays, and the transmitted rays are recorded by a two-dimensional computer-controlled detector as images with varying intensity. The transmitted intensity is determined by the absorption (attenuation) of the different constituents of the sample according to Beer's law

$$I = I_0 exp \sum_k -\mu_k x_k \quad (15)$$

where I and I_0 are the transmitted and incoming intensity, respectively, μ_k is constituent k's linear attenuation coefficient and x_k is the length of the x-ray path. The summation is performed over all the different constituents of the sample. By probing the sample from multiple directions and combining the resulting images with a computer algorithm a series of 2D "image-slices" of the sample is reconstructed. These can be combined with the computer into a continuous 3D-rendering of the sample which is composed of tiny volume elements called voxels. The resolution, i.e. the voxel size, is mainly determined by the detector's pixel size and the thickness of the sample. In this work a voxel size of around 0.9 μm was obtained with a custom-built Nanotom 180 NF XMT setup supplied by Phoenix|x-ray Systems + Services GmbH (Wunstorf, Germany) located at the Department of Physics at the University of Helsinki, Finland. This system is equipped with a tungsten x-ray source, a high-accuracy sample stage, and a CMOS-detector with 2304 × 2304 square pixels.

2.3 Thermogravimetric analysis (TGA)

TGA was used to measure the mass loss upon thermal decomposition of the organic constituents in both the organoclays and the nanocomposites. From this it was possible to quantitatively estimate the clay and surfactant content in the nanocomposites and organoclays, respectively, and the thermal properties of the nanocomposites as a function of temperature. In these types of experiments a few milligrams of sample material are weighed on a balance while being heated beyond the decomposition temperature of the organic phase. During this work a Netsch STA 449 F3 Jupiter TGA was used at a constant heating rate of 10 °C/min from room temperature and up to 800 °C. The samples were kept under argon atmosphere during the experiments.

2.4 In situ SAXS/WAXS furnace

Commissioning of a custom built setup for performing *in situ* SAXS/WAXS studies at the I911 beamline at Max-Lab in Lund was performed by the author in collaboration with Dr. Tomâs Plivelic (I911), and the machine shop at Max-Lab. A high-temperature Linkam TS-1500 micro furnace was modified to fit a small copper block which was able to hold a capillary with a diameter of up to 2 mm. Pictures of the setup are shown in Figure 11. The copper block is inserted into the furnace (Figure 11b) and secured with a spring, which pushes against a mounting bracket with a hole to let the scattered rays exit (Figure 11c). The maximum exit-angle for the scattered x-rays was, due to the opening in the mounting bracket, limited to 6 degrees. The complete setup, shown in Figure 11d, was tested and calibrated, and a short manual was written for future users at I911. The manual can be found in Appendix A.

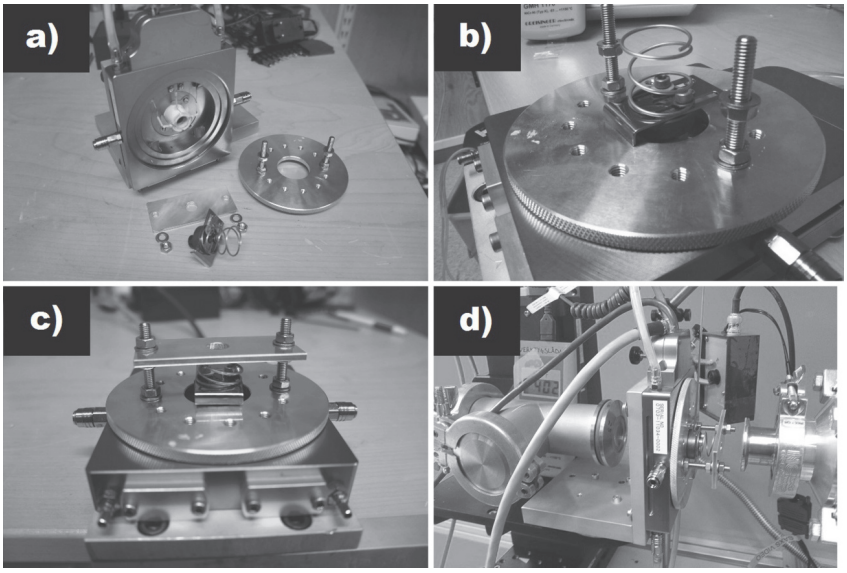

Figure 11 *Pictures of the in situ furnace built as part of this thesis. (a) The various parts disassembled, (b) the copper block inserted with the spring attached, (c) mounting bracket securing the copper block to the furnace, (d) the complete setup mounted at the beamline (the x-rays enter from the left).*

2.5 Stress tester

A custom built apparatus for measuring the mechanical properties of PNCs under compressive load was also assembled by the author. The setup was based on the ASTM D695 standard and it consisted of a Standa optical translation stage (model 7T173-10), fitted together with a digital force meter to a wooden board (Figure 12a). The samples, cut into ~1 mm^3 cubes, were placed in between the movable bracket on the translation stage and the force meter (Figure 12b-c). A compression rate of 5 μm/s and a force of up to 130 N were utilized in the experiments. Logging of the compression force was performed by video monitoring of the display of the force meter (Figure 12d). The uncertainty of the force meter was 0.5%.

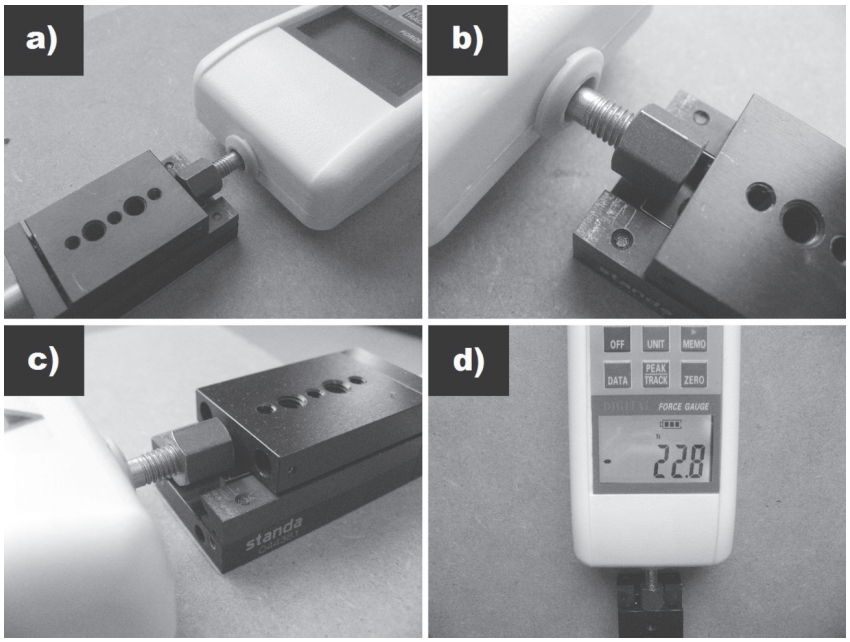

Figure 12 *Pictures of the custom built compression tester assembled by the author as part of this thesis.*

3 Synopsis of the results

3.1 NC-gels

3.1.1 Introduction

After searching the literature we found a promising water soluble polymer, poly(N-isopropylacrylamide) that could be polymerized at ambient conditions. Already mentioned in the introduction Haraguchi et al. invented a new nanocomposite by combining this polymer with the synthetic clay Laponite. The emerging nanocomposite (NC-gel) consisted of a polymer matrix physically cross-linked by single Laponite platelets.

3.1.2 Preliminary experiments and Transient electric birefringence (TEB)

Early testing proved it fairly straight forward to prepare the NC-gels (Figure 13a), but we noticed that in almost every sample phase separation occurred near the meniscus (Figure 13b), visible as an opaque ring. We then set out to reveal what caused the samples to phase separate by systematically going through our routines developed to polymerize this very system.

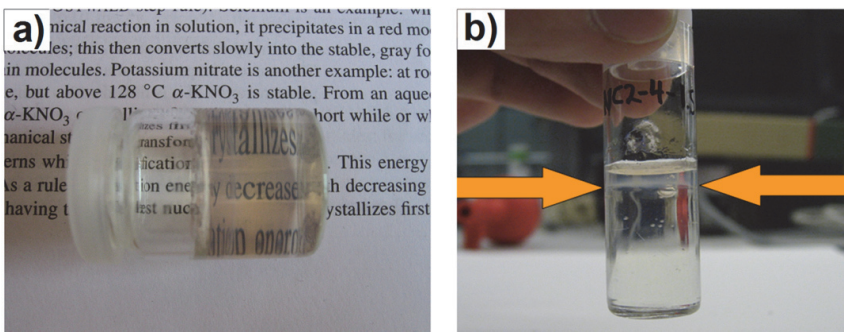

Figure 13 *(a) The first NC-gel synthesized during this work. (b) The visible ring due to the phase separation.*

It turned out that although the chemicals were handled under inert (argon, nitrogen) atmosphere, small quantities of oxygen gas could enter into the polymerization vessels at the moment when the radical initiator was added to the monomer mixture. This oxygen quickly dissolved and started attacking the growing polymer chains, forming a slightly

more water soluble phase that floated on top the polymer phase. A significant amount of time was dedicated to investigate this behavior and to understand the mechanisms for the phase separation which showed some highly interesting features. The work was published in Paper I.

The main objective for this PhD-thesis has been to prepare polymers containing nanoparticles organized in a particular manner. Our initial aim with the NC-gels was to align the Laponite clay platelets and look at the correlation between physical properties and the microstructure. In this case, due to the anisotropic microstructure, we anticipated a noticeable difference in mechanical strength that would be related to the direction of applied force. Alas, in this case water was not useful as a matrix when using electric fields to align the nanoparticles because of its large dielectric constant. However, Bakk et al. [10] showed that it was possible to align Laponite particles dispersed in water using a customized Transient Electric Pulse Induced Birefringence (TEB) setup, located in the lab of Prof. A. Mikkelsen at NTNU. To verify if the same results could be obtained for the NC-gels a quick experiment was conducted with this instrument.

The detailed description of the setup can be found elsewhere [10], but the principle can be explained as follows. Polarized laser light is sent through a solution of micro or nanoparticles. The transmitted light is then passed through an analyzer filter which is polarized 90 degrees with respect to the incoming light, before it hits a detector. If the incoming light exits the sample without changing polarization the analyzer will block the light from reaching the detector. But if the particles are arranged with some sort of long range order, they tend to turn the polarization of the light so that it can travel through the analyzer and hit the detector. The sample is kept between two parallel plate electrodes, spaced 2 mm apart, and coupled to a high voltage pulse generator to induce dipole moments in the particles.

We tested a sample containing 1.0 wt.% Laponite clay in distilled water. Different pulse times and electric field strengths were used to align the clay particles into chains. As an example Figure 14 shows the behaviour when a field of 80 V/mm was applied for 100 μs. Almost immediately after the voltage was raised (black curve) the birefringence signal (red curve) increased, indicating alignment of the clay particles. However, the alignment decayed quite rapidly within the next 80 μs showing a return to isotropic orientation. All experiments showed similar behavior, which means that in practice, clay can be dispersed

in water and become polarized by an external electric field. However, due to the (very) short time the clay particles stayed aligned we discarded the idea of using electric fields for alignment, and focused on other methods instead.

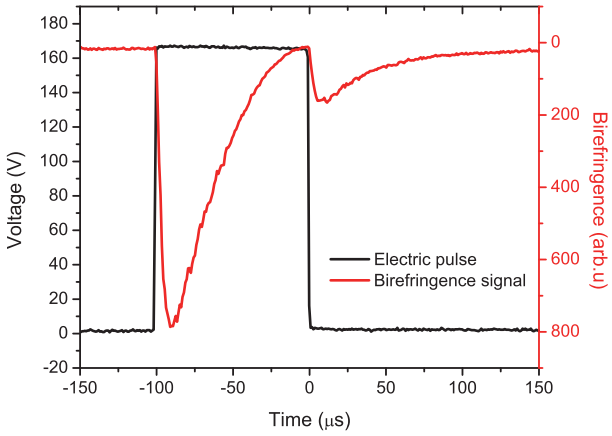

Figure 14 *Electrode voltage (black) and birefringence signal (red) from one of the TEB-experiments.*

3.1.3 Ferrofluid and Ferrogels

Another highly effective way of aligning nanoparticles is to use magnetic fields. In this case the particles need to be fairly susceptible to such fields, which Laponite is not. Magnetite, Fe_3O_4, on the other hand is a common ferromagnetic mineral which is often used in magnetic liquids (ferrofluids). These liquids are stable colloidal suspensions of nanometer-sized magnetite particles in a liquid carrier. The particle size is typically around 10 nm which is smaller than the magnetic domains needed to make magnetite permanently magnetized. As a result the particles become superparamagnetic, displaying no hysteresis in the magnetization curve. In the absence of a magnetic field, the magnetic moments of the particles are random and the particles themselves are randomly distributed in the fluid. When a magnetic field is applied on the ferrofluid, the particles orient their magnetic moments almost instantly along the field lines, and thus become tiny magnetic dipoles.

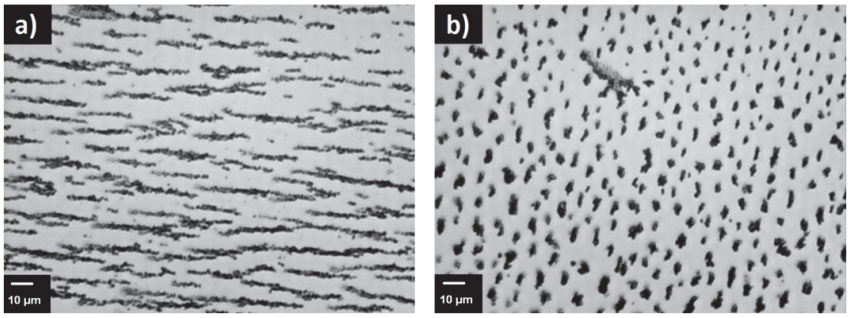

Figure 15 *Pictures of magnetite nanoparticles agglomerating into larger entities and aligning into chains inside a magnetic field: alignment along the image plane (a) or perpendicular to the image plane (b). The scale bars are 10 µm long. The pictures were shot with a Dinoeye Microscope Eye-piece digital camera mounted on an optical microscope (Nikon Optiphoto).*

The dipoles will rapidly attract each other and connect head to tail into long chains (Figure 15). When the magnetic field is removed the moments randomize quickly and the particles return to a random distribution. Since electric alignment of the Laponite clay is practically impossible using electric fields, we devised a scheme, partly inspired by the work of Teixeira et al. [35], where the pure clay in the NC-gels was decorated with magnetite nanoparticles.

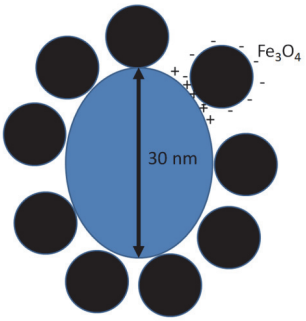

Figure 16 *Laponite particle (large oval) decorated with magnetite particles (filled circles).*

A magnetic field could thus in principle align and interconnect the clay particles into chains before and during polymerization. To our knowledge this specific combination of materials had not been mentioned previously in the literature. The bonding between magnetite and the clay would be done by electrostatic forces either between positively

charged magnetite and the negatively charged clay surface, or between negatively charged magnetite and the positively charged rim of the clay (Figure 16).

Synthesis of the magnetite nanoparticles was performed according to the Massart method [36] where an acidic solution of $FeCl_2$ and $FeCl_3$ was titrated against NH_4OH. Due to the amphoteric behavior of magnetite it is possible to control the surface charge by adjusting the pH. An acidic solution renders the particles positively charged while a basic solution makes them negative. TEM-microscopy (Figure 17) of the particles showed a fairly homogenous particle size distribution centered around 10 nm.

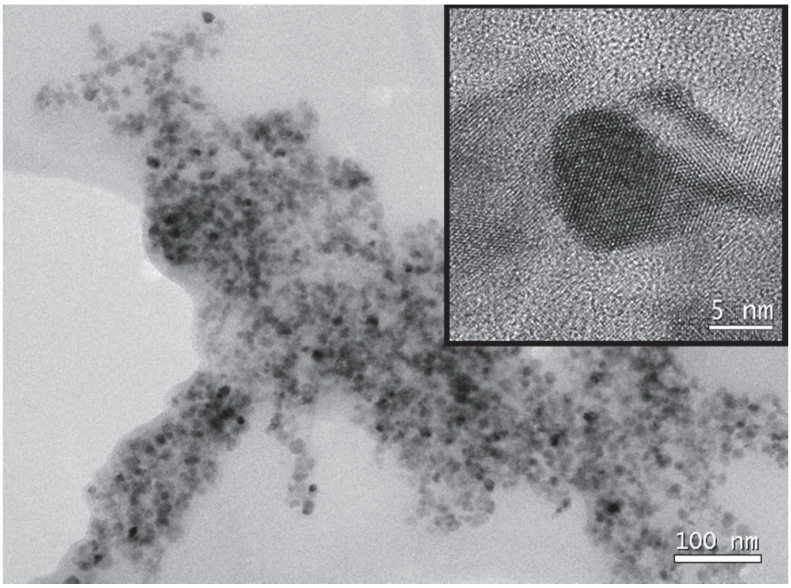

Figure 17 *TEM-micrograph of the magnetite nanoparticles. Inset shows a close-up image of two particles lying on top of each other. The scale bars are 100 and 5 nm, respectively.*

Much effort went into finding the optimum procedure for peptizing the nanoparticles. One important restriction was that if surfactants should be used they would need to have as low impact as possible on the polymerization process. We found that a simple basic solution of pH=10 created a stable suspension of negatively charged particles. Since the preparation of NC-gels occur at this very pH level the polymerization would be disturbed to a very small degree. The first ferro-NC-gel (FNC-gel) we prepared displayed the same rubber-like behavior as the pure NC-gels, leading us to conclude that the system was ready to be explored further.

To attain knowledge about the dynamics during polymerization we performed an *in situ* SAXS-study at the Dubble beam line at ESRF in Grenoble. This was the first x-ray measurements we performed on the NC-gels because only synchrotron sources would give enough intensity in the x-ray beam for us to be able to "see" the clay particles, due to the large absorption by water.

First a pure NC-gel containing 2 wt.% Laponite was measured continuously with SAXS during polymerization inside a glass capillary, with an exposure time of 10 minutes. The shape of the SAXS curves from this sample, shown in Figure 18, did not change within the time frame of polymerization which indicated that there were no inhomogeneities appearing, and thus the cross-linking with Laponite was homogenous through the sample. Furthermore the slope of the curves at intermediate q-range was close to -2.0 which was also an indicator of well-dispersed clay platelets [34]. The curves also contained a small kink around 0.16 nm^{-1}, which was due to scattering from entities with a size of around $2\pi/q \approx 40$ nm (cf. section 2.2.2).

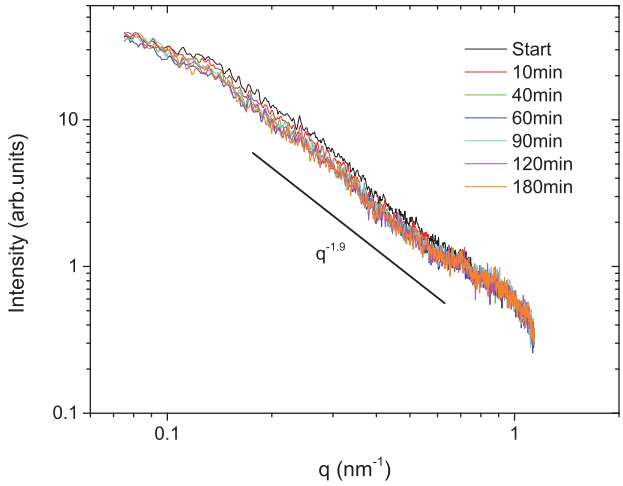

Figure 18 *In situ SAXS curves of a 2 wt.% NC-gel during polymerization.*

To find out if the kink was produced by clay particles or polymer coil "pseudo particles" we measured the gel during stretching, from 0 % and all the way up to 500 % of its original length, to uncoil the polymer chains. If the kink disappeared, it most probably originated from the polymer particles. The curves of the stretched NC-gel are shown in Figure 19.

They were made by integrating the 2D-images in sectors along **q** perpendicular to the stretching direction (i.e. horizontal direction in the inset of Figure 19). At higher strain the kink moved to higher angles, i.e. the size of the unknown entities decreased. At a strain of 500 % (near the breaking limit) the kink disappeared, indicating that the kink did not originate from clay particles, but from polymer coils that were now stretched out to their maximum length.

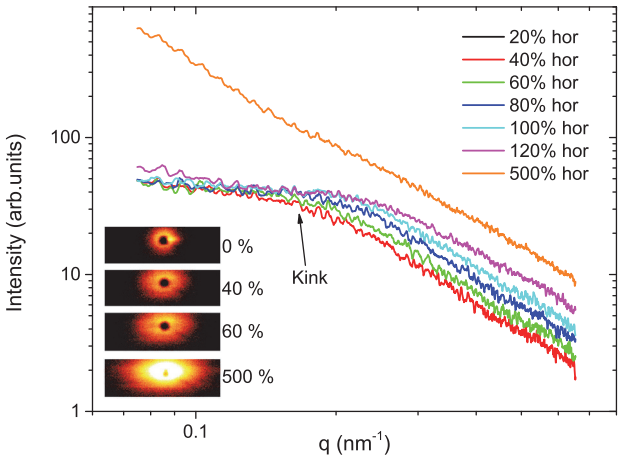

Figure 19 *SAXS-curves from stretching the gel in several steps from 20 to 500 %. Inset shows some of the corresponding scattering patterns.*

This initial study provided important information about the system, but in order to elucidate better the inner structure of these systems, higher clay concentrations were needed. Consequently FNC-gels containing 4 wt.% magnetite and 2 wt.% Laponite were studied with in situ SAXS during polymerization with or without an applied magnetic field of approximately 1 T. Figure 20 shows the scattering pattern from two of these FNC-gels. The upper panel a) shows the resulting scattering pattern from the gel polymerized in absence of a magnetic field (FNC-1). The scattering pattern is seen to be isotropic (circular) apart from an excess signal just on top of the beam center (shown with a black cross), due to a not fully optimized beam stop.

The second gel, FNC-2, was in contrast to FNC-1 polymerized inside a magnetic field, and the x-ray exposure was performed with the field on. The resulting scattering pattern in Figure 20b shows a distinct anisotropic pattern at low **q**. The anisotropy is caused by the

shape of the superstructure of the magnetite nanoparticles when they align into long chains. Since the angular scale (or **q**) varies inversely with dimensions in real space, the pattern will have strong bands perpendicular to the chains. In this case the magnetic field and the resulting chains are oriented along the horizontal direction in Figure 20.

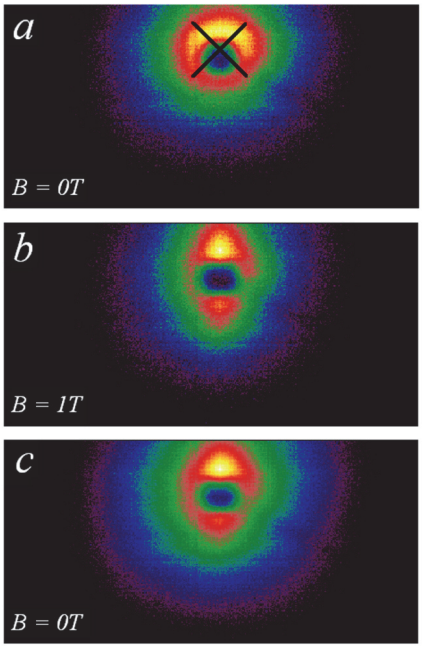

Figure 20 *2D scattering images from FNC-gels. (a) An FNC-gel polymerized in absence of magnetic field. The black cross indicates the beam center. (b) An FNC-gel polymerized in a field of approximately 1T, and measured in the same field. (c) The same FNC-gel as in b) measured without magnetic field.*

After the first exposure FNC-2 was put outside the magnetic field for 3 hours, and measured again in absence of a magnetic field. The resulting scattering pattern, shown in Figure 20c, also has strong anisotropic characteristics, indicating that the dispersed magnetic nanoparticles were permanently aligned. Performing sector integration of the scattering pattern from FNC-2 in the vertical and horizontal direction with a sector width of 20 degrees resulted in the curves seen in Figure 21a. The vertical direction clearly has a stronger signal at low q (<0.2 nm^{-1}) while the intensity converges towards the horizontal direction at higher angles (due to probing of smaller length scales which are unaffected by the alignment). The sample was measured again 7 months later in the x-ray lab at NTNU.

Interestingly the pattern was still anisotropic (Figure 21b), meaning that the magnetite particles were still aligned into chains. This is an interesting behavior when taking into account that the sample contained mostly water and a highly flexible polymer network that would be expected to promote diffusion back to an isotropic state. The reason why this did not occur can be that the magnetite particles were in fact attached to the Laponite particles. Since the Laponite is more or less stationary in the polymer matrix the magnetite will behave likewise.

From these data there are indications that the scattering pattern also contain information from the clay orientation, cf. studies by Shibayama et al. [37]. However, this would require more detailed studies, using both SAXS and SANS techniques, which was found to be less feasible within the time scope of this thesis.

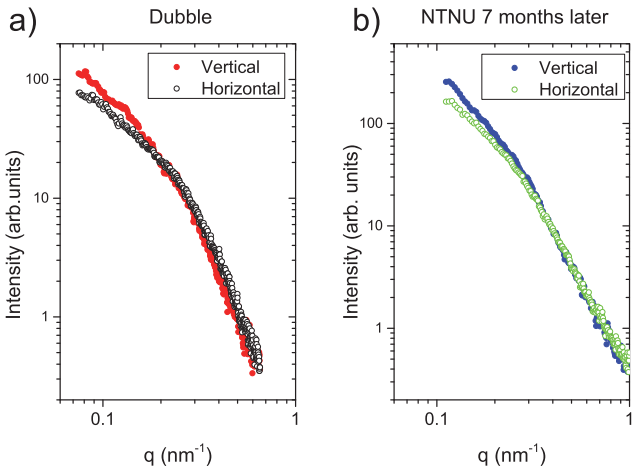

Figure 21 *SAXS curves of FNC-2 measured at two different times. Sector integration was performed in the vertical and horizontal direction on similar scattering patterns as shown in Figure 20.*

3.1.4 Photopolymerization

The polymerization of PNIPA is most easily carried out using the free radical technique. This means, however, that the reaction is controlled by temperature in the case for the KPS-initiator utilized in this study. For our *in situ* SAXS studies we wanted to develop a simple setup that would make it possible to control the polymerization reaction using UV-light. After searching through the literature for non-toxic UV-reactive photoinitiators we decided to use the organic biomolecule riboflavin-5'-phosphate (R5P), a derivative from vitamin B_2. Exposure to UV-light turns the molecule into a radical which can then start the polymerization reaction in the same manner as KPS. But whereas the KPS initiated reaction proceeds until there is no monomer left, the R5P molecule is only a radical while exposed to UV-light. Figure 22a shows a comparison between a polymerized and a non-polymerized sample. The yellow color due to R5P (left vial) disappears as the polymerization reaction proceeds. We investigated in more detail what was the most prominent wavelength to have for polymerization, and found blue light (not UV) the most effective. Thus this process can also be performed with sunlight, which we confirmed separately. The right picture in Figure 22 shows several NC-gel and FNC-gel samples exposed to a fluorescent UV-light source in one of the experiments. The rest of the samples were prepared using a mercury-lamp which emits both blue light and UV.

However, the resulting NC- and FNC-gels had inferior mechanical properties than the ones produced with temperature induced polymerization using KPS as initiator. For this reason we decided not to develop the procedure further for this particular project.

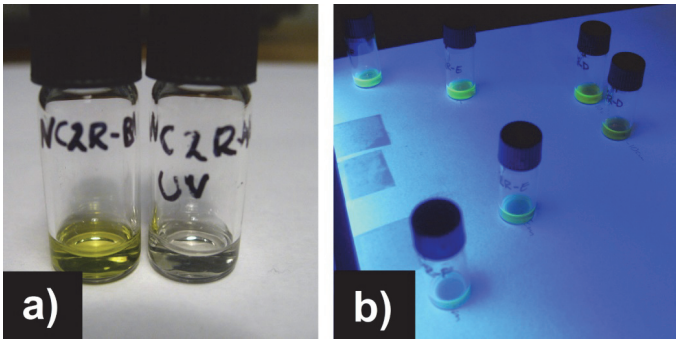

Figure 22 *(a) Picture of NC2R-gels before (left) and after (right) UV-induced polymerization. (b) Several samples exposed to a low power UV-light.*

3.1.5 Thermoresponsive nanoparticles

In Paper VII thermoresponsive nanoparticles made of triblock polymers were synthesized and characterized using various techniques. The system was similar to the NC-gels studied, where PNIPAAM, arranged into nanometer sized subdomains, was dispersed in water. In this case the polymeric part consisted of relatively short polymer chains built up of three parts. One amphiphilic midsection flanked by a hydrophobic and a charged tail group to either side. The combined physical properties of the three sub-chains made them associate into complex coacervate micelles, which displayed both responsiveness towards temperature changes and salt concentration.

My contribution to the work included performing small angle neutron scattering (SANS) experiments on the nanoparticles, which were dispersed in various surfactant concentrations at different temperatures. This was performed with our in-house instrument, SANS, at IFE. The results indicated that the micelles consisted of a core made of the hydrophobic chains, with the other two sub-chains making up the corona of the particles. By adding a charged surfactant to the dispersion, more and more of the charged tail groups interacted with the core, leading to looping of the triblock chains, and a decrease in particle size.

3.2 Polystyrene-clay NCs: A fresh start

3.2.1 Introduction

Although the NC-gels described up to now have highly interesting properties they have some disadvantages in terms of manipulation and practical applications. First of all the NC-gels were not compatible with electrical field induced alignment of the Laponite nanoparticles. Secondly, any difference in mechanical properties arising from the superstructure of the nanoparticles would be difficult to measure with any accuracy because the gels showed non-constant mechanical properties. The fact that the water content of the gels also affected the properties to a large extent made it unpractical to perform accurate measurements because the whole setup must have been located inside a closed container with controlled humidity. Lastly, for these gels we would be limited to Laponite clay only, since other types of clay such as Li-Fluorohectorite (Li-Fh) failed to produce similar nanocomposite structures using the same procedures for preparation.

In view of this we shifted our aim towards purely hydrophobic polymers that could more easily be manipulated. We therefore chose to work with the widely used polymer polystyrene (PS). It could be polymerized from the liquid monomer styrene at normal pressures and not too high temperatures (60-120 °C), in sharp contrast to other important polymers such as polyethylene and polypropylene that are produced from gas phase. Being able to synthesize PS using bulk polymerization was also highly beneficial, since there would be no need for solvents, meaning that the polymerized samples could be shaped by the polymerization vessel, in our case square-shaped glass capillaries. The dielectric constant of styrene was also lower than the one for clay which would make the E-field alignment feasible. We could now also use other types of clay nanoparticles which would give us more diversity.

3.2.2 E-field induced alignment

We first chose to include Li-Fh clay, since this clay is fundamentally different than Laponite, having a much larger size distribution and much larger cation exchange capacity (CEC). We would thus be able to study two materials most probably at each end of the scale regarding their mechanical and thermal properties. After preparing surface modified versions of Fh and Laponite we performed the first testing of E-field alignment of the clays in liquid styrene. Microscope snapshots from aligning org-Fh suspended in styrene can be

seen in Figure 23. The left image shows the initial random dispersion of several micrometer sized org-Fh agglomerates before the E-field was applied. The right image shows the resulting chain/column formation after a 500 Hz AC-field of around 650 V/mm was applied from top to bottom. A similar dispersion using org-Lp showed the same behavior.

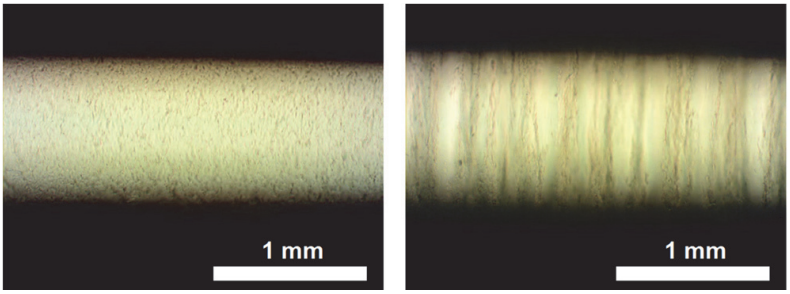

Figure 23 *Electric field induced alignment of org-Fh in liquid styrene from the initial random dispersion (left) to chain like structures (right). The direction of the E-field is from top to bottom in the pictures.*

After the preliminary and successful experiments our custom setup for polymerization of the samples inside an electric field was developed. The setup is described earlier in the thesis in section 2.1.2 and was partly inspired by the work performed by Qi et al. [38]. A large array of anisotropic nanocomposites, using two other clays as well (Hectorite and Na-Montmorillonite), were prepared and studied with a variety of tools such as TGA, SAXS/WAXS, XMT, and mechanical testing. This part of the thesis led to the work presented in Paper II and Paper III, and in one of the main sections of Paper V.

3.2.3 Polypropylene-clay nanocomposites

In Paper VI melt-intercalated PNCs, made of polypropylene (PP) and Cloisite® 20A organoclay, were studied with in situ WAXS. One of the aims with the described work was to recreate some interesting results reported by Kim et al. [39] and Park et al. [40] who worked with similar systems. These authors found that the Cloisite® clay exfoliated when the PP nanocomposites were melted inside an alternating electric field (AC-field), whereas only alignment of the clay was observed when a constant DC-field was applied. However, despite several experiments to try to recreate Kim and Park's results, we did not observe similar behavior. A change of around 5 % in basal spacing was detected, but no exfoliation occurred. Furthermore, this behavior was found to not depend on whether AC- or DC-fields were employed for particle alignment.

3.3 Nylon 6/clay NCs

3.3.1 Introduction

After the successful work on the anisotropic PS-clay composites we decided to include other types of polymers in our portfolio. Nylon 6 was the immediate choice after PS due to its also widespread use and industrial importance, and relative ease of fabrication. Nylon 6/clay nanocomposites (N6NC) are also well-known (cf. section 1.1) but the use of E-field assisted self-assembly of clay in nylon matrices has to our knowledge not been reported.

Nylon 6 is made from ring opening polymerization of melted ε-caprolactam (Figure 24). At around 260 °C, in the presence of a small amount of water (or any chemical with a hydroxyl group), ε-caprolactam reacts with a water molecule by opening up its peptide bond (O=C-NH), and is via a number of steps (not shown here) transformed to an amino acid.

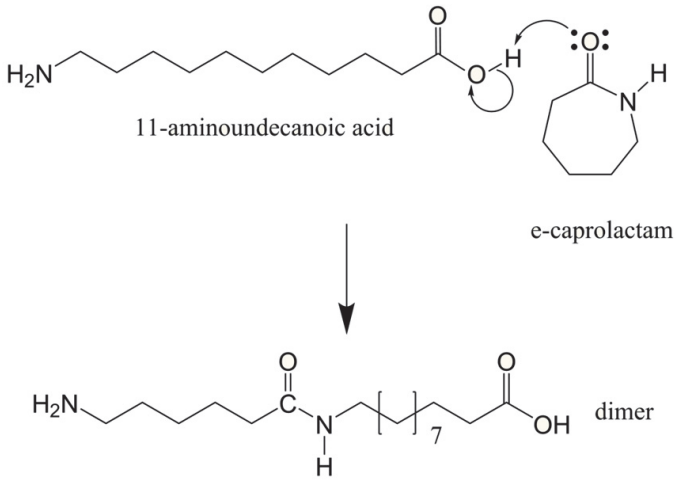

Figure 24 *Simplified reaction scheme showing the reaction, between ε-caprolactam and the hydroxyl group of 11-aminoundecanoic acid, which initiates the polymerization of nylon 6 by creating a dimer that can continue to react with ε-caprolactam.*

The next ε-caprolactam molecule can then either react with a new water molecule, or react with the acidic hydrogen in the newly formed amino acid (see Figure 24). The latter process results in a dimer that can continue to react with more ε-caprolactam molecules, and eventually turn into a long polymer chain. Based on the synthesis of nylon 6/clay

nanocomposites developed by Usuki et al. [41], instead of using water as the polymerization initiator, we decided to co-polymerize nylon 6 with 11-aminoundecanoic acid (11-acid) which would also serve as the surfactant for the surface modified clays. The 11-acid would fill three roles in the synthesis being used as the polymerization initiator, co-polymer, and surfactant. This approach would lead to direct bonding between the polymer and the clay platelets, and facilitate exfoliation.

Due to the high polymerization temperature of nylon 6, of around 260 °C, we could not use the same setup as when preparing the PS-clay nanocomposites (oil bath). In addition all the reactants were in a solid state at room temperature which complicated matters further with regards to being able to produce dense and homogenous samples. These difficulties were however solved, and the results of the preliminary synthesis and characterization of non-aligned nylon 6/clay nanocomposites are presented in Paper IV. Contrary to the findings in Paper II, which showed that yield strength and compressive modulus of polystyrene-clay nanocomposites decreased as the surface charge of the clay increased, we observed here the exact opposite: A larger improvement in mechanical properties was seen when the surface charge increased.

3.3.2 Electrode setup for in situ polymerization

The prospects of performing E-field alignment of the clay inside the nylon 6 matrix were also studied. The high polymerization temperature of the N6NCs posed a problem when solving how to apply an electric field at temperatures exceeding 260 °C, while still maintaining a secure and user-friendly setup. The high voltage needed for the E-field, between 1000 and 3000 V, required well-insulated electrodes and connecting wires. Since most wire insulators are made of polymers that degrade and may catch fire at 260 °C, we could not put these into the oven used for polymerization of the non-aligned samples. We came up with a solution where the capillary and the electrodes were heated inside a special high-precision micro-furnace used for optical in situ microscopy studies (Mettler FP900 Thermosystem with an attached FP82 hot stage). With this setup the wires would be separated from the heating compartment and kept at near room temperature. The hot stage was capable of reaching 375 °C, a temperature well above our needs.

3.3.2.1 Detailed description of the setup

The electrodes (Figure 25a and b) were made of two 10 cm long and 2 mm thick square shaped rods, cut from 2 mm thick aluminium sheets. They were ground and polished to fit

inside thick-walled square shaped glass capillaries with inner diameter of 2 mm (Figure 25a). The electrodes were put into the capillaries with a 4 cm protruding section which wire was soldered onto. The temperature of the protruding ends of the electrodes (and hence the integrity of the soldered joints) was lowered to around 100 °C by convection to the surrounding air, by keeping them outside of the furnace (Figure 25d). The wiring was further secured with two layers of heat-shrinkable tubing, which also served as insulation of the protruding ends of the electrodes. Fimo® clay, a polymer based playdough was cast around the electrodes, which were kept parallel with their walls perpendicular to each other, and spaced 2.4 mm apart with an empty glass capillary (Figure 25c). The whole setup was put into an oven for 30 min at 110 °C to cure and harden the Fimo® clay.

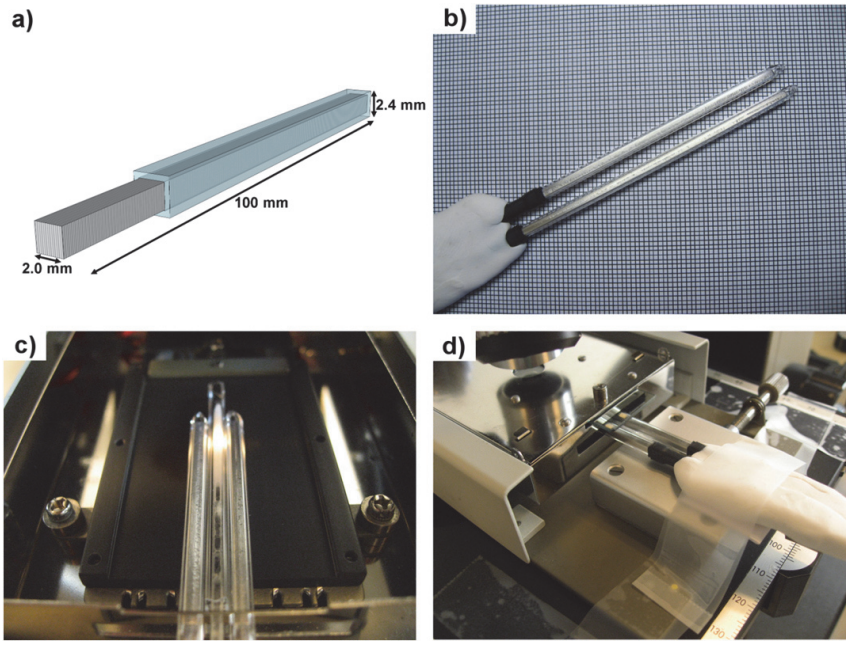

Figure 25 *(a) Sketch of the electrodes and the capillaries used, (b) the finished insulated electrodes, (c) placement of the electrodes inside the micro-furnace (a 2.4 mm glass capillary is inserted between the electrodes), (d) the electrodes protrude out from the closed micro-furnace.*

3.3.2.2 E-field alignment

The electrode setup was first tested and confirmed to produce a field strong enough to align CTAB-modified Hectorite clay (CTAB-HT) dispersed in silicone oil. At the maximum alternating electric field of 420 V/mm for this setup and 500 Hz the clay particles aligned into chains, shown in the microscopy pictures in Figure 26.

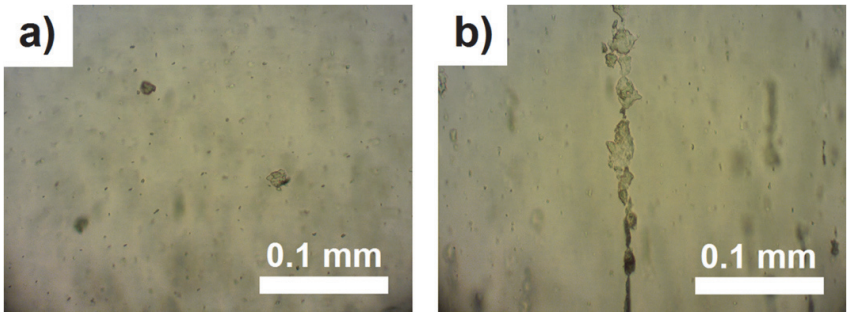

Figure 26 *Before (a) and after (b) E-field alignement of org-HT particles dispersed in silicone oil.*

The next step was to test the setup under heating with an applied electric field. A capillary, filled with 5 wt.% 11-acid modified Li-Fluorohectorite clay (11-Fh) dispersed in ε-caprolactam, was inserted between the electrodes, and monitored with an optical microscope during heating up to 260 °C. At 70 °C the monomer matrix melted, and at 110 °C small clay particles started to float around in the melted monomer. When the sample reached 150 °C an alternating electric field of 420 V/mm and 500 Hz was applied, but no movement of the clay particles with respect to the E-field (characteristic of dipolar particles) occurred. At higher temperatures the system remained identical. The only movement of the particles we could see was caused by convection currents.

This result was a little puzzling because it would mean that either the surface modification of the clay itself changed the dielectric constant of the clay particles to a large extent, or that the dielectric constant of melted ε-caprolactam was higher than for clay. A third scenario could as well be a mix of the former two. According to the relation in eq. (1) in section 2.1.2, polarization of the clay particles demand a lower dielectric constant of the surrounding medium. If the opposite is true the surrounding medium will be polarized instead. The outcome of such a system is difficult to predict (cf. the alignment of Laponite clay in water in section 3.1.2). However, several combinations of clay and matrix, as well

as different frequencies of the alternating E-field, were therefore tested in the same manner as the initial experiment with CTAB-HT. The main results are summarized in Table 2.

Table 2 *Results of applying an E-field to several clay dispersions.*

Clay type	Matrix	Chain formation?
CTAB-HT	Silicone oil	Yes
11-Fh	ε-caprolactam	No
Li-Fh	ε-caprolactam	No
CTAB-Fh	ε-caprolactam	No
11-MMT	Silicone oil	Yes

LiFh and CTAB-Fh both dispersed in ε-caprolactam failed to be affected by the electric field, while 11-MMT dispersed in silicone oil, on the other hand, displayed clear evidence of E-field induced polarization. No effect of lowering or increasing the frequency of the E-field was noticeable. These results indicated that it was most probably the dielectric constant of ε-caprolactam which was the source of error in the former alignment experiments. Apparently the dielectric constant was higher than for clay which would make alignment impossible using E-fields, similar to what happened when we tried aligning Laponite clay in water (cf. section 3.1.2).

3.3.2.3 Measurements of dielectric constants

To elucidate why the E-field alignment failed, the dielectric constant of several types of clay and other relevant materials/liquids was measured with a customized setup. The capacitance over two plate electrodes, with the volume between occupied by the material being examined, was measured with an automated Philips PM6304 RCL meter at 100 kHz. The dielectric constant, ε, was derived from the measured capacitance, according to the conventional relation $\varepsilon = C \cdot d/\varepsilon_0 A$, where ε_0 is the dielectric constant of vacuum (8.85×10^{-12} Fm^{-1}), d is the distance between the electrodes, and A the contact area of the electrodes [16]. The resulting dielectric constants are listed in Table 3.

Solid ε-caprolactam has a lower value than all clays, meaning that if the clays were immersed in liquid ε-caprolactam they should be polarized inside an E-field. However, when ε-caprolactam was poured into the electrode cell in melted form (around 100 °C) the measured dielectric constant shot upwards to approximately 13. Upon cooling down to room temperature this value decreased to 0.9. This latter value is higher than for the powdered sample (0.4) which can be related to the higher filling fraction in the cell for the

melted sample. A reasonable explanation for the increase in dielectric constant in the melted state may be that the polar ε-caprolactam molecules are then free to move around resembling the behavior of the high-capacitance liquids ethanol and water, which were measured with constants of 30.3 and 79.1 respectively.

Table 3 *Measured dielectric constants of different materials and substances at a frequency of 100 kHz.*

Material	100 kHz
Laponite XLG (pure clay)	9.4
LiFh (pure clay)	3.7
org-Lp	1.3
org-HT	1.5
org-MMT	2.0
11-Lp	1.8
11-FH	2.5
11-MMT	0.6
11-HT	1.8
ε-caprolactam powder	0.4
ε-caprolactam melted @ 100°C	12.9
Melted ε-caprolactam cooled down to room temperature	0.9
Silicone oil	1.7
Styrene	1.8
Water	79.1
Ethanol	30.3

These results clearly seem to indicate a temperature variation in the dielectric constant for ε-caprolactam. But it was, however, observed that the measured capacitance increased likewise when the conductive parts of the electrode cell were heated by a hot air gun. We believe this is due to changes in conductivity and expansion of the metal parts of the cell, and thus the measured capacitance is perturbed. Due to these implications we do not have confidence in the resulting values for ε-caprolactam in melted state, but we still believe in our suggested explanation for the unexpected results. We would have preferred to pursue these matters further, but since this study was performed at the very end of the doctoral work we had limited time to do so. Assembly of a modified electrode cell, resistant to temperature effects may have helped leading to a firm conclusion.

3.4 SAXS/WAXS Graphical user interface (GUI) for Matlab

A lot of the work performed in this thesis has been devoted to x-ray scattering experiments, thus large numbers of data files have been created and integrated for further analysis. The integration of the numerous files was performed with the free program Fit2D, written by Hammersley et al. [42]. This program has a limited ability to integrate file series, but it has the quite useful function that it can be controlled by text-based macros. Custom routines and scripts that could output such macros were therefore written in Matlab. A graphical user-interface (GUI), shown in Figure 27, was also created in Matlab to simplify the whole integration process.

Figure 27 *The Matlab based graphical user-interface of the integration program.*

In the GUI the user can quickly set up the program to integrate data in a number of ways, including sector-integration in two directions simultaneously with or without background corrections. An option to create postscript image files with one click is also included together with an option to plot all the 1D-files present in the current folder with Matlab. A panel in the GUI is also displaying messages and errors to the user, as shown in the example in Figure 27 where the message “Folder OK, waiting for input…” confirms that

the selected folder path contains no open spaces, and is thus an accepted location of the data files. A single output file with all the data sorted by time of data acquisition is created automatically as well, which is extremely time conserving when importing and plotting large numbers of data files together in graphing software such as Origin.

Refining the underlying code has been an on-going project throughout the doctoral work, mainly to incorporate new features and support for more file types. (This is also the reason for the not-so fancy name of the program, “TestGUI5”, because it continued to live on as an unfinished test-program) Another important aspect has been to make the program compatible with several versions of Matlab, and to make it as fail-safe as possible in order for other students to use it. The main code for creating the Fit2D-macros was based on a Matlab-code written by Dr. Henrik Hemmen, and in his spirit the code developed in the present work is shared in Appendix B. This might prove beneficial for future students, or others working with large sets of data files. The code is, however, drastically stripped down when shown here because it would have been too lengthy to be presented at its full length in this thesis.

4 Concluding remarks

The aim of this thesis was to investigate functional polymers with embedded nanoparticles. Among a vast field of materials with highly diverse properties polymer clay nanocomposites (PCNs) were selected. The goal was to synthesize and characterize PCNs in which the orientation of the clay particles was controlled. Guided self-assembly using external electric or magnetic fields was investigated as a means to produce novel anisotropic composites.

The first system we worked on was nanocomposite hydrogels (NC-gels), first developed by Haraguchi et al. [23]. The original plan was to use external electric fields to align the clay particles inside the polymer matrix, but this turned out not to be possible because of the large fraction of water (~90 wt.%) in these materials. From TEB-measurements we observed alignment of clay particles in water, but the alignment persisted only on timescales of microseconds. The idea of alignment using electric fields was therefore discarded for this system, and the focus was rather shifted to employing magnetic fields instead. However, the work on this system led us on to other pathways when we observed phase segregation during polymerization, which turned out to be induced by tiny amounts of oxygen present in the samples. This work is presented in Paper I.

Further work on the NC-gels included embedding magnetic nanoparticles for the preparation of anisotropic NC-gels, and the development of a photopolymerization synthesis to be used during *in situ* synchrotron studies. Both of these works were interesting, but were stopped early due to several factors described earlier in this thesis.

Polystyrene-clay and nylon 6/clay nanocomposites received the most attention in this thesis. A range of surface modified clays and polymer-clay samples were synthesized and carefully analyzed using different techniques. One of the main findings was a linear correlation between the surface charge of the clays and several physical properties such as high temperature resilience and mechanical strength. For the polystyrene-clay system a low surface charge led to improvements, whereas the nylon 6/clay system showed the exact opposite trend. Furthermore, the polystyrene-clay system turned out to be susceptible to electric fields, and this was used to prepare anisotropic nanocomposites. It was observed anisotropy in the mechanical properties for two of the samples containing Laponite clay, while the rest of the samples did not show similar features. However, the alignment of clay

into chain-like structures in these nanocomposites had a somewhat negative impact on the mechanical properties, while in the nylon 6/clay system improved mechanical properties were observed when the clay was well-dispersed. On the other hand, the nylon 6/clay precursors were not affected by electric fields. We believe the reason for this was an increased dielectric constant as the monomer ε-caprolactam was melted. These topics are presented in Paper II, Paper III, and Paper IV.

There are still several unanswered questions that further work could have shed light onto. The effects of clay concentration in the nanocomposites for instance, were barely investigated due to limited time at the synchrotron facilities. Transmission electron microscopy (TEM) studies of both aligned and non-aligned polystyrene-clay nanocomposites would have been excellent as comparisons to the WAXS and XMT results. An effort was made to prepare TEM-cuts of the E-field aligned samples. It turned out, however, to be very difficult to achieve sufficiently clean cuts of these samples because the cuts quickly crumpled and splintered into fibers. A greater effort to achieve suitable sample-cuts is planned in the near future. Finally, a more detailed investigation of why the E-field alignment did not work for the nylon 6/clay nanocomposites is desired. Since these nanocomposites were of the exfoliated type it would have been highly interesting to see if anisotropy in the mechanical properties would appear.

5 Contribution to the scientific papers

Paper I: *Oxygen-Controlled Phase Segregation in Poly(N-isopropylacrylamide)/Laponite Nanocomposite Hydrogels*

My contribution to this scientific paper includes planning and performing all experiments and syntheses, data analysis, being the primary author of the manuscript and responsible for interpretation of the results, as well as handling the submission process.

Paper II: *The effect of clay surface charge on the emerging properties of Polystyrene-clay nanocomposites*

My contribution to this scientific paper includes planning and performing all experiments and syntheses, data analysis, and being the primary author of the manuscript and responsible for interpretation of the results. The submission process was handled by the supervisor, Prof. Kenneth D. Knudsen, because the Journal of Physical chemistry did not allow people without a PhD handle it.

Paper III: *Anisotropic polystyrene-clay nanocomposites: Synthesis, characterization and mechanical properties*

My contribution to this scientific paper includes planning and performing all experiments and syntheses, data analysis, modifications to the high-temperature furnace used for *in situ* SAXS/WAXS studies at Max-Lab, development of the electrode cells used for E-field alignment, development of the customized compression apparatus, as well as being the primary author of the manuscript and responsible for interpretation of the results. I will also handle the submission process.

Paper IV: *Synthesis and characterization of nylon 6/clay nanocomposites using different 2:1 smectic clays*

My contribution to this scientific paper includes planning and performing all experiments and syntheses, data analysis, development of the customized compression apparatus, as well as being the primary author of the manuscript and responsible for interpretation of the results. I will also handle the submission process.

Paper V: *Dipolar ordering of clay particles in various carrier fluids*

This paper was developed honoring the first international meeting arranged in Cuba on the topic of Complex Matter Physics, in March 2012. The journal "Revista Cubana de Fisica" is not the typical channel for publications due to its limited range and availability, but we felt honored to be asked for a contribution, and submitted this short paper related to the topics of the talks we presented during the meeting.

My contribution includes being the author of one of the subsections (*Clays in polystyrene*), sample preparation, WAXS-experiments, as well as participating in the discussions concerning the results and taking part in the writing process.

Paper VI: *Different Aspects of Electrically Activated PP/Clay Nanocomposites*

My contribution to this scientific paper includes being responsible for the Pseudo-Voigt analysis of the *in situ* WAXS data, involvement in the WAXS-experiment, as well as participating in the discussions concerning the results and taking part in the writing process.

Paper VII: *Complex coacervate micelles formed by a C18-capped cationic triblock thermoresponsive copolymer interacting with SDS*

My contribution to this scientific paper includes performing the small angle neutron scattering (SANS) experiment, involvement in the interpretation of the SANS-results, as well as taking part in the writing process.

References

[1] Utracki, L.A., *Clay-Containing Polymeric Nanocomposites*. Vol. 1. 2004, Shrewsbury, U.K.: Smithers Rapra Technology. 456.

[2] Josmin, J.P., et al., *Polymer Composites*. Vol. 1. 2012: Wiley-VCH Verlag GmbH & Co.

[3] Jaatinen, P., T. Manninen, and M. Ripatti, *Pole shaft for a cross-country ski pole*, 1997, Exel Oy, Mantyharju, Finland.

[4] Mouritz, A.P., et al. Review of advanced composite structures for naval ships and submarines. *Compos. Struct.* **2001**, 53, 21-41.

[5] Vallbo, S. Material selection considerations for polymer composite structures in naval ship applications. *Journal of Sandwich Structures & Materials* **2005**, 7, 413-429.

[6] Kelly, A. Very stiff fibres woven into engineering's future: a long-term perspective. *Journal of Materials Science* **2008**, 43, 6578-6585.

[7] Okada, A. and A. Usuki Twenty years of polymer-clay nanocomposites. *Macromol. Mater. Eng.* **2006**, 291, 1449-1476.

[8] Kaviratna, P.D., T.J. Pinnavaia, and P.A. Schroeder Dielectric properties of smectite clays. *J. Phys. Chem. Solids* **1996**, 57, 1897-1906.

[9] Fossum, J.O. Physical phenomena in clays. *Physica A* **1999**, 270, 270-277.

[10] Bakk, A., et al. Viscosity and transient electric birefringence study of clay colloidal aggregation. *Phys. Rev. E* **2002**, 65, 9.

[11] Knudsen, K.D., et al. Pore characteristics and water absorption in a synthetic smectite clay. *J. Appl. Crystallogr.* **2003**, 36, 587-591.

[12] da Silva, G.J., et al. Hydration transitions in a nanolayered synthetic silicate: A synchrotron x-ray scattering study. *Physical Review B* **2003**, 67.

[13] Knudsen, K.D., et al. Small-angle neutron scattering from a nano-layered synthetic silicate. *Physica B-Condensed Matter* **2004**, 352, 247-258.

[14] Fossum, J.O., et al. Intercalation-enhanced electric polarization and chain formation of nano-layered particles. *Europhys. Lett.* **2006**, 74, 438-444.

[15] Hemmen, H., et al. The Isotropic-Nematic Interface in Suspensions of Na-Fluorohectorite Synthetic Clay. *Langmuir* **2009**, 25, 12507-12515.

[16] Wang, B.X., et al. Electrorheological properties of organically modified nanolayered laponite: influence of intercalation, adsorption and wettability. *J. Mater. Chem.* **2009**, 19, 1816-1828.

[17] Rozynek, Z., et al. Dynamic column formation in Na-FLHC clay particles: Wide angle X-ray scattering and rheological studies. *J. Phys.: Conf. Ser.* **2009**, 149, 012026.

[18] Svåsand, E., *Nanoparticle complex fluids*. 2008, Oslo: University of Oslo.

[19] Wang, W., et al. Complex coacervate micelles formed by a C18-capped cationic triblock thermoresponsive copolymer interacting with SDS. *Soft Matter* **2012**, 8, 11514-11525.

[20] Mauroy, H., et al. Oxygen-Controlled Phase Segregation in Poly(N-isopropylacrylamide)/Laponite Nanocomposite Hydrogels. *Langmuir* **2013**, 29, 371-379.

[21] Makino, K., J. Hiyoshi, and H. Ohshima Effects of thermosensitivity of poly (N-isopropylacrylamide) hydrogel upon the duration of a lag phase at the beginning of drug release from the hydrogel. *Colloids and Surfaces B-Biointerfaces* **2001**, 20, 341-346.

[22] Haraguchi, K., et al. Mechanism of forming organic/inorganic network structures during in-situ free-radical polymerization in PNIPA-clay nanocomposite hydrogels. *Macromolecules* **2005**, 38, 3482-3490.

[23] Haraguchi, K. and T. Takehisa Nanocomposite hydrogels: A unique organic-inorganic network structure with extraordinary mechanical, optical, and swelling/de-swelling properties. *Adv. Mater.* **2002**, 14, 1120-1124.

[24] Wünsch, J.R., *Polystyrene: Synthesis, Production and Applications*. 2000: iSmithers Rapra Publishing.

[25] Liu, T.X. Melting behavior of isotactic polystyrene revealed by differential scanning calorimetry and transmission electron microscopy. *Eur. Polym. J.* **2003**, 39, 1311-1317.

[26] Galanty, P.G., *Polymer Data Handbook*. 1999: Oxford University Press.

[27] Hemmen, H., et al. X-ray Studies of Carbon Dioxide Intercalation in Na-Fluorohectorite Clay at Near-Ambient Conditions. *Langmuir* **2012**, 28, 1678-1682.

[28] Bhanu, V.A. and K. Kishore Role of oxygen in polymerization reactions. *Chem. Rev.* **1991**, 91, 99-117.

[29] Davis, L.C. The metal-particle insulating oil system - An ideal electrorheological fluid. *J. Appl. Phys.* **1993**, 73, 680-683.

[30] Rozynek, Z., et al. Dipolar ordering of clay particles in various carrier fluids. *Cuban Journal of Physics, Revista Cubana de Fisica* **2012**, 29, 37-41.

[31] Mauroy, H., et al. Anisotropic polystyrene-clay nanocomposites: Synthesis, characterization and mechanical properties. *Manuscript in preparation (June)* **2013**.

[32] Als-Nielsen, J. and D. McMorrow, *Elements of Modern X-Ray Physics*. 2001: John Wiley & Sons, Ltd.

[33] Pusey, P.N., *Neutron, X-rays and Light. Scattering Methods Applied to Soft Condensed Matter*. 2002: North Holland.

[34] Roe, R.J., *Methods of x-ray and neutron scattering in polymer science*. 2000: Oxford University Press.

[35] Teixeira, A.V., et al. Structure and magnetic properties of dilute ferrofluids suspended in gels. *Composites Sci. Technol.* **2003**, 63, 1105-1111.

[36] Massart, R. Preparation of aqueous magnetic liquids in alkaline and acidic media. *Ieee Transactions on Magnetics* **1981**, 17, 1247-1248.

[37] Shibayama, M., et al. Small-angle neutron scattering study on uniaxially stretched poly(N-isopropylacrylamide)-clay nanocomposite gels. *Macromolecules* **2005**, 38, 10772-10781.

[38] Qi, R., X. Jin, and S. Huang Synthesis and Characteristics of Polystyrene-Clay Nanocomposites via In Situ Intercalative Polymerization in a Direct Current Electric Field. *J. Appl. Polym. Sci.* **2010**, 115, 2723-2727.

[39] Kim, D.H., et al. Microstructural evolution of electrically activated polypropylene/layered silicate nanocomposites investigated by in situ synchrotron wide-angle X-ray scattering and dielectric relaxation analysis. *Polymer* **2006**, 47, 5938-5945.

[40] Park, J.U., et al. Time-electric field superposition in electrically activated polypropylene/layered silicate nanocomposites. *Polymer* **2006**, 47, 5145-5153.

[41] Usuki, A., et al. Synthesis of nylon 6-clay hybrid. *J. Mater. Res.* **1993**, 8, 1179-1184.

[42] Hammersley, A.P., et al. Two-dimensional detector software: From real detector to idealised image or two-theta scan. *High Pressure Res.* **1996**, 14, 235-248.

Papers I – VII

I

II

Manuscript accepted by Journal of Physical Chemistry C
27 August 2013

The effect of clay surface charge on the emerging properties of Polystyrene-organoclay nanocomposites

Henrik Mauroy*[a,b], Tomás S. Plivelic[c], Elisabeth L. Hansen[d], Jon Otto Fossum[d], Geir Helgesen[a,b] and Kenneth D. Knudsen*[a,d]

[a]Physics department, Institute for Energy Technology, P.O. Box 40, N-2027 Kjeller, Norway
[b]Department of Physics, University of Oslo, N-0316 Oslo, Norway
[c]MAX IV Laboratory, Lund University, P.O. Box 118, SE-221 00 Lund, Sweden
[d]Department of Physics, Norwegian University of Science and Technology, Hoegskoleringen 5, N-7491 Trondheim, Norway

ABSTRACT: A series of polystyrene-clay nanocomposites, based on two natural clay types (Na-Montmorillonite and Hectorite), and two synthetic clays (Laponite and Li-Fluorohectorite), were prepared via in situ intercalative polymerization after surface modification with an organic ammonium cation (CTAB). The structural characteristics of the organically modified clays as well as the nanocomposites were investigated by means of wide angle x-ray scattering (WAXS), and the thermal properties were studied with TGA. In organically modified clays, the silicate interlayer spacing increases and the magnitude seems to be directly correlated with the amount of clay surface charge. In nanocomposites, polymer intercalation is also observed but partial exfoliation is present, modifying significantly the morphology of the material. The degree of dispersion of the clay platelets, as well as the resulting properties of the nanocomposites, were found again to be systematically, and almost linearly correlated with the intrinsic surface charge of the clays, which varied between 44 and 120 meq/100g. Increased dispersion was seen in the nanocomposites made from clays with low surface charge, here Hectorite and Laponite, suggesting that these can be suitable alternatives to the more employed Montmorillonite for enhancement of thermal properties. The thermal stability was found to be better for the nanocomposites than for the pure polystyrene.

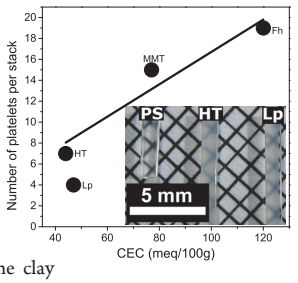

1 INTRODUCTION

In polymer materials science a promising class of high-performance composite materials has been explored during recent years. By combining polymer systems with miniature particles, where at least one of the particle dimensions is in the nanometer range, remarkable modifications in material properties can be achieved. Such polymer nanocomposite materials exhibit improved flame retarding properties[1,2] and mechanical performance[2-4] compared to the pristine polymers. In some nanocomposites, less than one weight percent of nanoparticle filler can drastically modify the overall macroscopic system behavior, provided that the incorporated particles are well-dispersed and their surface can interact sufficiently with the polymer chains.[5] For the enhancement of mechanical properties anisometric filler particles are preferred, especially lamellar types such as exfoliated clay, because the reinforcing effect is strongly related to the aspect ratio (diameter to thickness) of the particles.[6]

In the late 1980s Toyota Motor Company invented a new type of polymer composite[7,8] made by polymerizing ε-caprolactam in the presence of a few weight percent of organically surface treated montmorillonite (MMT) to create a nylon 6-clay nanocomposite with fully exfoliated clay platelets inside the polymer matrix. This material demonstrated superior thermal and mechanical properties compared to conventional nylon 6 composites, due to the intimate mixing of nanometer sized clay particles and polymer chains, and it was quickly utilized in one of their production cars.[8]

Since then many industrially important polymer systems have been explored, such as polypropylene (PP)[9] and polystyrene (PS).[10] PS-clay systems are of interest to employ as model compounds, not only because of the widespread use of PS in connection with engineering and commercial

products, but also because of the amorphous nature of this polymer. Any changes in overall properties will then be due mainly to the additives used. One major complication with PS is that it is hydrophobic and not miscible with clay, making exfoliation and dispersion of the clay particles difficult.[11] The workaround is to render the clay hydrophobic by exchanging the intercalated cations with organic chain molecules, such as alkyl ammonium ions or fatty acids, through a simple cation exchange process.[6] Since the early work on PS-clay by Vaia et al.,[12] extensive studies have been carried out to synthesize and produce compatible PS-clay systems, where the most used techniques involve melt compounding of the neat polymer with surface treated clays, and *in situ* intercalative polymerization.[13]

The latter process can disperse the clay platelets to a larger extent.[11] This technique involves adding clay to the liquid styrene monomer followed by polymerization. The intimate mixing prior to polymerization intercalates styrene molecules into the clay galleries, resulting in a swelled clay structure more susceptible to exfoliation. The degree of further swelling and intercalation of PS-chains are governed by the miscibility between the clay surface and PS. For example, Hasegawa et al.[10] managed to prepare fully exfoliated PS-MMT nanocomposites by using PS co-polymerized with polar oxazoline groups. Fu et al.[14] and Zhu et al.[15] on the other hand, used surfactants with reactive vinyl groups attached to reach a similar and fully exfoliated PS-MMT structure.

The clay mostly used for polymer reinforcement is of the 2:1 type where an octahedral metal-hydroxide sheet is sandwiched between two tetrahedral silicate-sheets sharing apical oxygen atoms. Due to isomorphous substitution in to the clay structure, of Si^{4+}, Mg^{2+} or Al^{3+} by cations with a lower charge, a net negative surface charge is formed on each clay platelet. This charge is balanced by exchangeable cations such as Li^{+}, Na^{+} and Ca^{2+} which are shared between adjacent clay platelets.[16] This arrangement leads to a property called cation exchange capacity (CEC), which varies between different 2:1 clays, and is therefore an important intrinsic property of the clays.

To the best of our knowledge, the range of clay types used in earlier works on PS-clay nanocomposites, prepared with *in situ* intercalative polymerization, is narrow. There is an extensive use of MMT clay[11], but only a few reports using other clays.[1,17-20] In the present work we have therefore aimed to explore in a systematic manner the differences between several 2:1 clays, and to investigate the significance of the effect that the CEC has on the emerging properties of the nanocomposites. Four different types of clay, Hectorite (HT), Laponite (Lp), Li-Fluorohectorite (Fh), as well as MMT were chosen based on their large span in CEC values.

2 EXPERIMENTAL

2.1 Materials

Styrene monomer (≥99%), Benzoyl peroxide (Luperox® A75, 25 % water) and cetyltrimethylammonium bromide (CTAB) (≥98%) were purchased from Sigma-Aldrich and used without further purification. Two synthetic 2:1 clays, Laponite XLG (Lp) and Li-Fluorohectorite (Fh), were kindly donated by Andreas Jennow AB, and purchased from Corning Inc, respectively. Two natural 2:1 clays, Na-Montmorillonite SWy-2 (MMT) and Hectorite SHCa-1 (HT), were purchased from The Clay Minerals Society Repository. These four clays share the same 2:1 phyllosilicate structure. The type of exchangeable cations and the CEC-values of the clays used here and reported by the manufacturers are listed in Table 1.

The lateral size of Fh platelets is large[1] and is during the synthesis in this work limited to ~1 μm by centrifugation, while Lp platelets have a much smaller, and fairly narrow, size distribution centred around 30 nm.[22] MMT and HT platelets lie in between these two extremes, at 0.1-1 μm and 0.1-0.4 μm, respectively.[1,23,24]

2.2 Preparation/synthesis

2.2.1 Organoclays

Table 1 Experimental details of the clays and the amount of CTAB added to the clay.

Clay type	Exchangeable cation†	CEC (meq/100g)†
HT	Na, Mg	44
Lp	Na	47
MMT	Ca,Na	77
Fh	Li	120

† HT, MMT see ref. [16], Lp, Fh see ref. [21]

The clays were surface modified using CTAB through a simple cation-exchange process, where the ammonium cation of CTAB replaces the inorganic cations between the clay platelets. In the present work the amount of CTAB used corresponded to four times the cation exchange capacity (CEC) of the respective clay. The clays were first crushed in a mortar, dispersed in deionized water and stirred at 80 °C for 12 hours in order to exfoliate the clay platelets. Subsequently the suspensions were cooled down and centrifuged at 700G (maximum speed) for 25 minutes to remove non-clay constituents that were present in the natural clays. This treatment also removed clay particles larger than ~1 μm.[25] After centrifugation, the supernatant contained a stable semi-transparent dispersion of exfoliated

clay that did not sediment, and the concentration of clay was determined by evaporating a known volume and weighing the solid residue. Since Laponite undergoes a near complete exfoliation by dispersion in water at room temperature, centrifugation was omitted and the suspension was only stirred at 80 °C for 2 hours.

A predefined amount of CTAB, corresponding to 4×CEC (surplus of surfactant) of each clay, was dissolved in deionized water at 30 °C until the solution turned clear. Subsequently the clay suspensions were heated to 80 °C, and the CTAB-solution was poured gently in under stirring. Flocks of hydrophobic surface modified clay precipitated immediately. The solutions were then stirred at 80 °C for 12 hours, and subsequently left at room temperature for 24 hours to settle. The solutions were decanted and suction filtrated, and the precipitate was washed with 100 mL deionized water, stirred for 1 hour and suction filtrated again. Washing and filtration was repeated up to 10 times to remove any residual CTAB. After each wash cycle the waste solutions were checked for Br-ions (free CTAB molecules) by adding some drops of 0.5 M $AgNO_3$. After the last filtration, the filtrate was dried in an oven at 80 °C overnight, crushed to a fine powder in a mortar, and stored in a sealed container until further studies. The organoclays were labelled org-HT, org-Lp, org-MMT and org-Fh respectively.

2.2.2 *Polystyrene nanocomposites*

The nanocomposites were prepared with *in situ* free radical polymerization of PS, by the following procedure: In a 2 mL glass bottle a certain amount of organoclay, normalized to 0.03 g of the inorganic part of the clay, was dispersed together with 7 mg initiator (Benzoyl peroxide) in 1 mL of styrene monomer. This amounts to 3.2 wt.% of inorganic filler, or roughly 5 wt.% of total organoclay filler (including the surfactant). Pure PS samples were made with the same ratio of monomer to initiator, but without any filler. The solution was vigorously stirred for 2 hours at room temperature, and then for 12 hours at a much lower intensity. Afterwards it was filled in 80 mm long square-shaped glass capillaries with inner dimensions of 1.0 mm.

Subsequently the open end was connected to a water jet pump, to remove air, and sealed with a flame torch. Immediately after sealing, the samples were immersed in a silicone oil bath, which was kept at 95 °C, and left to polymerize for 5 days.

The polymerized nanocomposites were carefully pulled out from the capillaries and labelled PSHT, PSLp, PSMMT and PSFh, respectively. They were studied with wide angle x-ray scattering, optical and electron microscopy, and thermogravimetric analysis. Visual inspection of the samples showed that they were all, except PSFh, semi-transparent with a homogenous white coloring from the clay (see Figure S1 in the supporting information).

2.3 Characterization

2.3.1 *Wide angle x-ray scattering (WAXS)*

WAXS experiments were performed at beamline I911-4 of the MAX-lab synchrotron facility in Lund, Sweden.[26] All data were collected at a wavelength of $\lambda = 0.91$ Å, covering the q-range between 0.1 to 10 nm^{-1} ($q=(4\pi/\lambda)\sin(\theta)$ with 2θ the scattering angle). The detector used was a two-dimensional CCD (165 mm diameter from MarResearch, Inc). *In situ* heating experiments on the nanocomposites were performed using a customized high temperature furnace (Linkam TS1500) for x-ray scattering experiments. These samples were kept inside the capillaries used for polymerization, and heated from 25 to 250 °C at a rate of 10 °C/min.

WAXS-scans of the pure clays were carried out using a NanoSTAR system from Bruker AXS, equipped with a CuKα Xenocs micro source with a wavelength of 1.5418 Å, and a two-dimensional multiwire grid "Xe" gas detector. The exposure times varied from 10 to 20 seconds for the synchrotron experiments, to 60 minutes for the NanoSTAR experiments.

Data treatment was performed using the software FIT2D[27] and custom Matlab routines. The synchrotron data were normalized with respect to the transmitted intensity using a photodiode located inside the beam-stop and corrected with respect to the contribution from background scattering.

The instrumental peak broadening, used for peak fitting, was determined by measuring the 111 reflection from silicon powder.

2.3.2 Thermogravimetric analysis (TGA)

TGA was performed on a Netsch STA 449 F3 Jupiter TGA-DSC instrument under an argon atmosphere at a heating rate of 10 °C/min from 25 to 650 °C. Other instrumental parameters were adjusted with the software package STA 449F3. A 70 µL alumina crucible was used to hold the samples, which weighed 2-5 mg for the nanocomposites and pure PS, and 15-25 mg for the organoclays. The org-clays were pre-dried prior to measurements to eliminate the signal from absorbed atmospheric moisture.

2.3.3 Transmission electron microscopy (TEM)

TEM imaging of the PSLp and PSHT samples was performed using a JEOL JEM-2000FX transmission electron microscope operated at 200kV. Samples were prepared by placing microtome sections of the composite onto a holey carbon TEM grid.

3 RESULTS AND DISCUSSION

3.1 Analysis of organoclays

3.1.1 WAXS

In order to verify that the surface modification of the clays was successful, they were measured by WAXS prior to and after modification. The WAXS-curves shown in Figure 1 were used to calculate the average basal spacing between the silicate layers, $d_{001} = 2\pi/q_1$, where q_1 is the q-value at the center of the 001 Bragg-reflection. The basal spacings of the pristine clays were very similar in all cases, varying between 1.1 and 1.3 nm (see Figure 1e). The small variations can be due partly to minor differences in the amounts of intercalated water, since the pristine clays were stored and measured in ambient atmosphere.

On the other hand, there are significant differences in the peak widths (FWHM) of the 001 reflection peak, indicating limited size and/or strain of the silicate layer stacking, depending on the clay type. Pristine Fh presents a very sharp peak whereas the peak from pristine Lp is very broad. This is mainly attributed to the number of clay platelets in each tactoid, being larger in Fh (see also discussion in section 3.2.2). Strain is common in clays and arises due to a large variation in the stacking order of the clay tactoids.[28] Further discussions are presented later.

After surface modification, the d_{001}-spacing of the organoclays increases due to intercalation of CTAB-cations. The values are shown in Figure 1 and also listed in Table 2.

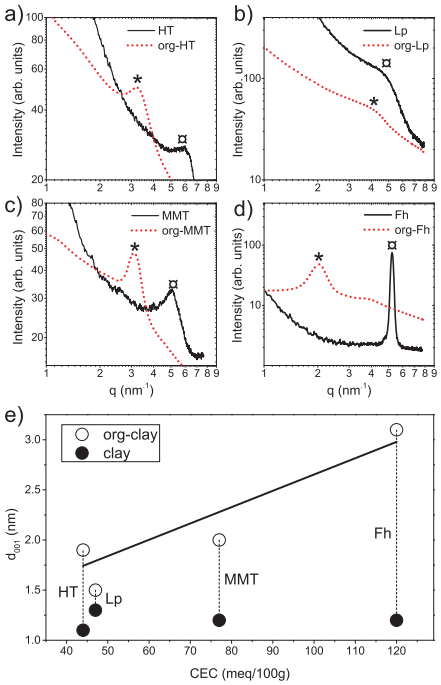

Figure 1 (a-d) WAXS-curves of pure clays and organoclays. The 001-reflection is indicated with (¤) and (*) for the pure clays and org-clays, respectively. Curves are scaled arbitrarily to facilitate comparison. (e) The d_{001}-spacing of the clays prior to and after surface modification. The solid line is a guide for the eye.

The spacing increases the most for org-Fh, reaching 3.1 nm, while org-MMT and org-HT obtain values of 2.0 and 1.9 nm, respectively. Interestingly, this swelling seems to be correlated with the magnitude of the surface charge of the three clays, e.g. Fh has the highest surface charge and hence intercalates more CTAB-cations. However, org-Lp distinguishes itself from the others, showing a very small increase in d_{001}-spacing, although the surface charge of Lp is comparable to HT (see Table 2). A possible cause is that the majority of org-Lp platelets are fully exfoliated when the Lp clay stacks expand above a certain threshold, and therefore do not contribute to the Bragg peak. A peak broadening for all four organically modified clays is also observed, which we interpret as either a reduced number of stacked clay platelets in each tactoid or a sign of uneven amounts of intercalated guest molecules from one clay gallery to another.

Table 2 Results from analyzing the organoclays with WAXS and TGA. The different steps of the mass loss are defined in Figure 2. d_{001} values for pure clays are added for comparison.

Clay type	CEC (meq/100g)	Pure clay d_{001}-spacing (nm)	org-clay d_{001}-spacing (nm)	Surfactant mass (%)	Rel. mass loss step 1 (%) (Adsorbed)	Rel. mass loss step 2-3 (%) (Intercalated)
HT	44	1.1	1.9	37	49	51
Lp	47	1.3	1.5	42	36	64
MMT	77	1.2	2.0	41	51	49
Fh	120	1.2	3.1	49	69	31

3.1.2 Thermogravimetric analysis org-clays

Thermogravimetric analysis (TGA) of the organoclays was performed to determine the quantity of surfactant molecules that was intercalated. The results, shown in Figure 2a, and listed in Table 2, indicate a correlation between the uptake of surfactant molecules and the CEC as well. Although CTAB was present in excess (4×CEC), the org-clays with larger surface charge (org-MMT and org-Fh) contained more surfactant, showing an almost linearly correlated increase (see Figure S2 in the supporting information).

Furthermore, the TGA-traces indicate that there are three major steps during decomposition of the surfactant.[29] The differentiated TGA-traces (DTGA), shown in Figure 2b, display two peaks above 200 °C for all organoclays. The peaks at around 300 °C are coupled to decomposition step 1 which is attributed to a high rate of decomposition of surfactant molecules *adsorbed* on the *outer* surface of the clay particle or tactoid. The peaks resulting from step 2 and step 3, above 375 °C, come from decomposition of *intercalated* surfactant molecules.[29] Moreover, we interpret the higher decomposition temperature for the intercalated molecules to be caused by the fact that they are a key part of the clay structure, serving as counterbalancing ions. Since the charge balance must stay intact, these molecules can only exit the clay galleries by degrading during several steps, forming H^+ ions.[15] The adsorbed molecules, on the other hand, may be loosely bound to the surface of the clay by Van der Waals interactions between nonpolar tail groups of CTAB. Furthermore the decomposition products of the intercalated molecules need to diffuse through an extended path along the gallery to exit. Org-Fh releases the intercalated molecules at a higher temperature than the other three organoclays (the peaks from step 2 and step 3 are shifted to higher temperatures). We believe the reason for this is that the higher surface charge of Fh shifts the equilibrium for degradation of CTAB to higher temperatures. On the other hand, the DTGA-peak at around 770 °C for org-Lp, marked with an asterisk (*), is due to dehydroxylation of the silicate structure.[29]

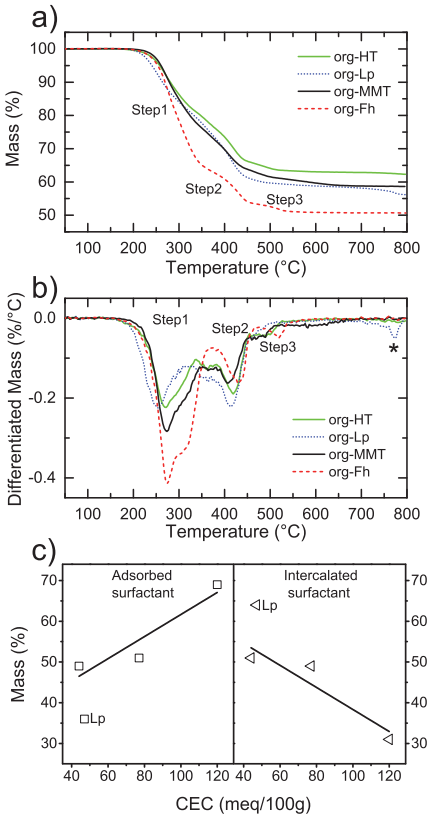

Figure 2 (a) TGA-traces of the four organoclays, (b) The corresponding DTGA-traces. (c) Mass fraction of adsorbed and intercalated surfactant as a function of CEC.

The relative mass losses during step 1 (adsorbed species), and subsequently during step 2-3 (intercalated species), are presented in Figure 2c and Table 2. From the figure, if org-Lp is not taken into account, it seems that the ratio of adsorbed and intercalated surfactant molecules is strongly

correlated with the amount of surface charge present in each clay. The reason why org-Lp shows a much higher value compared to org-HT, although the CEC is almost identical, may be explained by the better dispersion of Lp during the surface treatment, which increases the effective area for the surfactant to be attached.

3.2 Analysis of nanocomposites

3.2.1 WAXS: d-spacing

The WAXS-curves of the four different nanocomposites are shown in Figure 3. It is evident that the organoclays did not exfoliate completely during PS-polymerization because distinct peaks from 00*l* reflections are still present. The existence of higher order reflections indicates larger and more regular stacking domains in the nanocomposites compared to the organically modified clays alone.[30] Furthermore, the nanocomposites were semi-transparent when inspected in an optical microscope (see Figure S1 in the supporting information), which indicates that the stacked silicate layers form assemblies large enough to scatter visible light.

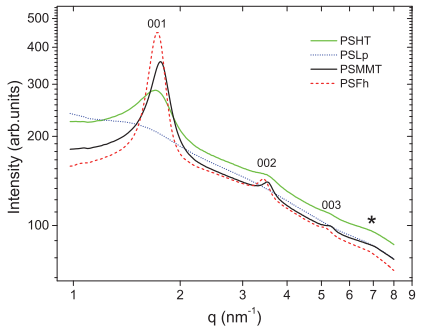

Figure 3 WAXS-curves of the four nanocomposites. 00*l*-reflections are labeled. The broad peak at the end of the diffractogram (labeled with *) originates from the amorphous halo of the PS matrix.

Figure 4 shows high-resolution TEM-micrographs of Laponite (a) and Hectorite (b) clay particles, respectively. The Laponite platelets are well dispersed in the matrix and no large aggregates are observed. Hectorite, on the other hand, displays small 15-20 nm thick tactoids arranged into larger agglomerates. These results are in good agreement with the WAXS results discussed later.

All four nanocomposite samples show a larger d_{001}-spacing compared to pure organoclays (see Table 2 and Table 3 later) due to intercalation of PS chains between the silicate layers, and it seems that they reach a common value between 3.6 and 4.0 nm. Similar basal spacings in PS-clay nanocomposites have been reported earlier,[10,17,31,32] indicating that the present values produce the optimum space for a compact arrangement of PS chains between silicate sheets.

3.2.2 WAXS: particle/tactoid size

The Bragg peaks of the nanocomposites in Figure 3 are broadened beyond the instrumental resolution. The additional contribution from the sample to the peak widths may be obtained by describing each peak by a pseudo-Voigt function, which has two components. One Gaussian component, which counts for the instrumental peak width, and one Lorentzian which counts for the broadening due to size/strain effects. A more detailed explanation of the peak fitting procedure is given in the supporting information. The average number of platelets in each tactoid was calculated from the particle/tactoid size which was found using both

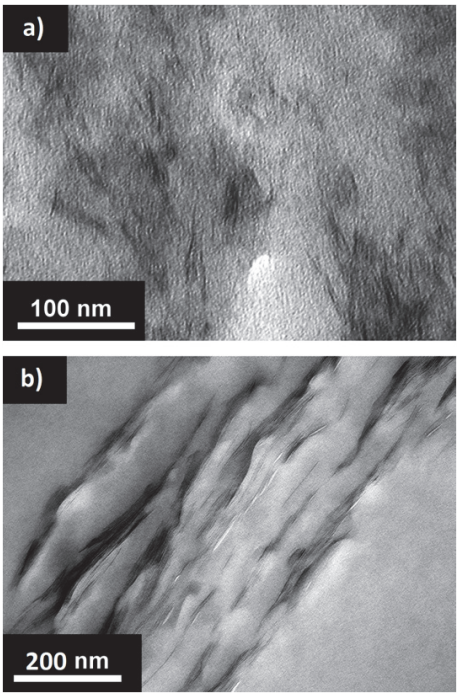

Figure 4 High-resolution TEM micrographs of clay in two nanocomposites. (a) shows well-dispersed Laponite platelets in the PSLp sample, while (b) shows larger stacking structures of Hectorite platelets in the PSHT sample.

Table 3 Average basal spacing in the nanocomposites and the number of platelets, *N*, in the tactoids. The standard deviation in *N* is ± 1.

Clay type	d_{001}-spacing in nano-composite (nm)	Number of platelets (N)		
		organoclay	Nanocomposites	
		Scherrer	Scherrer	Williamson -Hall
HT	3.7	7	7	4
Lp	4.0	6	4	-
MMT	3.6	9	15	13
Fh	3.7	8	19	121

the Scherrer equation,[33] and a Williamson-Hall analysis.[34] The results for both organoclays and nanocomposites are given in Table 3.

Comparing the values of *N* for the nanocomposites it is clear that the Scherrer equation underestimates the strain broadening and may lead to apparently larger particle sizes. This is particularly true for PSFh where there is a large discrepancy between the two methods, which originates from the higher strain in this sample compared to PSMMT and PSHT (PSFh shows a steeper slope in Figure S3 in the supplementary information). Except for PSFh, however, the variation of *N* between the two methods is close to the level of uncertainty, and hence we can assume the values obtained for the organoclays, where only the Scherrer equation could be used, to be valid. Moreover, Uthirakumar et al.[35] prepared PSMMT samples which contained 10-20 nm thick MMT-tactoids (with *N*~6), a value close to ours. The reason why PSFh displays such a large strain is not obvious, but it may originate from the volume contraction of around 10 % when styrene polymerizes. The large size of the Fh-tactoids can make it difficult to release the stress induced by the shrinking matrix. Another cause may be that org-Fh originally has more disorder in the stacking due to uneven charge distribution between layers.[13]

Again it was observed that the surface charge of the clays influences the nanocomposites to a high degree, holding the silicate layers together and increasing the number of platelets in each stack as the surface charge increases. On the other hand, the *N* values for the four different organoclays in powdered form (no polymer present) are quite similar. A possible reason for this, and also why their tactoids are quite small compared to pure clays, is that the organoclays crystallize nearly instantaneously from single platelets in suspension during the surface treatment. As a comparison, the nominal value for unmodified Na-Fh is between 75 and 100 platelets in each tactoid.[30]

The increase in *N* in nanocomposites compared to organoclay samples for the Fh- and MMT-systems indicates that the organoclays dissolve to some degree in the styrene monomer, before assembling into larger tactoids. *In situ* WAXS of styrene-clay dispersions showed that when org-Lp was dispersed at room temperature, the d_{001}-spacing increased from 1.5 nm in powdered form up to 7.1 nm when dispersed, while org-Fh increased from 3.1 up to 4.7 nm. Continuous heating up to 100 °C induced a minor additional increase in d-spacing (see Figure 5). The swelled structures and particularly the large increase displayed by org-Lp may help dispersing the clay tactoids through exfoliation. This study also suggests that a low to moderate surface charge could lower the barrier for exfoliation by allowing large d-spacings during polymerization.

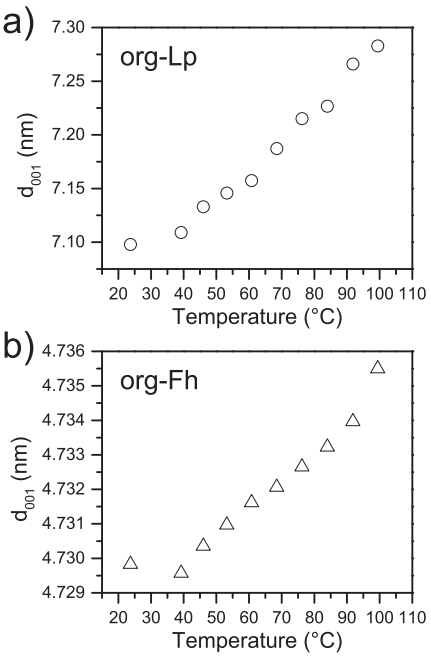

Figure 5 d_{001}-spacing of org-Lp and org-Fh dispersed in styrene as a function of temperature.

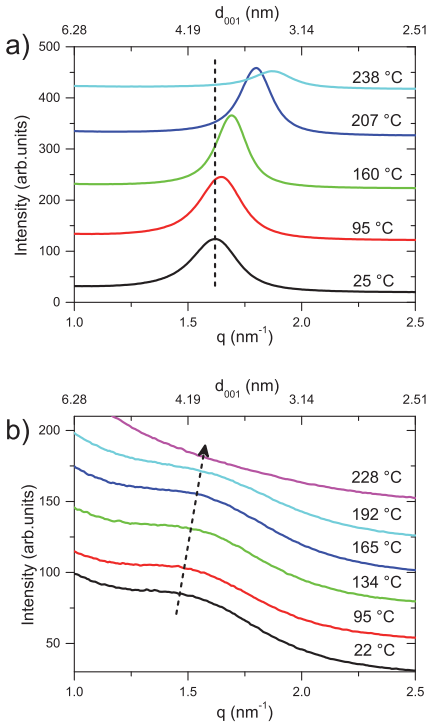

Figure 6 WAXS-curves around the 001-reflection of PSFh (a) and PSLp (b) nanocomposites during heating. Temperatures are indicated next to each curve, and the curves are shifted along the y-axis to make the changes more visible.

In situ heating WAXS-studies up to 250 °C, of PSFh and PSLp, presented in Figure 6, showed noticeable changes in both nanocomposites. The d_{001}-spacing of PSFh (Figure 6a) shrinks during heating because intercalated PS chains are slowly dissolved in the surrounding matrix. The spacing converges towards the value of the organoclay of 3.1 nm, before the sample melts completely. In the melted state the clay structure collapses further due to the release of the remaining PS chains and intercalated surfactant molecules. The spacing of PSLp (Figure 6b), on the other hand, decreases only slightly from 4.1 to 3.9 nm before the 001-reflection disappears completely, indicating full exfoliation of the clay tactoids. Scanning several points in the heat-treated part of the sample after cooling did not reveal any Bragg reflection, meaning that the clay remained mostly exfoliated. This result seems to point out that low-CEC nanocomposites through *in situ* polymerization, and post heating up to 250 °C, may produce well exfoliated clay structures. These findings again suggest a correlation between the surface charge of the clays and the behavior of their respective nanocomposites, showing exfoliation to a higher degree for clay tactoids carrying lower surface charge.

3.2.3 Thermal behavior

Figure 7a shows TGA-traces from decomposition of the four different nanocomposites together with a curve of pure PS. All samples have a small mass loss between 200-375 °C, in contrast to the pure polymer which is stable in this temperature range. This loss is most likely due to small amounts of unreacted monomer and surfactant molecules in the composites. The lowest point of the DTGA curves shows the temperature at maximum decomposition rate, and the average of several values for each sample is listed in the inset of Figure 7b. With as little as 3.2 wt.% of inorganic filler

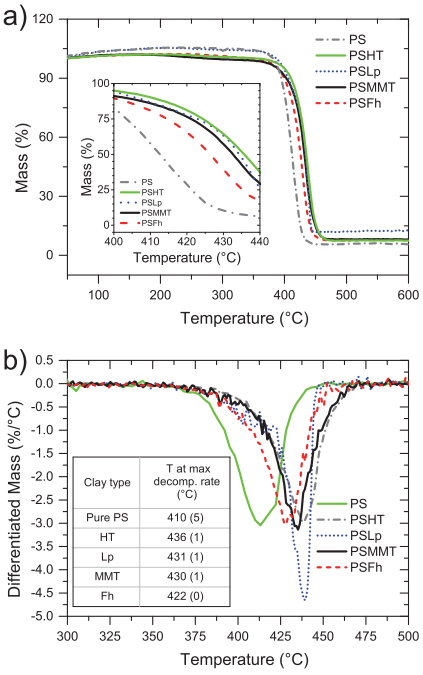

Figure 7 (a) TGA-traces of pure PS and PS-clay nanocomposites. Inset shows a zoomed-in view of the steep drop between 400 and 440 °C. (b) The corresponding DTGA-traces. The inset shows a table with the average decomposition temperatures at maximum decomposition rate. 3σ standard deviation is given in parenthesis.

added, the decomposition temperature is increased for all four nanocomposites. The largest improvement compared to pure PS is seen for the natural HT-clay with a 26 °C higher temperature at maximum decomposition rate. The synthetic Lp-clay and the natural MMT-clay have similar improvements with 21 and 20 °C respectively, which are comparable to MMT-clay values of PSMMT given in a report by Gilman et al.[36] The smallest improvement (12 °C) is found in the synthetic Fluorohectorite clay (Fh), as Gilman et al. also identified when comparing the flame retardant properties of PSMMT and PSFh nanocomposites.[1] This trend also follows the differences in surface charge between the four clays, showing higher decomposition temperatures for the lower CEC values.

The higher degradation temperature of polymer-clay nanocomposites compared to pure polymers is related to the superior insulator and mass transport barrier for the volatile products generated during decomposition. A more tortuous path inside the nanocomposites is beneficial for the thermal stability of the material. Based on the models by Bharadadwaj,[37] the tortuosity is increased when well dispersed and large aspect ratio platelets are present in the system, whereas a large stacking number or aggregations produce the opposite effect. This model explains qualitatively our results, dependent on the clay type. Lp-platelets have lower surface charge and a better dispersed morphology, but their aspect ratio is lower than for MMT-platelets. A similar degradation temperature is then obtained. Fh-platelets are larger than the other clays but their surface charge is too high to promote exfoliation and present larger stacking structures. HT-platelets, on the other hand, have both larger area than Lp and a slightly lower surface charge which facilitates exfoliation. These factors turn HT into a better candidate than the other three clays as filler for improving the high-temperature resilience of PS based nanocomposites.

4 CONCLUSIONS

In this work a series of polystyrene-organoclay nanocomposites with different clay surface charge were prepared via in-situ polymerization. Their structure and thermal properties were explored using various experimental techniques. WAXS measurements showed that the resulting nanocomposites were in all cases a mix of intercalated and exfoliated silicate layers. However, PSLp presented a good dispersion of the platelets, and this was further improved after thermal treatment up to 250 °C.

The intrinsic surface charge of the clays was found to play an important role in the uptake of surfactant molecules and in the dispersion of clay platelets in the PS matrix. A larger surface charge facilitated enhanced intercalation of CTAB, as well as showing an almost linear increase in the number of platelets in each tactoid in both organoclays and nanocomposites. A lower surface charge allowed for increased dispersions for Hectorite and Laponite clay, compared to Montmorillonite and Fluorohectorite, which ultimately resulted in better thermal properties for the former two.

ASSOCIATED CONTENT

Supporting Information

Picture of the polymerized nanocomposites (Fig. S1). Mass fraction of surfactant in org-clays (Fig. S2). Detailed procedure for performing peak analysis of WAXS data, including fittings of the 00*l* peaks (Fig. S3) and peak widths (Fig S4), as a function of *q*. This material is available free of charge via the Internet at http://pubs.acs.org.

ACKNOWLEDGEMENTS

This work was performed under the sponsorship of The Research Council of Norway. The authors thank Fredrik S. Hage and Antje Hoenen for the assistance in the TEM analysis. The beam time provided by MAX-Lab is also acknowledged. The contribution from the referees to clarify the work is greatly appreciated.

AUTHOR INFORMATION

Corresponding author

*E-mail: kenneth.knudsen@ife.no; henrik.mauroy@ife.no

REFERENCES

(1) Gilman, J. W.; Jackson, C. L.; Morgan, A. B.; Harris, R.; Manias, E.; Giannelis, E. P.; Wuthenow, M.; Hilton, D.; Phillips, S. H. Flammability Properties of Polymer - Layered-Silicate Nanocomposites. Polypropylene and Polystyrene Nanocomposites. *Chem. Mater.* **2000**, 12, 1866-1873.

(2) Zhu, J.; Wilkie, C. A. Thermal and Fire Studies on Polystyrene-Clay Nanocomposites. *Polym. Int.* **2000**, 49, 1158-1163.

(3) Kojima, Y.; Usuki, A.; Kawasumi, M.; Okada, A.; Fukushima, Y.; Kurauchi, T.; Kamigaito, O. Mechanical Properties of Nylon 6-Clay Hybrid. *J. Mater. Res.* **1993**, 8, 1185-1189.

(4) He, J.; Shen, Y.; Evans, D. G. A Nanocomposite Structure Based on Modified Mcm-48 and Polystyrene. *Microporous Mesoporous Mater.* **2008**, 109, 73-83.

(5) Haraguchi, K.; Takehisa, T. Nanocomposite Hydrogels: A Unique Organic-Inorganic Network Structure with Extraordinary Mechanical, Optical, and Swelling/De-Swelling Properties. *Adv. Mater.* **2002**, 14, 1120-1124.

(6) Utracki, L. A. *Clay-Containing Polymeric Nanocomposites*; Smithers Rapra Technology: Shrewsbury, U.K., 2004.
(7) Usuki, A.; Kojima, Y.; Kawasumi, M.; Okada, A.; Fukushima, Y.; Kurauchi, T.; Kamigaito, O. Synthesis of Nylon 6-Clay Hybrid. *J. Mater. Res.* **1993**, 8, 1179-1184.
(8) Okada, A.; Usuki, A. Twenty Years of Polymer-Clay Nanocomposites. *Macromol. Mater. Eng.* **2006**, 291, 1449-1476.
(9) Hasegawa, N.; Kawasumi, M.; Kato, M.; Usuki, A.; Okada, A. Preparation and Mechanical Properties of Polypropylene-Clay Hybrids Using a Maleic Anhydride-Modified Polypropylene Oligomer. *J. Appl. Polym. Sci.* **1998**, 67, 87-92.
(10) Hasegawa, N.; Okamoto, H.; Kawasumi, M.; Usuki, A. Preparation and Mechanical Properties of Polystyrene-Clay Hybrids. *J. Appl. Polym. Sci.* **1999**, 74, 3359-3364.
(11) Panwar, A.; Choudhary, V.; Sharma, D. K. A Review: Polystyrene/Clay Nanocomposites. *J. Reinf. Plast. Compos.* **2011**, 30, 446-459.
(12) Vaia, R. A.; Ishii, H.; Giannelis, E. P. Synthesis and Properties of 2-Dimensional Nanostructures by Direct Intercalation of Polymer Melts in Layered Silicates. *Chem. Mater.* **1993**, 5, 1694-1696.
(13) Alexandre, M.; Dubois, P. Polymer-Layered Silicate Nanocomposites: Preparation, Properties and Uses of a New Class of Materials. *Mater. Sci. Eng., R* **2000**, 28, 1-63.
(14) Fu, X.; Qutubuddin, S. Synthesis of Polystyrene-Clay Nanocomposites. *Mater. Lett.* **2000**, 42, 12-15.
(15) Zhu, J.; Morgan, A. B.; Lamelas, F. J.; Wilkie, C. A. Fire Properties of Polystyrene-Clay Nanocomposites. *Chem. Mater.* **2001**, 13, 3774-3780.
(16) Kaviratna, P. D.; Pinnavaia, T. J.; Schroeder, P. A. Dielectric Properties of Smectite Clays. *J. Phys. Chem. Solids* **1996**, 57, 1897-1906.
(17) Mitchell, C. A.; Krishnamoorti, R. Rheological Properties of Diblock Copolymer/Layered Silicate Nanocomposites. *J. Polym. Sci., Part B: Polym. Phys.* **2002**, 40, 1434-1443.
(18) Burmistr, M. V.; Sukhyy, K. M.; Shilov, V. V.; Pissis, P.; Spanoudaki, A.; Sukha, I. V.; Tomilo, V. I.; Gomza, Y. P. Synthesis, Structure, Thermal and Mechanical Properties of Nanocomposites Based on Linear Polymers and Layered Silicates Modified by Polymeric Quaternary Ammonium Salts (Ionenes). *Polymer* **2005**, 46, 12226-12232.
(19) Sun, Q. H.; Deng, Y. L.; Wang, Z. L. Synthesis and Characterization of Polystyrene-Encapsulated Laponite Composites Via Miniemulsion Polymerization. *Macromol. Mater. Eng.* **2004**, 289, 288-295.
(20) Zhu, J.; Uhl, F. M.; Morgan, A. B.; Wilkie, C. A. Studies on the Mechanism by Which the Formation of Nanocomposites Enhances Thermal Stability. *Chem. Mater.* **2001**, 13, 4649-4654.
(21) The Clay Minerals Society. Source Clay Physical/Chemical Data. http://www.clays.org/SOURCE%20CLAYS/SCdata.html Apr. 04 DateAccess. 2013
(22) Bakk, A.; Fossum, J. O.; da Silva, G. J.; Adland, H. M.; Mikkelsen, A.; Elgsaeter, A. Viscosity and Transient Electric Birefringence Study of Clay Colloidal Aggregation. *Phys. Rev. E* **2002**, 65, 9.
(23) Chen, B. Q.; Evans, J. R. G. Thermoplastic Starch-Clay Nanocomposites and Their Characteristics. *Carbohydr. Polym.* **2005**, 61, 455-463.
(24) Moncada, E.; Quijada, R.; Lieberwirth, I.; Yazdani-Pedram, M. Use of Pp Grafted with Itaconic Acid as a New Compatibilizer for Pp/Clay Nanocomposites. *Macromol. Chem. Phys.* **2006**, 207, 1376-1386.
(25) Boylu, F.; Hojiyev, R.; Ersever, G.; Ulcay, Y.; Celik, M. S. Production of Ultrapure Bentonite Clays through Centrifugation Techniques. *Sep. Sci. Technol.* **2012**, 47, 842-849.
(26) Labrador, A. L.; Cerenius, Y.; Svensson, S.; Theodor, K.; Plivelic, T. S. The Yellow Mini-Hutch for Saxs Experiments at Max Iv Laboratory. *J. Phys.: Conf. Ser.* **2013**, 425, 072019.
(27) Hammersley, A. P.; Svensson, S. O.; Hanfland, M.; Fitch, A. N.; Hausermann, D. Two-Dimensional Detector Software: From Real Detector to Idealised Image or Two-Theta Scan. *High Pressure Res.* **1996**, 14, 235-248.
(28) Laird, D. A. Influence of Layer Charge on Swelling of Smectites. *Appl. Clay Sci.* **2006**, 34, 74-87.
(29) Wang, B. X.; Zhou, M.; Rozynek, Z.; Fossum, J. O. Electrorheological Properties of Organically Modified Nanolayered Laponite: Influence of Intercalation, Adsorption and Wettability. *J. Mater. Chem.* **2009**, 19, 1816-1828.
(30) da Silva, G. J.; Fossum, J. O.; DiMasi, E.; Maloy, K. J.; Lutnaes, S. B. Synchrotron X-Ray Scattering Studies of Water Intercalation in a Layered Synthetic Silicate. *Phys. Rev. E* **2002**, 66.
(31) Arora, A.; Choudhary, V.; Sharma, D. K. Effect of Clay Content and Clay/Surfactant on the Mechanical, Thermal and Barrier Properties of Polystyrene/Organoclay Nanocomposites. *Journal of Polymer Research* **2011**, 18, 843-857.
(32) Qi, R.; Jin, X.; Huang, S. Synthesis and Characteristics of Polystyrene-Clay Nanocomposites Via in Situ Intercalative Polymerization in a Direct Current Electric Field. *J. Appl. Polym. Sci.* **2010**, 115, 2723-2727.
(33) Patterson, A. L. The Scherrer Formula for X-Ray Particle Size Determination. *Physical Review* **1939**, 56, 978-982.
(34) Williamson, G. K.; Hall, W. H. X-Ray Line Broadening from Filed Aluminium and Wolfram. *Acta Metall.* **1953**, 1, 22-31.

(35) Uthirakumar, P.; Nahm, K. S.; Hahn, Y. B.; Lee, Y. S. Preparation of Polystyrene/Montmorillonite Nanocomposites Using a New Radical Initiator-Montmorillonite Hybrid Via in Situ Intercalative Polymerization. *Eur. Polym. J.* **2004**, 40, 2437-2444.
(36) Gilman, J. W.; Kashiwagi, T.; Morgan, A. B.; Harris, R.; Brassell, L.; Vanlandingham, M.; Jackson, C. L. *Flammability of Polymer Clay Nanocomposites Consortium: Year One Annual Report*, US Dept. Commerce, Technology Administration, National Institute of Standards and Technology, 2000.
(37) Bharadwaj, R. K. Modeling the Barrier Properties of Polymer-Layered Silicate Nanocomposites. *Macromolecules* **2001**, 34, 9189-9192.

The effect of clay surface charge on the emerging properties of Polystyrene-organoclay nanocomposites

Henrik Mauroy[a,b], Tomás S. Plivelic[c] ,Elisabeth L. Hansen[d], Jon Otto Fossum[d], Geir Helgesen[a,b] and Kenneth D. Knudsen*[a,d]*

[a]Physics department, Institute for Energy Technology, P.O. Box 40, N-2027 Kjeller, Norway

[b]Department of Physics, University of Oslo, N-0316 Oslo, Norway

[c]MAX IV Laboratory, Lund University, P.O. Box 118, SE-221 00 Lund, Sweden

[d]Department of Physics, Norwegian University of Science and Technology, Hoegskoleringen 5, N-7491 Trondheim, Norway

*E-mail: Kenneth D. Knudsen: kenneth.knudsen@ife.no; Henrik Mauroy: henrik.mauroy@ife.no

Supporting information

1 Picture of the finished nanocomposites

The polymerized nanocomposites are displayed in Figure S1 together with a pure polystyrene (PS) sample. All samples, except PS-Fluorohectorite (Fh) were semitransparent.

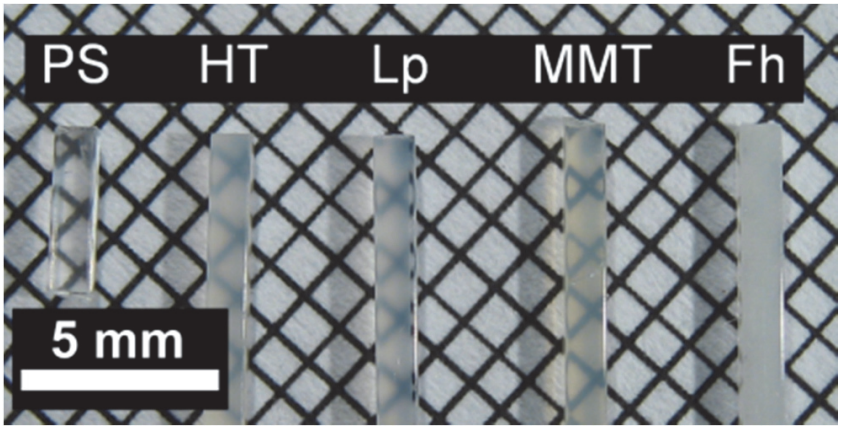

Figure S1. Picture of the finished nanocomposites. From left: pure PS, PS-Hectorite (HT), PS-Laponite (Lp), PS-Montmorillonite (MMT) and PS-Fluorohectorite (Fh).

2 Mass fraction of surfactant in org-clays

The total amount of surfactant intercalated and adsorbed by the clays during surface treatment was determined with thermogravimetric analysis (TGA). The results indicated an almost linear correlation between clay surface charge and the total uptake of surfactant as is shown in Figure S2.

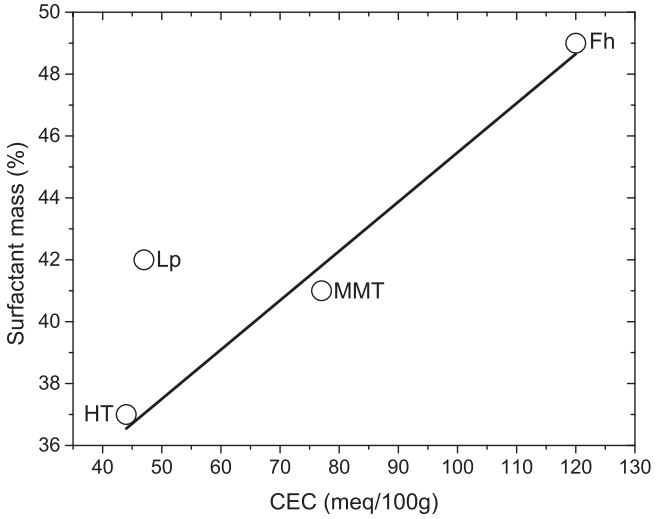

Figure S2. Mass fraction of surfactant in org-clays as a function of CEC.

3 Peak fitting of x-ray data

3.1 Introduction

A detailed description of the determination of the thickness of the clay tactoids in the nanocomposites is presented below. The 00*l* reflections for both the organoclays and organoclays inside the nanocomposites are broadened beyond the instrumental resolution. The additional contribution from the sample to the peak widths can be obtained by deconvoluting the scattered intensity $I(q)=C(q)\Phi(q)$. The C parameter is related to the scattering setup and polarization factors, and can be approximated by a constant value in the region around each 00*l* peak since it varies slowly with q compared to the peak widths.[1] After subtracting a polynomial function for the background contribution around each peak, and normalizing the intensity to 1, the 00*l* reflections for the organoclays and the nanocomposites were fitted with a pseudo-Voigt function

$$\Phi(q) = \frac{2\eta}{\pi\Gamma(1+4(q-q_c)^2/\Gamma^2)} + 2\frac{1-\eta}{\Gamma}\left(\frac{ln2}{\pi}\right)^{1/2} e^{-4ln2(q-q_c)^2/\Gamma^2} \quad (1)$$

that approximates the peak profile as a linear combination of a Gaussian and a Lorentzian component.[2] q_c is the refined center of the peak, Γ is the measured width at half maximum (FWHM) and η is a mixing parameter between zero and one that determines the extent of the Lorentzian contribution. Γ and η can be expressed as a function of the Gaussian, Γ_G, and Lorentzian, Γ_L, width contribution, which are directly connected to Γ and η with two polynomial expressions[2],

$$\Gamma = \Gamma_G^5 + 2.6927\Gamma_G^4\Gamma_L + 2.4284\Gamma_G^3\Gamma_L^2 + 4.471\Gamma_G^2\Gamma_L^3 + 0.0784\Gamma_G\Gamma_L^4 + \Gamma_L^5 \quad (2)$$

$$\eta = 1.36603\frac{\Gamma_L}{\Gamma} - 0.47719\frac{\Gamma_L^2}{\Gamma^2} + 0.11116\frac{\Gamma_L^3}{\Gamma^3} \quad (3)$$

In order to determine the instrumental peak broadening, the 111 reflection from a silicon powder standard was fitted with eq. 1. Normally the instrumental broadening is attributed to the Gaussian component alone. However, we here allow also for a minor contribution from a Lorentzian component. The fit resulted in Γ_G = 0.09663 nm^{-1} and Γ_L = 0.03967 nm^{-1}. Γ_G = 0.09663 nm^{-1} was thus set as a locked parameter in eq. 1 in the later fitting procedure, and only Γ_L and q_c were refined. The instrumental contribution to Γ_L was later subtracted from the

sample's Γ_L. Figure S3 shows the results of the fitting for some of the samples, and also examples of the Gaussian and Lorentzian contributions.

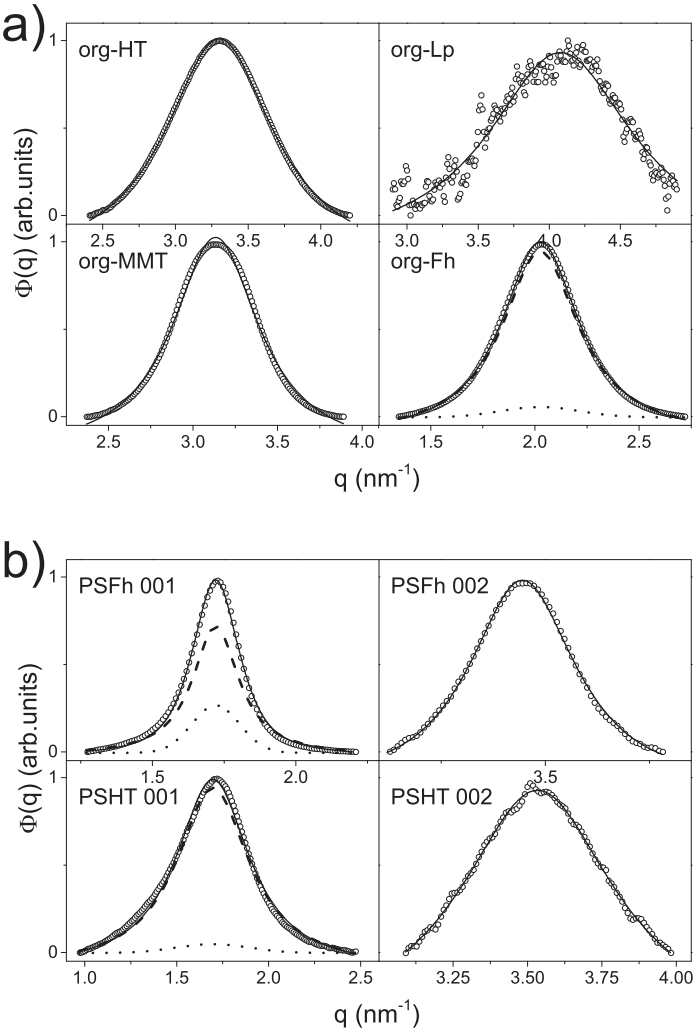

Figure S3. Peak fitting of the a) organoclays and b) the 001 and 002 reflections from PSFh and PSHT. The open symbols are the experimental data, and the continuous lines are the fits. The

dotted and dashed lines in the panel for org-Fh and the panels for the 001 peaks show the Gaussian and Lorentzian contributions, respectively.

3.2 Williamson-Hall analysis

The Lorentzian component of the FWHM is connected with the effect of both the particle size and strain on the silicate layer stacking.[3] The average thickness of each clay tactoid, and thus the number of platelets they contain, can therefore be determined from a Williamson-Hall[3] plot according to the following relations:[1]

$$\Gamma_L = \frac{2\pi}{Nd} + \xi q \qquad (4)$$

where N is the number of platelets in a clay stack, d is the d_{00l}-spacing and ξ is the strain. The slope of the straight line gives the strain and its intercept at $q = 0$ estimates the thickness.

Figure S4 shows the plots of the widths Γ_L versus peak positions for PSFh, PSMMT and PSHT. The calculated values for N and the strain ξ are shown as insets. PSLp could not be analyzed with this method because it did not show any higher order reflections. An absence of higher order reflections was also the case for the organoclay-powders, except org-Fh which showed a weak 002 reflection.

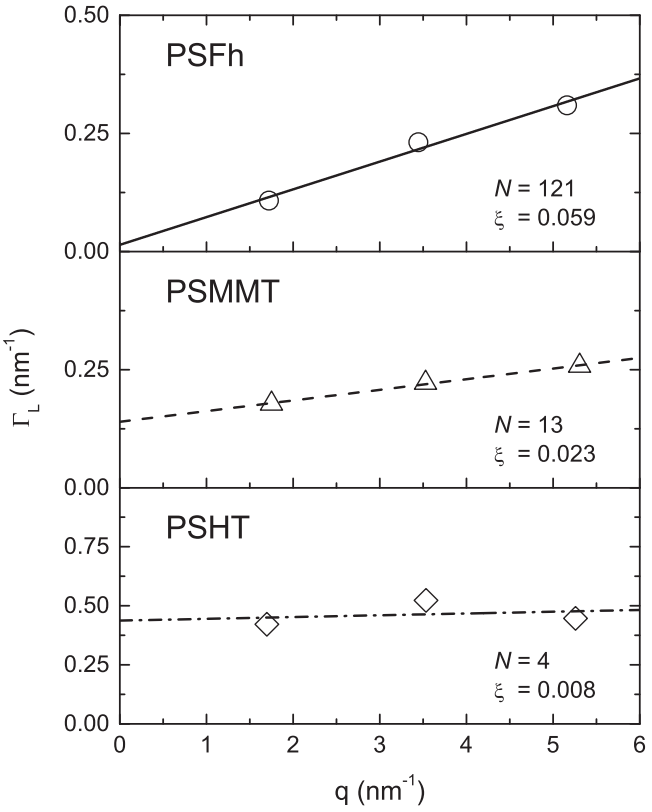

Figure S4. Williamson-Hall plot for PSFh, PSMMT and PSHT. The straight lines are fitted to the function in eq. 4, and the calculated values for N and the strain ξ are shown as insets.

3.3 Scherrer equation

Another method to estimate the average number of platelets in the tactoids is the Scherrer equation:[4]

$$Nd = \frac{K \cdot \lambda}{\Delta\theta_L \cdot cos\theta} \quad (3)$$

where d is the d_{001}-spacing, K (~0.9) is a numerical constant, $\Delta\theta_L$ is the Lorentzian component of the FWHM measured in radians and 2θ the Bragg angle. The average number of platelets in each tactoid for both the organoclay-powders and the nanocomposites, based on eq. (2) and (3), are presented in Table 3 of the manuscript.

4 References

(1) da Silva, G. J.; Fossum, J. O.; DiMasi, E.; Maloy, K. J.; Lutnaes, S. B. Synchrotron X-Ray Scattering Studies of Water Intercalation in a Layered Synthetic Silicate. *Phys. Rev. E* **2002**, 66.

(2) Thompson, P.; Cox, D. E.; Hastings, J. B. Rietveld Refinement of Debye-Scherrer Synchrotron X-Ray Data from Al2o3. *J. Appl. Crystallogr.* **1987**, 20, 79-83.

(3) Williamson, G. K.; Hall, W. H. X-Ray Line Broadening from Filed Aluminium and Wolfram. *Acta Metall.* **1953**, 1, 22-31.

(4) Patterson, A. L. The Scherrer Formula for X-Ray Particle Size Determination. *Physical Review* **1939**, 56, 978-982.

III

Manuscript in preparation

Anisotropic polystyrene-clay nanocomposites: Synthesis, characterization and mechanical properties

Henrik Mauroy*[a,b], Tomás S. Plivelic[c], Jussi-Petteri Suuronen[d], Jon Otto Fossum[e], Geir Helgesen[a,b] and Kenneth D. Knudsen*[a,e]

[a]Physics department, Institute for Energy Technology, P.O. Box 40, N-2027 Kjeller, Norway
[b]Department of Physics, University of Oslo, N-0316 Oslo, Norway
[c]MAX IV Laboratory, Lund University, P.O. Box 118, SE-221 00 Lund, Sweden
[d]Department of Physics, Division of Materials Physics, University of Helsinki, P.O.Box 64, FI-00014, Finland
[e]Department of Physics, Norwegian University of Science and Technology, Hoegskoleringen 5, N-7491 Trondheim, Norway

ABSTRACT: Recent studies on polymer-clay nanocomposites have shown prominent improvements in thermal and mechanical properties with the addition of quite small amounts of nanometer sized clay particles. In the present work we have characterized anisotropic polystyrene-clay nanocomposites synthesized utilizing a guided self-assembly technique, which aligned the clay particles into chain-like structures inside the polymer matrix. Four different kinds of surface modified clay were used as reinforcing agents, namely Hectorite, Laponite, Na-Montmorillonite and Li-Fluorohectorite. The microstructure of the nanocomposites was examined with wide angle x-ray scattering (WAXS) and x-ray computed microtomography (XMT). Thermogravimetric analysis (TGA) was further used to examine the high-temperature resilience of the nanocomposites before the mechanical properties during compression were determined. The results indicated that the nanocomposites were of the intercalated type with the clay dispersed as ~15-70 nanometer sized tactoids. Our earlier studies have shown that the degree of dispersion of the clay, as well as the resulting thermal and mechanical properties of the nanocomposites, are systematically and almost linearly correlated with the intrinsic surface charge of the clays.[1] The structural anisotropy on the other hand induced measurable differences in two of the samples containing Laponite. These samples displayed higher yield strength when compressed in a direction parallel to the clay chains compared to when compression was in the perpendicular direction.

1 INTRODUCTION

Anisotropy in the mechanical properties is a desired quality of modern polymeric composite materials where high strength along a particular direction is desired. This can be in e.g. light bicycle frames,[2] automotive car suspensions,[3] cross bows,[4] or even in large aircraft like the new Boeing 787.[5,6] These materials are made of sheets of woven or braided high-strength fibers (e.g. glass, carbon or polyaramides) embedded in a polymer matrix. The fabrication of today's state-of-the-art polymer composites are still using macroscopic fibers with thickness in the millimeter range and lengths measured in centimeters or meters. To enhance these materials further one need better control of the structure of the reinforcing fibers on the micro and nano scale.

We have investigated a concept which circumvents the conventional top-down approach by utilizing a guided self-assembly technique to orient the reinforcing filler particles, in this case clay nanoparticles, in an anisotropic pattern inside the polymer matrix. Polymer-clay nanocomposites (PCN) have earlier showed large improvements in the physical properties at surprisingly low weight fractions.[7,8] This is due to the large aspect ratio of clay platelets and their large surface area.[9,10] These interesting properties, combined with anisotropy, are likely to result in new types of materials with highly specialized properties. The clay platelets may for instance be chemically bonded together after the alignment process to increase the tensile strength, or be cross-linked to also improve the overall rigidity. The present work investigates the synthesis and characterization of a simple version of the proposed system where clay particles are aligned into chains, but not linked together, inside a polystyrene matrix.

The guided self-assembly is performed by applying an alternating electric field to the monomer-clay dispersion to manipulate the orientation of the clay particles. The clay is electrically polarized along the silica sheets inside the electric

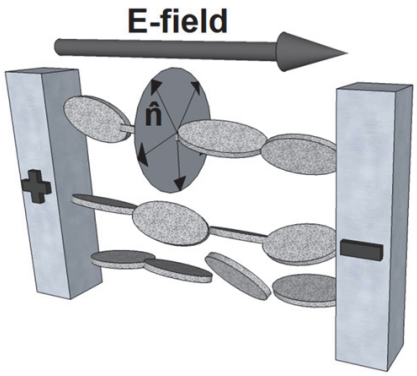

Figure 1 Sketch of how the clay particles align inside an electric field.

field,[11,12] i.e. the plate normal, $\hat{\boldsymbol{n}}$, is perpendicular to the direction of the electric field (see Figure 1).

This results in chain formation by the clay particles due to attractive forces between positively and negatively charged parts. An effective polarization of the clay occurs when the dielectric constant of the matrix is lower than for the clay.[13] In this work the dielectric constant of styrene was measured to be approximately 1.7 which is a little lower than the values of approximately 3.5-9 that we measured for the clays used in this work.

In the presented work four different types of clay were used separately in each nanocomposite. Two batches of samples, one with alignment under E-field and one without, were prepared in parallel, and examined by wide angle x-ray scattering (WAXS), x-ray computed microtomography (XMT) and thermogravimetric analysis (TGA). The mechanical properties of the nanocomposites were measured and the impact of the morphology is discussed.

2 EXPERIMENTAL

2.1 Materials

Styrene monomer (≥99%) and Benzoyl peroxide (Luperox® A75, 25 % water) were purchased from Sigma-Aldrich and used without further purification. The synthetic clay, Laponite XLG (Lp) was kindly donated by Andreas Jennow AB (Lp), and the synthetic clay Li-Fluorohectorite (Fh), was purchased from Corning Inc. Two natural clays, Na-Montmorillonite SWy-2 (MMT) and Hectorite SHCa-1 (HT), were purchased from The Clay Minerals Society Repository. The cation exchange capacities (CEC) of the clays used here are given in Table 1.

2.2 Preparation/synthesis

The clays were surface modified using cetyltrimethylammonium bromide (CTAB) through a simple cation-exchange process, where the ammonium cation of CTAB replaces the inorganic cations between the clay platelets. A detailed description can be found in ref. [1]. The four clays were labeled org-X, where X is the type of clay, i.e. org-HT for the surface treated Hectorite clay etc. Table 1 lists the basal spacing (d_{001}) before and after surface modification, and the weight fraction of surfactant.

Polystyrene-clay nanocomposites with two different clay concentrations, 1 and 3 wt.%, were prepared with *in situ* free radical polymerization of PS inside sealed square-shaped glass capillaries, with inner dimensions of 1.0 mm. A more detailed description can be found in ref. [1]. The capillaries were immersed in silicone oil kept at 95 °C to polymerize for 5 days standing upright. A parallel batch of nanocomposites with aligned clay particles was also prepared. These samples were placed between two parallel flat electrodes, immersed in the silicone oil, oriented with their glass walls parallel to the electrodes. An alternating voltage was applied over the electrodes producing an electric field (E-field) of 625 V/mm, which was the maximum field achievable with the present setup. The polymerized nanocomposites, now shaped as square rods, were carefully pulled out of the capillaries and

Table 1 Selected properties for the clays and organoclays.

Clay type†	CEC (meq/100g)‡	Pure clay d_{001}-spacing[1] (nm)	org-clay d_{001}-spacing[1] (nm)	Weight fraction of surfactant in the organoclay[1] (%)
HT	43.9	1.1	1.9	35
Lp	47	1.3	1.5	36
MMT	76.4	1.2	2.0	36
FH	120	1.2	3.1	40

† HT = Hectorite, Lp = Laponite, MMT = Montmorillonite and Fh = Fluorohectorite

‡ HT, MMT see ref [14]., Lp, Fh see ref. [15]

labeled PSXw, where X and w indicates the type of clay and the weight percent of clay, respectively. An additional letter "E" is added to indicate if the sample was prepared in an E-field. The samples were later studied with WAXS, optical microscopy, XMT, TGA, and finally the mechanical properties were characterized.

2.3 Characterization

2.3.1 Wide angle x-ray scattering (WAXS)

WAXS experiments were performed at beamline I911-4 of the MAX-lab synchrotron facility in Lund, Sweden [16]. All data were collected at a wavelength of 0.91 Å with a sample-to-detector distance of 481 mm or of 1900 mm, resulting in a covered q-range of about 1-10 and 0.1-3 nm^{-1}, respectively (q is the magnitude of the scattering vector and is defined as $q=4\pi\sin\theta/\lambda$ with λ being the wavelength and 2θ the scattering angle). The beam size at the sample position was approximately 300 × 300 microns. The detector used was a two-dimensional CCD (165 mm diameter from Mar Research, Inc). The samples were analyzed with the x-ray beam parallel or perpendicular (normal) to the E-field alignment direction (Figure 2).

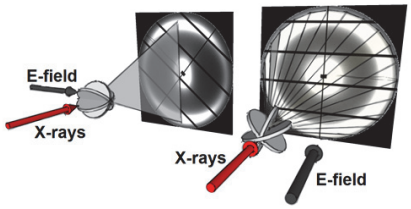

Figure 2 WAXS geometry when the samples are probed by the x-rays normal or parallel to the clay chains.

Data treatment was performed using the software FIT2D[17] and customized Matlab® routines. The data were normalized with respect to the transmitted intensity using a photodiode located inside the beam-stop. The peak broadening of the 001-reflection of the clay was used to estimate the thickness of the platelet stacking, L, by employing the Scherrer formula [18] $L = (K \cdot \lambda)/(FWHM \cdot \cos\theta)$ where K (~0.9) is a numerical constant, λ is the wavelength of the x-ray beam, $FWHM$ is the full width at half maximum of the Bragg-peak, and θ the Bragg angle. The average number of platelets in each stack was calculated by dividing the thickness with the d_{001}-spacing of the dispersed org-clay particles.

2.3.2 X-ray microtomography (XMT)

X-ray computed microtomography was performed with a voxel size of around 0.9µm using a custom-built Nanotom 180 NF XMT setup supplied by Phoenix|x-ray Systems + Services GmbH (Wunstorf, Germany), located at the Department of Physics at the University of Helsinki, Finland. This system is equipped with a tungsten x-ray source, a high-accuracy sample stage, and a CMOS-detector with 2304 × 2304 square pixels in cone beam imaging geometry. The XMT scans consisted of 1200 projection radiographs, each acquired as an average of 10 or 11 exposures of 500 ms. The x-ray tube voltage was set at 60 kV, and the current varied between 200-225 µA. Datos|x software provided by the equipment manufacturer was used to perform the reconstructions.

2.3.3 Thermogravimetric analysis (TGA)

TGA was performed on a Netsch STA 449 F3 Jupiter TGA-DSC instrument under argon atmosphere with a heating rate of 10 °C/min from 25 to 650 °C. Other instrumental parameters were adjusted with the software package STA 449F3. A 70 µL alumina crucible was used to hold the samples, which weighed between 2 and 5 mg.

2.3.4 Optical microscopy imaging

Pictures of the nanocomposites were taken with a Dinoeye Microscope Eye-piece digital camera mounted on a Nikon Optiphoto microscope.

2.3.5 Mechanical testing

The mechanical properties of the nanocomposites were measured in a custom built compression apparatus specifically designed for the 1 mm thick samples produced in our synthesis. The measurements were performed according to a modified version of the ASTM D695 standard, because of practical limits due to the small sample size. ASTM D695 states that a sample with dimensions of *0.5″ × 0.5″ × 1.0″ (~12.7 × 12.7 × 25.4 mm³)* is placed in the apparatus with compression along the long axis, and the rate of compression should be 1.27 mm/min. In the present work the elongated samples were cut to approximately 1 mm in length while the other two sides were already determined by the inner dimensions of the glass capillaries (~1.0 mm). Compression was performed against the two sides shaped by the capillaries, at a rate of 5 µm/s. Before every measurement the dimensions of the samples were carefully determined via the micrometer dial on the compression apparatus. The stress is expressed as $\sigma = F/A$, where F is the force applied to the sample area A at a given strain, $\varepsilon = l/L$, where l is the displacement and L the original width of the sample along the compression axis. Four to six pieces of each sample were measured in order to obtain averages and standard deviations. The samples were cut from the bottom and upwards in equal 1.0 mm long pieces, which were compressed alternatingly from different sides to even out

local effects in the samples. The procedure for examining the E-field aligned samples were similar, with compression alternatingly parallel or normal to the clay chains.

Figure 3 displays a typical stress-strain curve from the mechanical compression experiments. The yield strength is defined as the maximum stress applied to the sample before it fractures, and the compressive modulus is the slope in the linear region. To obtain consistent results, we have expressed the fracture toughness as the area given by the extrapolation of the linear region to the intersection with the yield strength value (shaded area).

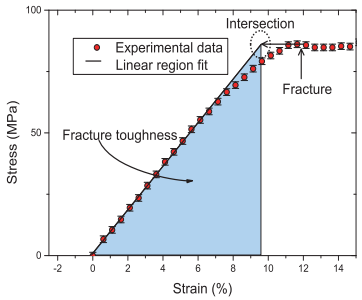

Figure 3 A typical stress-strain curve from testing the nanocomposites (here PSHT). The linear region is extrapolated to intersect with the yield strength. The shaded area corresponds to the fracture toughness. Error bars are marked on each data point.

3 RESULTS AND DISCUSSION

3.1 WAXS

3.1.1 In situ heating

The effect of heat on the dispersion of clay during the polymerization reaction of the synthesis was examined with *in situ* WAXS. org-Lp and org-Fh were dispersed in styrene at a concentration of 3 wt.% and sealed inside glass capillaries. These were measured with WAXS before and after several heating cycles between room temperature and 75 °C (a temperature we initially used for polymerization in this work). As shown in Table 2 the d_{001}-spacing of the clay increased after dispersion into styrene due to swelling when styrene molecules entered the silicate layers' galleries. Org-Lp increased its spacing from the initial 1.5 to 6.0 nm, while org-Fh increased somewhat less from 3.1 to 4.7 nm. During the heating cycles the org-Lp increased further to approximately 6.5 nm, while the spacing of org-Fh remained constant. The thickness of the clay stacks was roughly estimated with the Scherrer formula [18] and resulted in 10 nm for org-Lp, which corresponds to 1.5 platelets in each particle on average. org-Fh, on the other hand, displayed a stack-thickness of 80 nm, corresponding to 17 platelets per stack.

Table 2 Approximate d_{001}-spacings for org-Lp and org-Fh dispersed in Styrene at RT and after different heating cycles.

State	d001 Lp (nm)	d001 Fh (nm)
Dry org-clay	1.5	3.1
Dispersed in styrene	6.0	4.7
After 1st heating	6.1	4.7
After 2nd heating	6.3	4.7
After 3rd heating	6.5	-
Number of platelets in each stack	(~1.5)	~17

It is important to point out that since the 001-reflection of org-Lp is barely visible as a broad feature in the scattering pattern, one should be cautious interpreting the correlation peak as coming from a stacking morphology and using the Scherrer formula on this feature. However, the estimated value demonstrates how well-dispersed the org-Lp clay is before polymerization.

After the initial heating cycles, up to 75 °C, the Lp-sample was heated continuously from room temperature to 123 °C and subsequently cooled down to room temperature again, at a rate of 10 °C/min. WAXS-patterns were collected simultaneously every minute, and the calculated d_{001}-spacing from the WAXS-curves is shown to the left in Figure 4. Heating above RT increased the spacing, but it saturated at around 7.2 nm before dropping to 7.0 nm. During cooling it decreased to 6.5 nm again. This behavior may be explained by the increased kinetic energy gained by the intercalated styrene molecules at higher temperatures. With the increased energy the styrene molecules will exert more force against the clay platelets, and move them further apart by counteracting the electrostatic energy holding two adjacent clay platelets together. During cooling the surplus of kinetic energy is lost and the electrostatic energy forces the clay platelets closer again. Note that this effect can result in more than 10 % change in d-spacing.

The styrene-org-Fh dispersion was heated up to 146 °C, in several steps while collecting WAXS-patterns, since little effects were observed at moderate temperatures below 100 °C. The calculated d_{001}-spacing is shown to the right in Figure 4. Upon heating the spacing increased only slightly. The reason why org-Fh only showed moderate swelling is

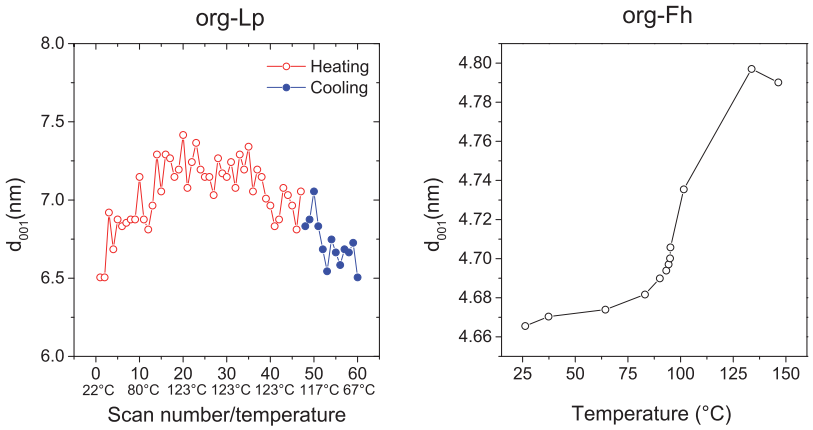

Figure 4 d_{001}-spacing of org-Lp (left) and org-Fh (right) dispersed in styrene during heating (and cooling for org-Lp).

attributed to the intrinsic surface charge, which is almost three times higher for Fh, and results in stronger electrostatic forces keeping the Fh-clay platelets closer together.

3.1.2 Scherrer analysis

WAXS curves, averaged over the whole 2D scattering images, of four E-field nanocomposites containing 3 wt.% clay, are shown in Figure 5. The 001-reflection is still very prominent, showing that the nanocomposites are of the intercalated type because the clays did not exfoliate completely during polymerization. Almost identical curves were obtained for the non-aligned samples, meaning that the

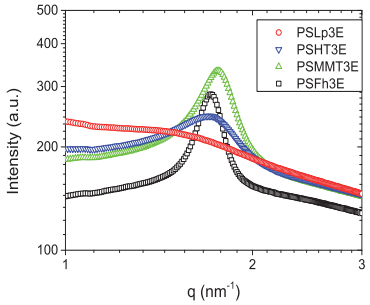

Figure 5 WAXS curves of four 3 wt.% PSNCs prepared inside an electric field.

E-field only oriented the tactoids but did not change their inner morphology (stacking distance). Even for PSLp3E the 001-reflection is visible, although the *in situ* heating experiment indicated that org-Lp swells considerably upon heating. The calculated d_{001}-spacing for the different samples are listed in Table 3. The spacing for the nanocomposites is noticeably smaller than for the clay dispersed in hot styrene (Table 2), and it seems to converge to a value between 3.6 and 4.1 nm. Similar basal spacings in PS-clay nanocomposites have been reported,[19-22] which might indicate that this spacing produces the optimum volume for a compact arrangement of PS chains between clay platelets. The estimated thickness of the clay stacks is listed in Table 3 together with the estimated number of platelets in each stack. The number of clay platelets in each stack is highly influenced by the surface charge of the clays, with an increased number for higher CEC, most probably due to the stronger electrostatic forces holding the stacks together.[1]

3.1.3 Anisotropy

The Bragg scattering from the 001-plane (stacking direction) of clay is directly correlated to the orientation of the clay particles with respect to the x-ray beam. Inside the E-field aligned samples the clay particles orient with the stacking direction perpendicular to the electric field (Figure 1) In principle one would not expect any preferred orientation around the E-field axis, but in our samples a large fraction of the particles align with the stacking direction perpendicular to the long axis of the sample, a point that we will discuss later.

The scattering patterns in the upper panels of Figure 6 were obtained from four different E-field aligned nanocomposites probed perpendicular (normal) to the chain direction. The strong anisotropic feature in the vertical

Table 3 Results from analysing WAXS-data of PSNCs.

Sample	CEC (meq/100g)	d_{001}-spacing in nanocomposite (nm)	Clay stack thickness (nm)	Average number of platelets in each stack
PSHT3E	43.9	3.7	26	7
PSLp3E	47	4.0	16	4
PSMMT3E	76.4	3.6	50	15
PSFh3E	120	3.7	68	19

direction is the 001-reflection of the stacking morphology, which shows that the clay particles are oriented with their stacking direction perpendicular to the electric field. The small angle scattering, close to the beam stop, is also anisotropic due to the shape of the clay particles.

When the samples were probed parallel to the electric field direction the scattering patterns in the lower panels of Figure 6 were produced. One would now also expect the scattering patterns to be isotropic because the clay platelets can have all possible orientations around the Electric field direction, and the scattering would thus produce a Debye-Scherrer cone, as is illustrated to the right in Figure 2.

For the samples produced here this only applies to the clay particles align with their platelets parallel to the inner, flat walls of the capillary, as is illustrated in Figure 7. Since clay particles in dispersion tend to align with the nearby walls of the supporting container as well as with each other,[23] this orientation can be translated inwards through the center of the sample. This effect is not seen for PSLp3E, probably because the aspect ratio of Lp is smaller than for the other clays, and therefore it does not align with the walls that easily. For the samples produced in absence of an electric field the 2D-patterns (not shown here) were isotropic.

3.1.4 X-ray microtomography (XMT)

X-ray XMT was used to examine the microstructure of the nanocomposites. As mentioned earlier the large x-ray

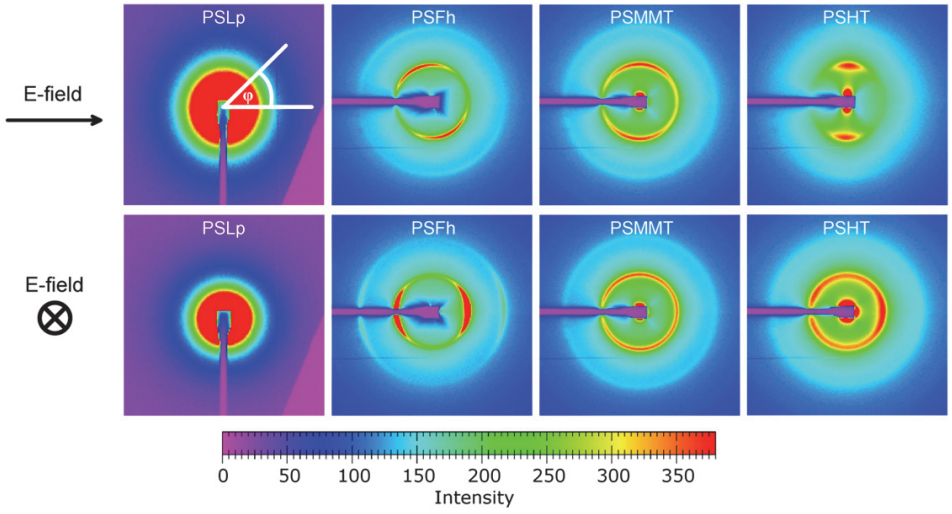

Figure 6 2D-scattering patterns for four 3 wt.% PSNCs polymerized in E-field, probed normal (upper panels) and parallel to the E-field direction. The azimuth angle, φ, is shown in the upper left pattern from PSLp3E.

PSLp3E while the scattering from the other three samples still contain anisotropic features, but they are shifted 90 degrees respective to the upper panels. This indicates that contrast between clay and the polymer allowed a more or less direct imaging of the clay particles alone. A comparison between the microstructure of the E-field aligned sample

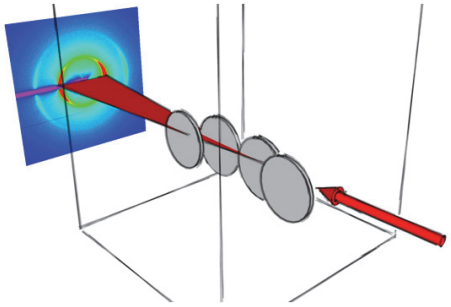

Figure 7 Sketch of how the clay platelets align with the walls of the capillary and how the anisotropic scattering pattern is produced from such an arrangement.

PSLp3E (left pane), and the non-aligned counterpart PSLp3 (right pane), is shown in Figure 8.

An immediate observation is that the clay particles are in both samples clearly visible inside the polymer matrix, showing up as bright features, larger than the voxel size of 0.9 μm. This corroborates our interpretation of the WAXS results, which indicated that the clay did not exfoliate completely. If full exfoliation had occurred, the clay platelets would have been smaller than the limiting resolution of the instrument used. A demonstration of this is given in Figure S1 in the supporting information, where a XMT slice of PSFh3E (intercalated type) is shown next to a slice of a fully exfoliated nylon 6-clay nanocomposite containing 5 wt.% Fh-clay. No signal from the clay can be discerned in the slice from the nylon 6-clay nanocomposite, while many bright spots are visible in the slice from PSFh3E.

The alignment of clay into chains in PSLp3E (left pane in Figure 8) can be discerned, whereas no such features are visible in the sample that had not been exposed to an E-field, and this sample displays a more homogenous microstructure. This is also illustrated in the *optical* microscopy images in Figure 9, where the non-aligned sample is homogenous.

The other E-field aligned samples did, however, not show any prominent chain structure in the XMT images (see Figure S2 in the supporting information). Since the WAXS results clearly indicated orientation of the clay platelets, we are confident that these samples also contained some chain-like features, even though these were not easily recognizable in the XMT images. These images further show significant agglomeration of the clay into larger particles. PSFh had the largest agglomerates of approximately 10-30 μm, which we believe can be linked to a lower miscibility between org-Fh

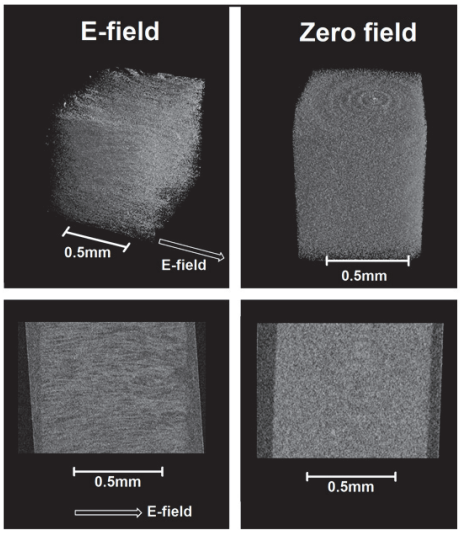

Figure 8 Comparison of microstructure between an E-field aligned PSNC (left pane, PSLp3E) and a non-aligned PSNC (right pane, PSLp3). XMT 3D-renderings are shown at the top while slices through the middle of the samples are shown at the bottom. The circular patterns in the upper right image are due to artifacts in the detector.

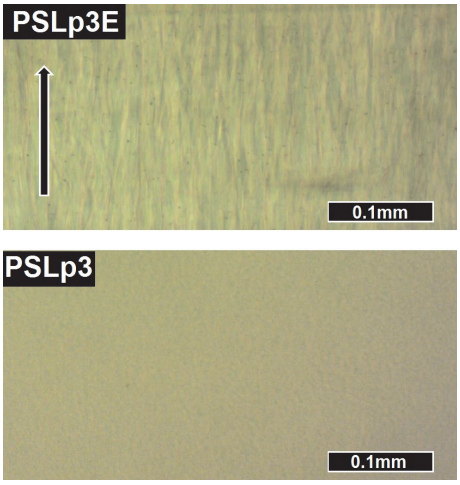

Figure 9 Optical microscopy of PSLp3E (E-field aligned) above and PSLp3 (no field) below. The direction of the E-field is indicated with the arrow. The scale bars are 100 μm long.

and PS. From the XMT images there was no significant effect from using E-fields or not on the size of the agglomerates.

3.2 Thermal behavior

Thermogravimetric analysis (TGA) of both types of nanocomposites, E-field aligned and non-aligned (zero-field), was performed to examine the thermal resilience of the nanocomposites. The respective TGA-curves are shown to the left in Figure 10 together with a curve from pure PS. The decomposition of the polymer matrix follows more or less the same path for each type of nanocomposite irrespective of alignment in E-field or not, and is also occurring at higher temperatures than for the pure polymer. This similarity in decomposition is expected since any effects of the alignment are lost when the PS-matrix melts and the clay obtains a random distribution.

The differentiated TGA curves (DTGA) to the right in Figure 10 display peaks, listed in Table 4, where the rate of decomposition is highest. What is noteworthy is that the decomposition temperature drops with higher CEC-value of the clay. We have earlier proposed that this might be linked to the dispersion of the clay platelets[1] which is less for clays carrying a high surface charge. The reduced dispersion leads to a less tortuous path for the decomposition products and hence these samples degrade a little earlier.

3.3 Mechanical properties

3.3.1 Comparison against Pure PS

The reinforcing effect of the different kinds of clay was compared by testing the nanocomposites with our custom compression tester. Apart from a few samples containing 1 wt.%, only 3 wt.% samples were inspected. A summary of the results from testing of four specimens of each nanocomposite, both aligned and non-aligned, can be found in Table 4. With a yield strength of 87.2 MPa, a value similar to that presented by Van Melick et al.[24], pure PS showed a higher yield strength than all PS-clay nanocomposites prepared in the present work, irrespective if the clays were aligned or not. However, a noticeable difference is induced when the clays are aligned, which will be discussed later. The decline in mechanical integrity when adding clay to PS differs from what can be found in the literature, which report *enhanced* mechanical properties for PS-clay nanocomposites [9,19,21,25]. This may be explained by the fact that, to our best knowledge, nearly all reported results from mechanical testing of PS-clay nanocomposites found in the literature are based under *elongation*, and not *compression* as was performed in the present work. However, there has been reported improved compressive properties in epoxy-MMT systems.[26]

Furthermore, only one study was found, by Burmistr et al. [27], which reports a decrease in tensile strength for melt-compounded PS-Bentointe composites. This decrease was explained by aggregation of organo-Bentonite platelets. The authors supported their claim by the fact that another batch of melt-compounded PS-clay composites using hydrophilic Na-Bentonite clay, displayed even worse properties and a

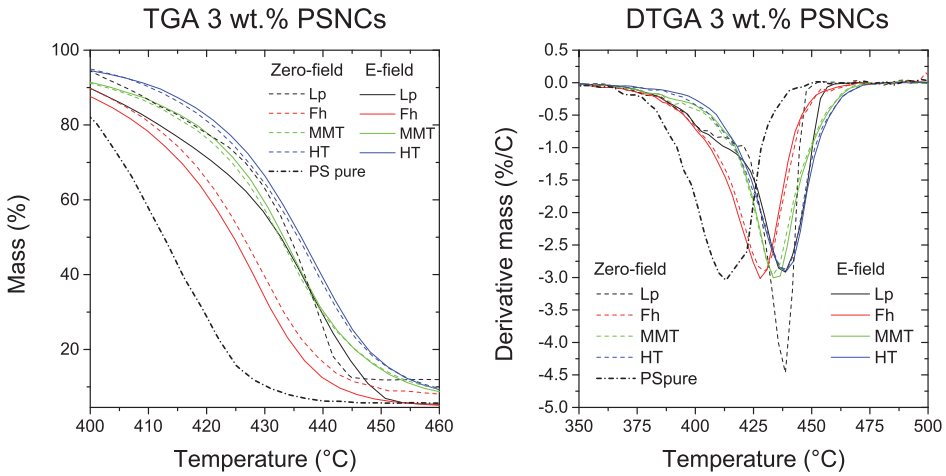

Figure 10 TGA and DTGA traces of 3 wt.% PSNCs. Solid lines: E-field, dashed lines: zero-field

Table 4 Yield strength, compressive modulus and fracture toughness of nanocomposites with 3 wt.% clay added. 3σ standard deviations are given in parenthesis. The rightmost column shows the temperature at maximum decomposition rate when tested with TGA.

Sample	Yield Strength (Mpa)	Compressive modulus (Mpa)	Fracture toughness (MJ/m^3)	Temp. at max decomp. Rate (°C)
Lp 3wt%				
zero-field	83.2 (4.1)	8.9 (0.2)	3.7 (0.3)	439
E-field	79.2 (4.5)	7.8 (0.6)	3.9 (0.5)	439
FH 3wt%				
zero-field	61.1 (5.0)	7.4 (0.5)	2.4 (0.4)	430
E-field	66.3 (7.9)	8.1 (1.0)	2.7 (1.0)	428
MMT 3wt%				
zero-field	74.1 (2.5)	8.9 (1.9)	3.0 (0.5)	435
E-field	76.7 (4.4)	8.7 (1.6)	3.3 (1.0)	435
HT 3wt%				
zero-field	82.5 (4.0)	8.9 (0.6)	3.7 (0.6)	438
E-field	80.1 (3.2)	8.2 (1.8)	3.8 (0.7)	439
PS avg 6 samples	87.2 (9.5)	9.0 (1.8)	4.2 (1.0)	410

more pronounced agglomeration. Our results, indicating inferior mechanical properties of the nanocomposites compared to pure PS may, similar to the results of Burmistr et al., also be explained by aggregation of small clay tactoids into larger particles, which reduces the dispersion. According to LeBaron et al. intercalated polymer-clay nanocomposites display improved rigidity (compressive modulus) at a cost of strength, elongation and toughness [26]. Apart from improved rigidity, this is similar to what we observed in the present study.

There are some differences in the mechanical properties between aligned samples and non-aligned. Without alignment (zero-field) the yield strength of PSLp3 and PSHT3 is comparable to pure PS, while PSMMT3 and PSFh3 have significantly lower strength. The compressive modulus is also similar to that of PS for all samples except for PSFh, which display a considerably lower value. Even though the first three samples showed similar modulus as PS, i.e. they resisted compression almost as well, their fracture toughness was lower. From both optical microscopy and cT it was observed that the org-Fh particles agglomerated into large micrometer sized (up to 30 μm) entities that could have facilitated crack generation [10] in the PS-matrix, rather than prevented it.

Comparing the effects of the type of clay added it seems clear that the surface charge of the clays indirectly induced significant differences in both the toughness and strength of the nanocomposites. A lower surface charge may have led to increased dispersion for org-Lp and org-HT, which ultimately resulted in better mechanical properties.

3.3.2 Effect of E-field

When the nanocomposites were polymerized using E-field alignment it was expected that they would generally display different properties when the compression was in the parallel or perpendicular direction to the clay chains. However, significant differences between the two directions of compression were found only for two samples. For the others the data were averaged over the two data sets for each sample to improve the statistics.

The PSFh3E nanocomposite displayed an increase in both yield strength and modulus, whereas the other samples actually showed inferior properties compared to the non-aligned samples. We believe the slightly impaired properties of the aligned nanocomposites may be due to an increased agglomeration of the clay particles when they aligned into chains. Earlier studies performed by our co-workers have reported that after some time, the chains can agglomerate into thicker column-like structures.[12,13,28] This would ultimately lead to a less homogenous composite network.

The relative increase in toughness for all the E-field aligned samples compared to the non-aligned may be caused by the buildup of thick clay chains. Because the PS-domains are now larger, and span a more continuous volume in between the clay chains/columns, they can distort more freely and absorb more energy before the material fails.

3.3.3 *Mechanical anisotropy*

Interestingly, two of the E-field aligned samples displayed anisotropy in the mechanical properties. These PSLp samples with 1 and 3 wt.% clay, respectively, were polymerized at a slightly lower temperature than the other samples, at 80 °C. The stress-strain curves of the 3 wt.% sample are shown in Figure 11.

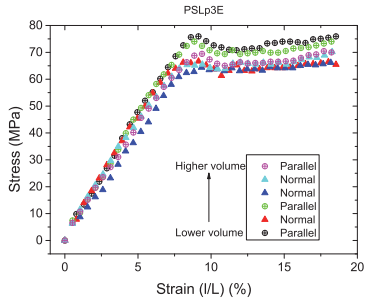

Figure 11 Stress-strain curves of a PSLp3E nanocomposite polymerized inside an electric field. The curves were obtained by compression parallel or normal to the clay chains.

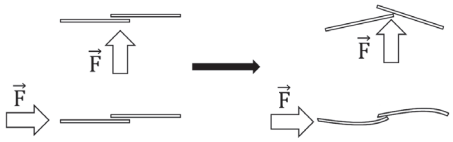

Figure 12 Simplified sketch of the forces working on clay platelets inside a nanocomposite during compression. The platelets are viewed from the side.

The necking of the curves, indicating the yield strength, occurred at a significantly higher load when the sample was compressed along the chains. A section of around 8 mm of this sample was cut into pieces that were tested alternatingly parallel and perpendicular to the chains to even out local effects from the clay concentration. The different parts are plotted together to show this result was in fact significant.

We believe a possible explanation to the observed mechanical anisotropy is that since the clay platelets align with their long axis along the E-field the compression forces will have a larger area to work on, when this occurs transverse to the long axis compared to when the compression is performed parallel to the clay chains. This is illustrated in Figure 12. The larger area may make it easier to distort the position of the clay platelets which results in a softer material with lower strength. Furthermore, compression parallel to the clay chains may on the other hand be more difficult because the platelets do not bend easily inside the PS-matrix (see bottom of Figure 12). Further work needs to be carried out to elucidate why only these two samples displayed anisotropic mechanical properties.

3.3.4 *Effect of clay weight fraction*

To test how the clay weight fraction affected the changes in mechanical properties a batch of 1 wt.% HT and MMT nanocomposites was also produced and their mechanical properties were tested. The comparison between the 1 wt.% and 3 wt.% samples, given in Table 5, shows that all of the three properties degenerated when the amount of clay increased.

The two 1 wt.% samples (HT and MMT) performed almost on par with pure PS which may indicate that the amount of clay is so small that it has no significant contribution on the mechanical properties. The stiffness (compressive modulus) for these two samples, on the other hand, was improved compared to PS. TGA (see Figure S3 in the supporting information) demonstrated that the temperature at maximum decomposition rate for the 1 wt.% samples, listed in Table 5 was almost as high as for the 3 wt.% counterparts. This result can be of interest since the thermal stability of the nanocomposite may be improved without the loss of mechanical integrity. Again, no significant change in decomposition temperature was observed between the E-field and zero-field samples.

Table 5 Yield strength, compressive modulus and fracture toughness of nanocomposites with 1 and 3 wt.% of clay added. 3σ standard deviation in parenthesis. The rightmost column shows the temperature at maximum decomposition rate when tested with TGA.

Sample	Yield Strength (Mpa)	Compressive modulus (Mpa)	Fracture toughness (MJ/m³)	Temp. at max decomp. Rate (°C)
MMT 1 wt%				
zero-field	86.9 (8.6)	9.2 (0.9)	4.0 (0.4)	433
E-field	83.2 (2.7)	8.4 (0.4)	3.8 (0.6)	431
MMT 3 wt%				
zero-field	74.1 (2.5)	8.9 (1.9)	3.0 (0.5)	435
E-field	76.7 (4.4)	8.7 (1.6)	3.3 (1.0)	435
HT 1 wt%				
zero-field	86.8 (11.6)	9.7 (0.6)	3.9 (0.8)	434
E-field	79.6 (7.1)	8.8 (2.6)	3.5 (0.5)	433
HT 3 wt%				
zero-field	82.5 (4.0)	8.9 (0.6)	3.7 (0.6)	438
E-field	80.1 (3.2)	8.2 (1.8)	3.8 (0.7)	439
PS avg 6 samples	87.2 (9.5)	9.0 (1.8)	4.2 (1.0)	410

4 CONCLUSIONS

Polystyrene-clay nanocomposites with four different types of clay were synthesized and characterized with WAXS, x-ray XMT and TGA, and the mechanical properties during compressive stress was examined. The WAXS and XMT results indicated that the nanocomposites were of the intercalated type, with increased dispersion of the clay for the low-CEC clays Hectorite and Laponite. *In situ* WAXS studies suggested that the d_{001}-spacing of the org-clays increased when they were dispersed in the styrene monomer. Further swelling was observed as the temperature was increased, but this was, however, only temporary since the d-spacing returned to the initial value upon cooling to room temperature. Furthermore, the WAXS results revealed that inside the E-field aligned samples, the clay platelets aligned themselves with their flat surface parallel to the walls of the enclosing glass capillaries used during synthesis.

TGA showed increased thermal resilience for all nanocomposites, as reported previously,[1] although o differences between aligned or non-aligned samples was observed.

Overall the mechanical properties of the nanocomposites were inferior to pure PS, with one exception. PSHT1 (non-aligned) displayed almost the same properties as pure PS. Since the high-temperature resilience of PSHT1 are far better than that of PS we find small additions (~1 wt.%) of surface modified Hectorite clay beneficial for the improvement of PS.

ACKNOWLEDGEMENTS

This work was performed under the sponsorship of The Research Council of Norway. The beam time provided by MAX-Lab is also acknowledged.

AUTHOR INFORMATION

Corresponding author

*E-mail: kenneth.knudsen@ife.no; henrik.mauroy@ife.no

REFERENCES

(1) Mauroy, H.; Plivelic, T. S.; Hansen, E. L.; Fossum, J. O.; Helgesen, G.; Knudsen, K. D. The Effect of Clay Surface Charge on the Emerging Properties of Polystyrene-Organoclay Nanocomposites. *Accepted August 2013 Journal of Physical Chemistry C* **2013**.

(2) Liu, T. J.-C.; Wu, H.-C. Fiber Direction and Stacking Sequence Design for Bicycle Frame Made of Carbon/Epoxy Composite Laminate. *Materials & Design* **2010**, 31, 1971-1980.

(3) Richard, D. Automotive Suspension Systems Benefit from Composites. *Reinforced Plastics* **2003**, 47, 18-21.

(4) Virk, A. S.; Summerscales, J.; Hall, W.; Grove, S. M.; Miles, M. E. Design, Manufacture, Mechanical Testing and Numerical Modelling of an Asymmetric Composite Crossbow Limb. *Composites Part B-Engineering* **2009**, 40, 249-257.

(5) Kelly, A. Very Stiff Fibres Woven into Engineering's Future: A Long-Term Perspective. *Journal of Materials Science* **2008**, 43, 6578-6585.

(6) Chawla, K. K. Foams, Fibers, and Composites: Where Do We Stand? *Materials Science and Engineering a-Structural Materials Properties Microstructure and Processing* **2012**, 557, 2-9.
(7) Kojima, Y.; Usuki, A.; Kawasumi, M.; Okada, A.; Fukushima, Y.; Kurauchi, T.; Kamigaito, O. Mechanical Properties of Nylon 6-Clay Hybrid. *J. Mater. Res.* **1993**, 8, 1185-1189.
(8) Haraguchi, K.; Takehisa, T. Nanocomposite Hydrogels: A Unique Organic-Inorganic Network Structure with Extraordinary Mechanical, Optical, and Swelling/De-Swelling Properties. *Adv. Mater.* **2002**, 14, 1120-1124.
(9) Utracki, L. A. *Clay-Containing Polymeric Nanocomposites*; Smithers Rapra Technology: Shrewsbury, U.K., 2004.
(10) Moczo, J.; Pukanszky, B. Polymer Micro and Nanocomposites: Structure, Interactions, Properties. *Journal of Industrial and Engineering Chemistry* **2008**, 14, 535-563.
(11) Fossum, J. O.; Meheust, Y.; Parmar, K. P. S.; Knudsen, K. D.; Maloy, K. J.; Fonseca, D. M. Intercalation-Enhanced Electric Polarization and Chain Formation of Nano-Layered Particles. *Europhys. Lett.* **2006**, 74, 438-444.
(12) Rozynek, Z.; Mauroy, H.; Castberg, R. C.; Knudsen, K. D.; Fossum, J. O. Dipolar Ordering of Clay Particles in Various Carrier Fluids. *Cuban Journal of Physics, Revista Cubana de Fisica* **2012**, 29, 37-41.
(13) Wang, B. X.; Zhou, M.; Rozynek, Z.; Fossum, J. O. Electrorheological Properties of Organically Modified Nanolayered Laponite: Influence of Intercalation, Adsorption and Wettability. *J. Mater. Chem.* **2009**, 19, 1816-1828.
(14) The Clay Minerals Society. Source Clay Physical/Chemical Data. http://www.clays.org/SOURCE%20CLAYS/SCdata.html Apr. 04 DateAccess. 2013
(15) Kaviratna, P. D.; Pinnavaia, T. J.; Schroeder, P. A. Dielectric Properties of Smectite Clays. *J. Phys. Chem. Solids* **1996**, 57, 1897-1906.
(16) Plivelic, T. S.; Labrador, A. L.; Theodor, K.; Gaponov, Y.; Svensson, C.; Nygaard, J.; Cerenius, Y. In *8th Nordic Workshop on Scattering from Soft Matter* Kjeller, Norway, 2011.
(17) Hammersley, A. P.; Svensson, S. O.; Hanfland, M.; Fitch, A. N.; Hausermann, D. Two-Dimensional Detector Software: From Real Detector to Idealised Image or Two-Theta Scan. *High Pressure Res.* **1996**, 14, 235-248.
(18) Patterson, A. L. The Scherrer Formula for X-Ray Particle Size Determination. *Physical Review* **1939**, 56, 978-982.
(19) Hasegawa, N.; Okamoto, H.; Kawasumi, M.; Usuki, A. Preparation and Mechanical Properties of Polystyrene-Clay Hybrids. *J. Appl. Polym. Sci.* **1999**, 74, 3359-3364.
(20) Mitchell, C. A.; Krishnamoorti, R. Rheological Properties of Diblock Copolymer/Layered Silicate Nanocomposites. *J. Polym. Sci., Part B: Polym. Phys.* **2002**, 40, 1434-1443.
(21) Arora, A.; Choudhary, V.; Sharma, D. K. Effect of Clay Content and Clay/Surfactant on the Mechanical, Thermal and Barrier Properties of Polystyrene/Organoclay Nanocomposites. *Journal of Polymer Research* **2011**, 18, 843-857.
(22) Qi, R.; Jin, X.; Huang, S. Synthesis and Characteristics of Polystyrene-Clay Nanocomposites Via in Situ Intercalative Polymerization in a Direct Current Electric Field. *J. Appl. Polym. Sci.* **2010**, 115, 2723-2727.
(23) Hemmen, H.; Ringdal, N. I.; De Azevedo, E. N.; Engelsberg, M.; Hansen, E. L.; Meheust, Y.; Fossum, J. O.; Knudsen, K. D. The Isotropic-Nematic Interface in Suspensions of Na-Fluorohectorite Synthetic Clay. *Langmuir* **2009**, 25, 12507-12515.
(24) van Melick, H. G. H.; Govaert, L. E.; Meijer, H. E. H. Localisation Phenomena in Glassy Polymers: Influence of Thermal and Mechanical History. *Polymer* **2003**, 44, 3579-3591.
(25) Zhu, J.; Morgan, A. B.; Lamelas, F. J.; Wilkie, C. A. Fire Properties of Polystyrene-Clay Nanocomposites. *Chem. Mater.* **2001**, 13, 3774-3780.
(26) LeBaron, P. C.; Wang, Z.; Pinnavaia, T. J. Polymer-Layered Silicate Nanocomposites: An Overview. *Appl. Clay Sci.* **1999**, 15, 11-29.
(27) Burmistr, M. V.; Sukhyy, K. M.; Shilov, V. V.; Pissis, P.; Spanoudaki, A.; Sukha, I. V.; Tomilo, V. I.; Gomza, Y. P. Synthesis, Structure, Thermal and Mechanical Properties of Nanocomposites Based on Linear Polymers and Layered Silicates Modified by Polymeric Quaternary Ammonium Salts (Ionenes). *Polymer* **2005**, 46, 12226-12232.
(28) Rozynek, Z.; Wang, B.; Zhou, M.; Fossum, J. O. Dynamic Column Formation in Na-Flhc Clay Particles: Wide Angle X-Ray Scattering and Rheological Studies. *J. Phys.: Conf. Ser.* **2009**, 149, 012026.

Anisotropic polystyrene-clay nanocomposites: Synthesis, characterization and mechanical properties

Henrik Mauroy[a,], Tomás S. Plivelic[b] , Jussi-Petteri Suuronen[c], Jon Otto Fossum[d] and Kenneth D. Knudsen[a,d,]**

[a]Physics department, Institute for Energy Technology, P.O. Box 40, N-2027 Kjeller, Norway

[b]MAX IV Laboratory, Lund University, P.O. Box 118, SE-221 00 Lund, Sweden

[c]Department of Physics, Division of Materials Physics, University of Helsinki, P.O.B. 64, FI-00014, Finland

[d]Department of Physics, Norwegian University of Science and Technology, Hoegskoleringen 5, N-7491 Trondheim, Norway

Supporting information

1 X-ray computed microtomography (XMT)

XMT was performed on different polymer-clay nanocomposites. Figure S1 compares the dispersion of org-Fluorohectorite (CTAB-modified) in polystyrene (Figure S1a) against 11-Fluorohectorite (11-aminoundecanoic acid modified) dispersed in nylon 6 (Figure S1b). The clay platelets are dispersed to such an extent in the nylon 6 matrix that the particle size becomes smaller than the resolution of 0.9 μm. (The speckle pattern is noise from the detector and the circular features are due to artifacts in the detector.) The dispersion is worse in the polystyrene matrix indicated by the large bright spots due to large agglomerations of clay

* Corresponding author. Tel/Fax: +47 63 80 60 81/+47 63 81 09 20
E-mail address: henrik.mauroy@ife.no and kenneth.knudsen@ife.no

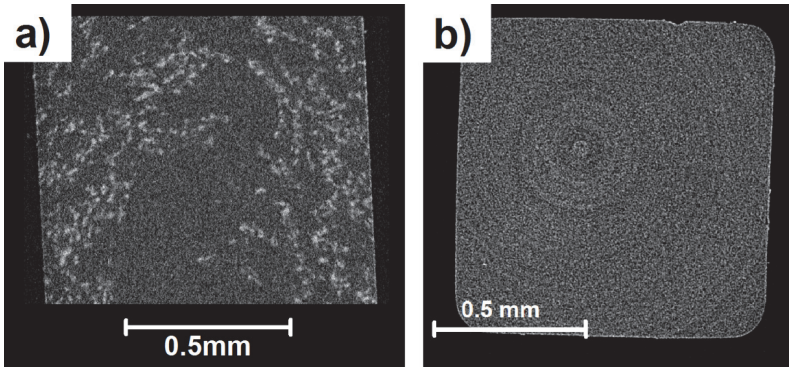

Figure S1 *XMT slices of two different types of nanocomposites using surface modified Li-Fluorohectorite as filler: (a) PSFh3E (intercalated type), (b) nylon 6-clay nanocomposite containing 5 wt.% Fh-clay (exfoliated type). The circular patterns in b) are due to artifacts in the detector.*

Figure S2 shows XMT 3D-renderings and tomography-slices of E-field aligned polystyrene-clay nanocomposites with different types of org-clay added.

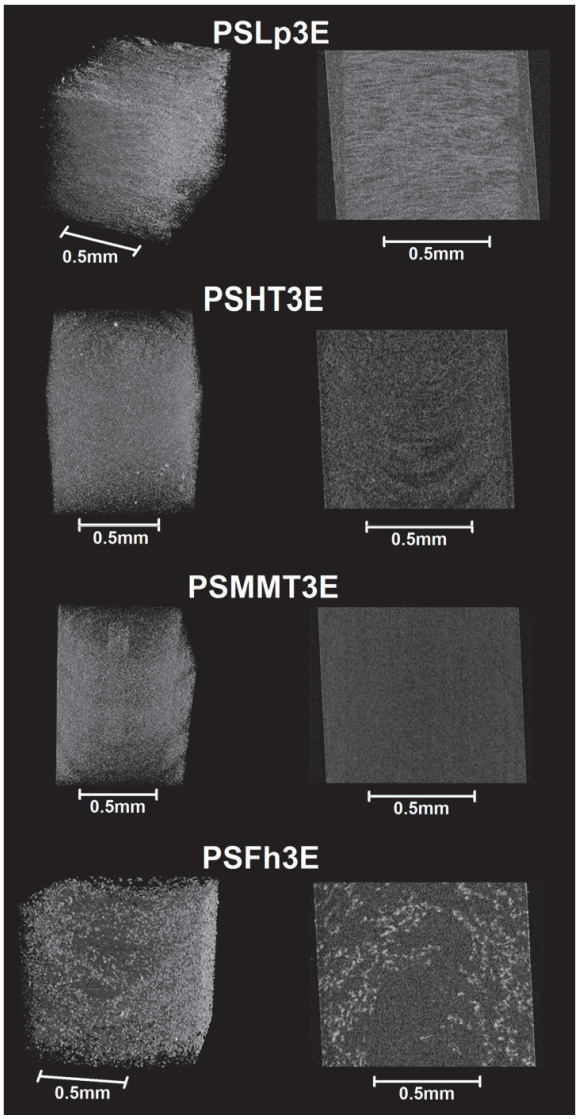

Figure S2 *XMT of E-field aligned PSNCs containing 3 wt.% org-clay. The left pane shows 3D-renderings of 1 x 1 mm samples while the right panel shows slices in the middle of the samples. The direction of the E-field used for alignment is along the same direction as the various scale bars.*

2 Thermogravimetric analysis (TGA)

The high-temperature resilience of polystyrene-clay nanocomposites, with 1 wt.% clay added, was studied with TGA. Figure S3 shows TGA and DTGA traces of these samples together with traces from pure PS. Clearly only a small weight fraction of clay is needed to increase the decomposition temperature of PS.

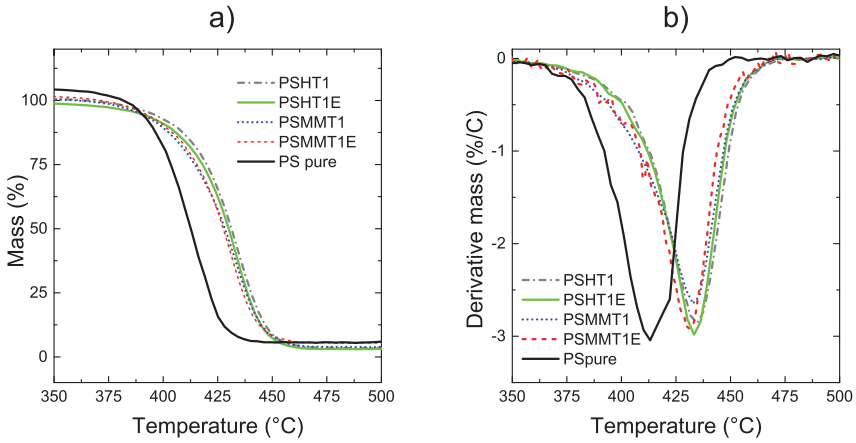

Figure S3 *TGA and DTA traces of 1 wt.% PSNCs and pure PS.*

IV

Manuscript in preparation

Synthesis and characterization of nylon 6/clay nanocomposites using different 2:1 smectic clays

Henrik Mauroy*[,a,b], Jussi-Petteri Suuronen[c] and Kenneth D. Knudsen*[,a,d]

[a]Physics department, Institute for Energy Technology, P.O. Box 40, N-2027 Kjeller, Norway
[b]Department of Physics, University of Oslo, N-0316 Oslo, Norway
[c]Department of Physics, Division of Materials Physics, University of Helsinki, P.O.Box 64, FI-00014, Finland
[d]Department of Physics, Norwegian University of Science and Technology, Hoegskoleringen 5, N-7491 Trondheim, Norway

ABSTRACT: Several nylon 6/clay nanocomposites were prepared using four different 2:1 clays with varying surface charge. 11-aminoundecanoic acid was used both as surfactant for the clay and as co-polymerizer. The resulting surface modified clays and nanocomposites were characterized with wide angle x-ray scattering (WAXS), thermogravimetric analysis (TGA) and x-ray computed microtomography (XMT). The mechanical properties were also studied under compression. The results indicate that a larger surface charge leads to increased intercalation of surfactant, improved dispersion of clay in the polymer matrix, and finally enhanced mechanical properties compared to pristine nylon 6.

1 INTRODUCTION

Nylon 6/clay nanocomposites were developed by the Toyota motor group in the early 1990's.[1-3] The materials were synthesized in a one-pot method where surface modified Montmorillonite clay nanoparticles (MMT) were dispersed in liquid ε-caprolactam monomer. The resulting materials had superior thermal properties compared to pristine nylon 6, and the composites were quickly used in one of Toyota's production cars.[3] Since then there has been a formidable interest in other polymer nanocomposites as well, due to the outstanding properties these materials exhibit, e.g. improved mechanical strength, water and oxygen barrier properties, improved thermal stability and flame retardation, scratch and wear resistance, chemical resistance, as well as optical, magnetic, and electrical properties.[4]

In the present work we have synthesized and characterized a range of nylon 6/clay nanocomposites using three different 2:1 smectic clays in addition to the widely used MMT clay. This work was originally performed as a preliminary study of the synthesis itself and the resulting nanocomposites, but since there were a series of interesting findings in this process, we felt justified to present it as a separate manuscript. We show how the uptake of surfactant is related to the clay surface charge, and how the amount of surfactant affects the intercalation of monomer and indirectly the mechanical properties of the final nanocomposites.

2 EXPERIMENTAL

2.1 Chemicals

ε-caprolactam (99%) and 11-aminoundecanoic (11-acid, 97%) were purchased from Sigma-Aldrich. Two synthetic 2:1 clays, Laponite XLG (Lp) and Li-Fluorohectorite (Fh), were kindly donated by Andreas Jennow AB (Lp), and purchased from Corning Inc (Fh), respectively. Two natural 2:1 clays, Na-Montmorillonite SWy-2 (MMT) and Hectorite SHCa-1 (HT), were purchased from The Clay Minerals Society Repository. The chemicals were used as received and the water used was of deionized purity.

2.2 Surface modification of clays

Preparation of the surface modified clays (11-clays) was performed based on the procedure reported by Usuki et al.[1] using a simple cation exchange reaction: 10 g clay was dispersed in 600 mL water and stirred at 80 °C for 2 hours. The dispersions containing HT and MMT clay was left to settle for 3 hours to remove the largest silicate impurities. Subsequently the liquid phase was sentrifuged at 700G for 25 minutes to remove clay particles larger than ~1 μm.[5] The clay concentration of the, now stable, suspensions was determined by evaporating a known volume of sample and weighing the residue. An amount of 11-acid, corresponding to 4 times the CEC of each clay, was dissolved in 150 mL HCl-solution of pH = 3.8. The acid treatment protonates the amino group in 11-acid, making it positively charged.

Subsequently the clay suspensions were heated to 80 °C, and the cold 11-acid solution was poured gently in under stirring. Almost immediately, flocks of hydrophobic surface modified 11-clay precipitated. The 11-clay/water mixture was stirred for 6 hours at 80 °C and subsequently stirred at RT for 15-20 hours. The solutions were decanted and suction filtrated, and the precipitate was washed with 100 mL deionized water, stirred for 1 hour and suction filtrated again. Washing and filtration was repeated up to 6 times to remove any residual 11-acid and HCl. After each washing cycle the waste solutions were checked for Cl^- ions by adding some drops of 0.5 M $AgNO_3$. After the last filtration, the filtrate was dried in an oven at 80 °C overnight, crushed to a fine powder in a mortar, and stored in a sealed container until further studies.

2.3 Melt-intercalation and polymerization

The procedure used for synthesis of N6NCs in the present work deviates somewhat from the method used by Usuki et al,[1] and was as follows: 0.80 g ε-caprolactam was ground in a mortar together with 0.05 g 11-clay and 0.15 g 11-acid (5 wt.% and 10 mol% of the ε-caprolactam, respectively). The powder mixture was then heated in a 100 °C water bath and stirred with a magnetic stirrer for 1 hour to perform melt-intercalation of ε-caprolactam monomer into the clay galleries. Subsequently the monomer mix was filled in liquid state into 1 mm square shaped capillaries and a small amount of epoxy glue was used as stoppers in both ends of the monomer mix. After the glue had hardened, both ends of the capillary were evacuated and sealed with a flame torch. The samples were finally polymerized in an oven at 260 °C for 5 hours. After polymerization the capillaries were cut open and the nanocomposites were carefully pulled out and stored in sealed glass bottles for further analysis. The samples were labeled N6X where X is the abbreviation for each clay type, i.e. N6HT for a Hectorite containing sample etc. The finished nanocomposites are shown together with a pure nylon 6 sample in Figure 1. It is noteworthy that N6MMT is almost as transparent as pure nylon 6, indicating that the 11-MMT clay was exfoliated and well-dispersed. N6HT and N6Lp on the other hand were completely opaque, while N6Fh had a certain transparency.

2.4 Wide angle x-ray scattering (WAXS)

WAXS experiments were performed at beam line I911-4 of the MAX-lab synchrotron facility in Lund, Sweden.[6] All data were collected at a wavelength of 0.91 Å with a sample-to-detector distance of 481 mm, resulting in a covered q-range of about 1-10 nm^{-1}. The beam size at the sample position was approximately 300 × 300 μm. The detector used was a two-dimensional CCD (165 mm diameter from Mar Research, Inc). Data treatment was performed using the software FIT2D.[7]

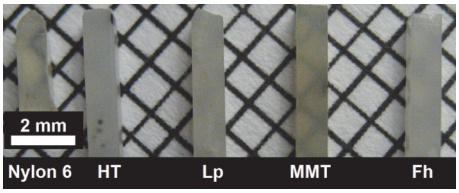

Figure 1 Picture of the polymerized nylon 6/clay nanocomposites together with a pure nylon 6 sample.

2.5 Thermogravimetric analysis (TGA)

TGA was performed on a Netsch STA 449 F3 Jupiter TGA-DSC instrument under argon atmosphere with a heating rate of 10 °C/min from 25 to 650 °C. Other instrumental parameters were adjusted with the software package STA 449F3. A 70 μL alumina crucible was used to hold the samples, which weighed around 15 mg. The weight fraction of surfactant in the 11-clays was defined as the mass loss above 150 °C (i.e. nearly all water had evaporated).

2.6 Energy dispersive x-ray spectroscopy (EDS)

The extent of surface modification of the clays was investigated using EDS, in a Hitachi S-4300SE field emission scanning electron microscope. The samples were carbon coated and attached to an aluminium stub using double-sided conductive carbon tape.

2.7 Mechanical testing

The mechanical properties during compression were investigated using a custom built compression apparatus specifically designed for the 1 mm thick samples produced in our synthesis. The samples were cut into ~1.0 mm long pieces, and compression was performed against the two sides shaped by the capillaries, at a rate of 5 μm/s. Before every measurement the dimensions of the samples were carefully determined via the micrometer dial on the compression apparatus. The stress is expressed as $\sigma = F/A$, where F is the force applied to the sample area A at a given strain, $\varepsilon = l/L$, where l is the displacement and L the original width of the sample along the compression axis. Four to six pieces of each sample were measured in order to obtain averages and standard deviations.

2.8 X-ray computed μ-Tomography

X-ray computed microtomography (XMT) was performed with a voxel size of around 0.9μm using a custom-built Nanotom 180 NF XMT setup supplied by Phoenix|x-

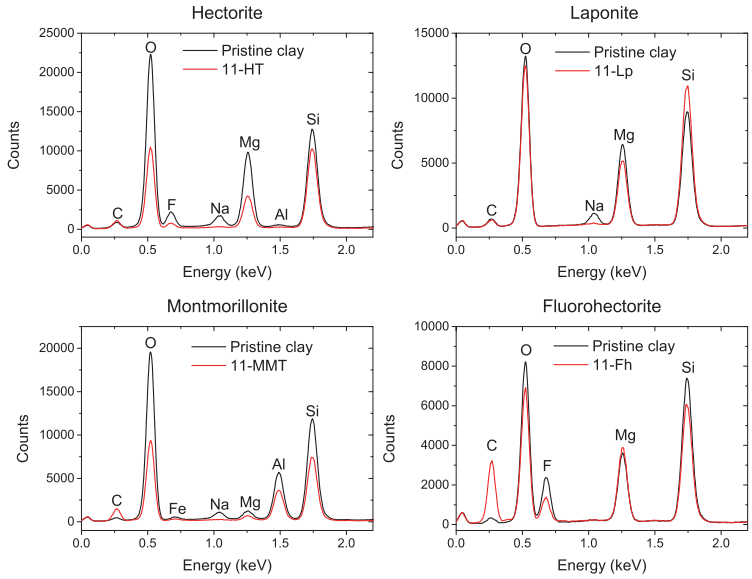

Figure 2 SEM EDS spectra from the four 11-clays shown together with the spectra from the pristine clays.

ray Systems + Services GmbH (Wunstorf, Germany) located at the Department of Physics at the University of Helsinki, Finland. This system is equipped with a tungsten x-ray source, a high-accuracy sample stage, and a CMOS-detector with 2304 × 2304 square pixels in cone beam imaging geometry. The XMT scans consisted of 1200 projection radiographs, each acquired as an average of 10 or 11 exposures of 500 ms. The x-ray tube voltage was set at 60 kV, and the current varied between 200-225 μA. Datos|x software provided by the equipment manufacturer was used to perform the reconstructions. The samples were cut into ~1.0 mm long pieces prior to examination.

3 RESULTS AND DISCUSSION

3.1 EDS of 11-clays

To obtain information of how well the surface modification had proceeded, the elemental composition of the 11-clays were studied with EDS in a scanning electron microscope (SEM). Figure 2 shows EDS spectra from the four 11-clays together with spectra from pristine clays.

The x-ray signal from Na is absent in the spectra for 11-HT, 11-Lp and 11-MMT which means that nearly all counterbalancing cations were substituted by 11-acid during the surface modification. In 11-Fh, on the other hand, Li^+ was substituted, which is undetectable by the system used, and hence the spectrum could not indicate if Li^+ was fully substituted. Since 11-acid contains one nitrogen atom per

Table 1 Experimental details of the clays and results from analyzing them with TGA and WAXS

Clay type	Exchangeable cation†	CEC (meq/100g)†	Pure clay d_{001}-spacing (nm)	11-clay d_{001}-spacing (nm)	Weight fraction of surfactant (wt.%)
HT	Na, Mg	44	1.10	1.37	9
Lp	Na	47	1.30	1.37	9
MMT	Ca,Na	76	1.24	1.33	18
Fh	Li	120	1.20	1.75	24

† HT, MMT see ref. [8], Lp, Fh see ref. [9]

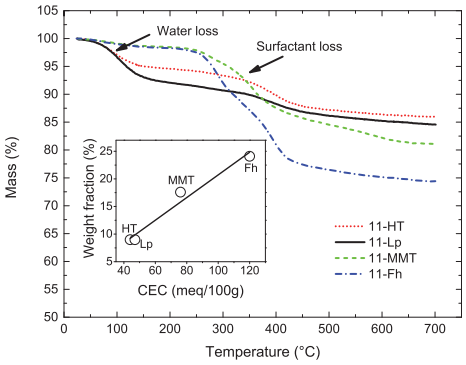

Figure 3 TGA-curves of the 11-clays.

molecule, one could expect that a peak from nitrogen would appear in the spectra from the 11-clays. The x-ray emission from nitrogen, however, has an energy (0.392 keV) which is in between the values from carbon (0.277 keV) and oxygen (0.525 keV) so this peak would only appear as a small shoulder to the peaks from the latter two due to the small amounts of nitrogen present in the 11-clays. (The peak from carbon is due to the carbon tape used to fix the powders to the sample holder.)

3.2 TGA of 11-clays

Thermogravimetric analysis (TGA) in the range 25-700 °C was performed to quantify the amounts of 11-acid that was intercalated into the clay structures. The results are listed in Table 1. As we also pointed out in another work, see ref. [10], the amount of surfactant which is intercalated is almost linearly dependent on the amount of surface charge if the surfactant is in surplus during synthesis (see inset Figure 3).

Due to the much larger CEC of Fh and MMT compared to Lp and HT (see Table 1), the former two intercalated more 11-acid, while 11-HT and 11-Lp intercalated almost equal amounts. One feature of the TGA-curves is the mass loss up to around 150 °C, which is caused by water being released from the 11-clays. This water was absorbed from the ambient air during storage. Interestingly 11-Lp and 11-HT contained significant amounts of water compared to 11-MMT and 11-Fh. The reason for this may be connected to the larger amounts of surfactant present in the high-CEC clays, MMT and Fh, which made these more hydrophobic than the other two clays.

3.3 WAXS: 11-clays and melt-intercalated 11-clays

The pure and the surface modified clays were probed with

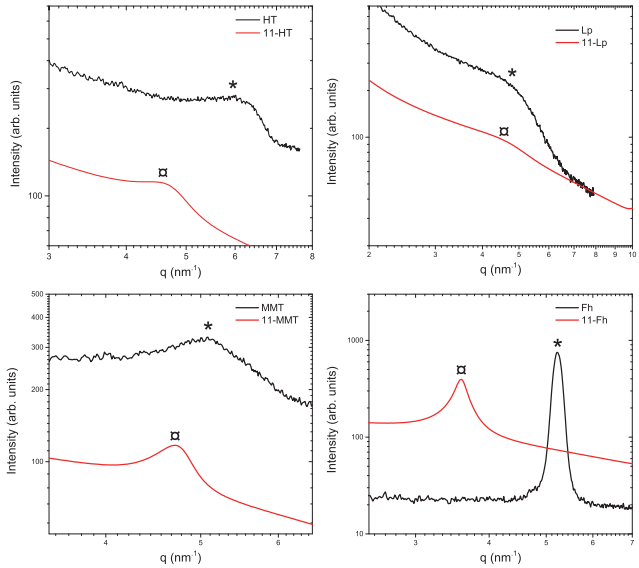

Figure 4 WAXS curves around the 001 reflection of the 11-clays. The 001 reflections are marked with (*) and (¤) for the pristine clays and the 11-clays, respectively.

WAXS to measure the change in d_{001}-spacing when the clays intercalated 11-acid. The WAXS-curves around the 001 reflection from the 11-clays are shown in Figure 4. The d-spacing increased markedly for all clays, but 11-Fh had the largest increase, up to almost 1.8 nm, due to intercalation of a large amount of surfactant. This corroborates the TGA results which indicated a much larger uptake of surfactant for the clays with larger surface charge.

Although 11-MMT displayed a much larger weight fraction of surfactant than 11-HT and 11-Lp (18 wt.% vs. 9 wt.%), its d-spacing increased only to 1.33 nm. The resulting d-spacing of 11-HT and 11-Lp of 1.37 nm was slightly larger. A reason for this may be that a large fraction of intercalated water was also present in the two latter 11-clays during the WAXS acquisition, cf. the TGA-section above.

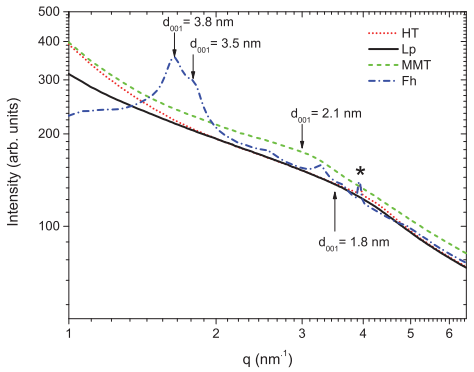

Figure 5 WAXS curves of melt-intercalated 11-clay. The 001 reflections are indicated with arrows and labeled with the corresponding d_{001}-spacing. The peak originating from ε-caprolactam is marked with an asterisk (*).

During melting of the monomer mix (cf. section 2.3), ε-caprolactam was intercalated into the clay galleries. This increased the average d_{001}-spacing of the clays up to around 1.8 nm for 11-Lp and 11-HT. 11-MMT and 11-Fh, on the other hand, increased to 2.1 and 3.8 nm, respectively (Figure 5). For all clays, except 11-Fh, the 001 reflection was broadened to such an extent that it was barely visible, most probably due to exfoliation and uneven amounts of intercalated molecules in the different galleries. 11-Fh, on the other hand displayed two 001 reflections, showing the existence of two main d-spacings. The spacing of 11-Fh was also increased up to a value almost twice as large as the other clays.

This is similar to what we observed in the studies of CTAB-modified clays for use in PS-clay nanocomposites see refs.[10,11]. Due to the larger surface charge on the Fh platelets, more surfactant was intercalated during surface treatment, and hence the clay could accept more ε-caprolactam between its platelets.

3.4 WAXS: N6NCs

Figure 6 shows WAXS curves of the four polymerized N6NCs. All samples showed a peak at around q = 8 nm^{-1} which originates from the 020 reflection of the γ-phase of nylon 6.[12] The absence of a 020 reflection in the curve from pure nylon 6 (inset in Figure 6) indicated that it crystallized only into the α-phase. This further shows that the resulting crystal structure of nylon 6 is highly sensitive to the additives.[13] After the polymerization had finished the samples were still kept above the melting temperature of pure nylon 6 (around 210 °C) for some time.

While the samples were cooled slowly down to room temperature, the polymer crystallized. Nylon 6 usually takes the α-phase when cooled down slowly, or annealed above 160 °C [14]. N6NCs on the other hand favor the γ-phase due to restricted movement of polymer chains caused by the exfoliated clay.[14]

N6Lp and N6HT both displayed a peak at q = 4 nm^{-1} (marked with a question mark) which corresponds to a d-spacing of around 1.6 nm. This peak could have been the lower order 010 reflection from the Nylon 6 γ-phase, but that is unlikely since it then should have been prominent also in

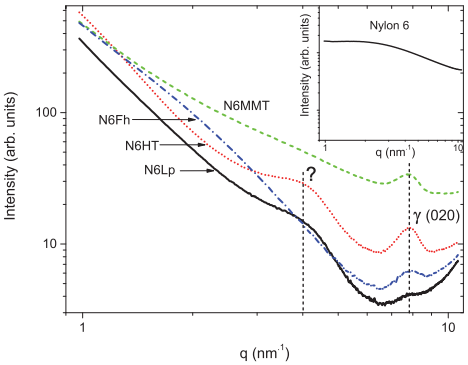

Figure 6 WAXS curves of polymerized N6NCs. The first peak at q~4 nm^{-1} is unknown (labeled "?") while the second peak at q~8 nm^{-1} comes from the 020 reflection of the nylon 6 γ-phase. Inset is the curve from pure nylon 6 synthesized in this work.

the curves from N6MMT and N6Fh. A more likely explanation is that the peak comes from the 001 reflection of the clay, which means that the d_{001}-spacing of the Lp and HT-clay shrinks during polymerization from around 1.8 to 1.6 nm. In the curves for N6MMT and N6Fh, on the other hand, the 001 reflection is absent, or outside of the q-range of the experiment, meaning that the average d_{001}-spacing was larger than ~6.3 nm due to substantial exfoliation and intercalation during polymerization.

These results seem to indicate that for preparation of well-exfoliated N6NCs it is beneficial to employ clay with large CEC because that leads to intercalation of large amounts of 11-acid molecules. Since the 11-acid surfactant is co-polymerized with nylon 6 this may create a driving force towards intercalation of more ε-caprolactam during polymerization, and eventually full exfoliation will take place. The lower CEC of Lp and HT leads to less amounts of 11-acid being intercalated during surface treatment compared to MMT and Fh (see the TGA-results above), and hence a smaller driving force for exfoliation is present.

3.5 X-ray computed μ-Tomography (XMT)

X-ray XMT was employed to investigate the dispersion of the 11-clays before and after polymerization. Figure 7 shows tomography images from the samples after melt-intercalation of ε-caprolactam. The images of the 11-Lp and 11-HT melts display large particles, an indication of low miscibility between these 11-clays and ε-caprolactam. No such features are visible in the melts of 11-MMT or 11-Fh (11-Fh is not shown here).

After polymerization the situation stayed the same, as can be seen in the tomography slices in Figure 8 and the 3D-rendering of N6HT in Figure 9.

The low-CEC composites (N6HT and N6Lp) contained a substantial amount of large particles while the other two composites had a particle size smaller than the resolution of

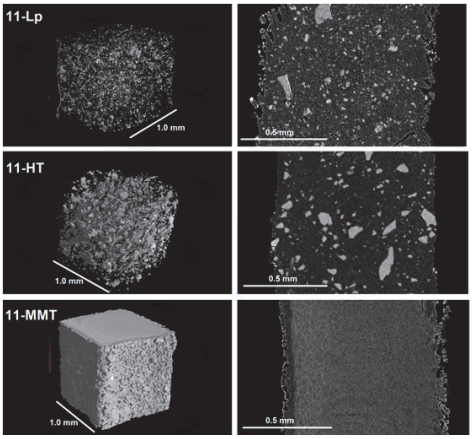

Figure 7 XMT images of three samples containing 11-clay dispersed in ε-caprolactam. From the top: 11-Lp, 11-HT and 11-MMT. The left pane shows a 3D rendering while the right pane shows a slice in the middle of the samples.

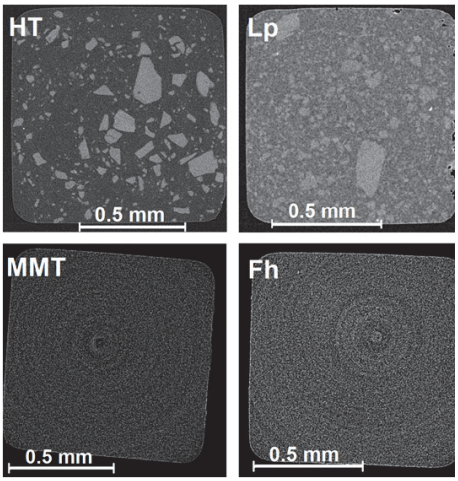

Figure 8 XMT slices of N6HT (top left), N6Lp (top right), N6MMT (bottom left) and N6Fh (bottom right). The speckled pattern and the circular features of N6MMT and N6Fh are not due to clay particles, but to noise and artifacts in the detector.

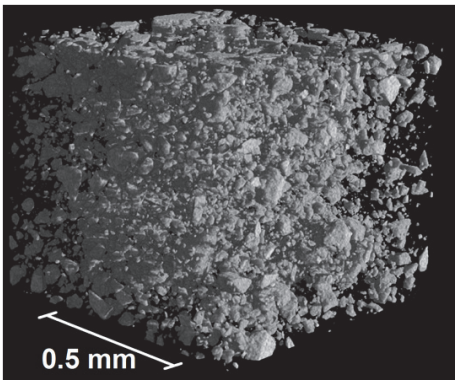

Figure 9 XMT 3D-rendering of N6HT displaying large clay particles/aggregates.

the instrument (0.9 μm). These observations corroborate our interpretation of the WAXS data concerning the decreasing d_{001}-spacing of the 11-Lp and 11-HT clays during polymerization. Due to the lower miscibility of these clays in ε-caprolactam they are unable to disperse to the same degree as 11-MMT and 11-Fh, which leads to segregation by shrinking to reduce the clay-nylon 6 interfacial area.

3.6 Mechanical properties

Figure 10 shows the resulting stress-strain curves from the four different N6NCs together with pure nylon 6 synthesized in this work. One particular feature of the curves is that they all display two slopes without the typical necking, characteristic for polystyrene-clay nanocomposites, when the material fails drastically. The reason for this is that nylon 6 is semi-crystalline and can thus deform to a large degree during compression. The first linear region of the curves is determined by the elasticity of the materials and is measured by the compressive modulus, $E_C = \sigma/\varepsilon$ (see Table 2) where σ and ε are the stress and the strain, respectively. For the curves shown here, this elastic region only spans up to around 5 % strain for the N6NCs and 9 % strain for the pure nylon 6, at which point the slope of the curves changes due to plastic deformation of the nylon 6-matrix. The yield strength and energy dissipation in this study (see Table 2) was defined by the stress at this point in the curves, and the product of the strain and stress at the same point, respectively.

As expected the N6NCs display much higher stiffness (compressive modulus) compared to pristine nylon 6 due to the reinforcing effect of the clay platelets.[2,15,16] Interestingly the values found here clearly shows a trend showing higher stiffness with a higher clay surface charge. N6Fh which has the highest CEC (120 meq/100g) for instance, has a 50 % larger modulus than N6Lp. The yield strength is also higher for the N6NCs, although N6Lp has a lower value than nylon 6. This property too follows the trend with larger values for samples with higher CEC. It is highly noteworthy that this trend is entirely opposite what was found for polystyrene-clay nanocomposites in presented in our earlier work.[10]

In our work on polystyrene-clay systems (PSNCs), the HT and Lp based nanocomposites displayed better properties than the MMT and Fh based ones, mainly due to increased dispersion of the clay particles compared to MMT and Fh. The increased dispersion was caused by the reduced electrostatic force holding the platelets together due to lower CEC, and this allowed for easier exfoliation.

Apparently the mechanism behind exfoliation in the N6NCs is different than for the PSNCs. We believe that the dispersion of 11-MMT and 11-Fh in nylon 6 was increased due to improved miscibility between clay and polymer. The reason for this may be that these two clay types intercalated more surfactant than HT and Lp, thus increasing the miscibility. The larger uptake of 11-acid during surface treatment, for the clays with higher CEC, was most likely just caused by the larger surface charge that these clays possess, which inherently must be balanced by a larger amount of 11-acid. Furthermore the proceeding melt-intercalation of ε-caprolactam resulted in larger swelling for 11-MMT and 11-Fh because these contained more 11-acid and were thus more miscible with the monomer. The larger d-spacing of these two 11-clays may also have contributed by allowing easier access for the monomer.

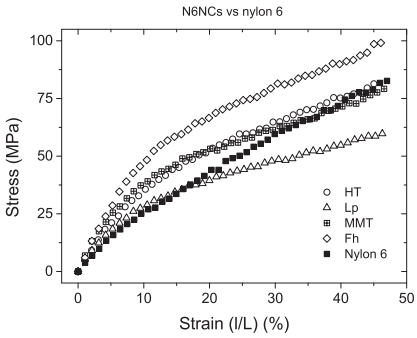

Figure 10 Stress-strain curves from compression testing of nylon 6 and nylon 6/clay nanocomposites.

Table 2 Yield strength, compressive modulus and fracture toughness of nylon 6 and nylon 6/clay nanocomposites with 5 wt.% 11-clay added.

Sample	Yield Strength (MPa)	Compressive modulus (MPa)	Strain at fail (%)	Energy dissipation (MJ/m^3)
Nylon 6	25.1	2.7	8.6	1.1
HT	26.4	4.3	5.9	0.8
Lp	22.0	3.8	4.8	0.5
MMT	26.9	5.5	4.8	0.6
Fh	30.6	5.8	5.2	0.8

4 CONCLUSIONS

A series of nylon 6/clay nanocomposites were prepared by melt intercalation of ε-caprolactam with subsequent polymerization using four different 2:1 clays with varying surface charge. The surface charge of each clay type had a pronounced effect on the degree of surface modification, clay dispersion, and the mechanical properties. The TGA-results showed that the uptake of surfactant followed a linear correlation to the surface charge, with larger uptake for the clays with larger surface charge (MMT and Fh). The higher uptake of surfactant for MMT and Fh led to greater miscibility between clay and monomer. This resulted in increased intercalation of monomer during melt-intercalation, and subsequently full exfoliation of the clay structures in the finished nylon 6/clay nanocomposites. The lower miscibility for 11-HT and 11-Lp caused these to segregate by growing into larger clay tactoids during polymerization. The mechanical properties of the nanocomposites reflect the degree of dispersion of the clays. For the exfoliated samples, N6MMT and N6Fh, the mechanical properties were significantly improved relative to pristine nylon 6. N6HT, on the other hand, displayed only small improvements, while N6Lp generally showed reduced properties. The stiffness of the nanocomposites was, however, increased in all cases.

ACKNOWLEDGEMENTS

This work was performed under the sponsorship of The Research Council of Norway. The authors acknowledge the beam time provided by MAX-Lab.

AUTHOR INFORMATION

Corresponding author

*E-mail: kenneth.knudsen@ife.no; henrik.mauroy@ife.no

REFERENCES

(1) Usuki, A.; Kojima, Y.; Kawasumi, M.; Okada, A.; Fukushima, Y.; Kurauchi, T.; Kamigaito, O. Synthesis of Nylon 6-Clay Hybrid. *J. Mater. Res.* **1993**, 8, 1179-1184.

(2) Kojima, Y.; Usuki, A.; Kawasumi, M.; Okada, A.; Fukushima, Y.; Kurauchi, T.; Kamigaito, O. Mechanical Properties of Nylon 6-Clay Hybrid. *J. Mater. Res.* **1993**, 8, 1185-1189.

(3) Okada, A.; Usuki, A. Twenty Years of Polymer-Clay Nanocomposites. *Macromol. Mater. Eng.* **2006**, 291, 1449-1476.

(4) Panwar, A.; Choudhary, V.; Sharma, D. K. A Review: Polystyrene/Clay Nanocomposites. *J. Reinf. Plast. Compos.* **2011**, 30, 446-459.

(5) Boylu, F.; Hojiyev, R.; Ersever, G.; Ulcay, Y.; Celik, M. S. Production of Ultrapure Bentonite Clays through Centrifugation Techniques. *Sep. Sci. Technol.* **2012**, 47, 842-849.

(6) Plivelic, T. S.; Labrador, A. L.; Theodor, K.; Gaponov, Y.; Svensson, C.; Nygaard, J.; Cerenius, Y. In *8th Nordic Workshop on Scattering from Soft Matter* Kjeller, Norway, 2011.

(7) Hammersley, A. P.; Svensson, S. O.; Hanfland, M.; Fitch, A. N.; Hausermann, D. Two-Dimensional Detector Software: From Real Detector to Idealised Image or Two-Theta Scan. *High Pressure Res.* **1996**, 14, 235-248.

(8) The Clay Minerals Society. Source Clay Physical/Chemical Data. http://www.clays.org/SOURCE%20CLAYS/SCdata.html Apr. 04 DateAccess. 2013

(9) Kaviratna, P. D.; Pinnavaia, T. J.; Schroeder, P. A. Dielectric Properties of Smectite Clays. *J. Phys. Chem. Solids* **1996**, 57, 1897-1906.

(10) Mauroy, H.; Plivelic, T. S.; Hansen, E. L.; Fossum, J. O.; Helgesen, G.; Knudsen, K. D. The Effect of Clay Surface Charge on the Emerging Properties of Polystyrene-Organoclay Nanocomposites. *Accepted August 2013 Journal of Physical Chemistry C* **2013**.

(11) Mauroy, H.; Plivelic, T. S.; Suuronen, J.-P.; Fossum, J. O.; Knudsen, K. D. Anisotropic Polystyrene-Clay Nanocomposites: Synthesis, Characterization and Mechanical Properties. *Manuscript in preparation (June)* **2013**.

(12) Konishi, Y.; Cakmak, M. Structural Hierarchy Developed in Injection Molding of Nylon 6/Clay/Carbon Black Nanocomposites. *Polymer* **2005**, 46, 4811-4826.

(13) Fornes, T. D.; Paul, D. R. Crystallization Behavior of Nylon 6 Nanocomposites. *Polymer* **2003**, 44, 3945-3961.

(14) Liu, X. H.; Wu, Q. J. Phase Transition in Nylon 6/Clay Nanocomposites on Annealing. *Polymer* **2002**, 43, 1933-1936.

(15) Lan, T.; Kaviratna, P. D.; Pinnavaia, T. J. On the Nature of Polyimide Clay Hybrid Composites. *Chem. Mater.* **1994**, 6, 573-575.

(16) Cho, J. W.; Paul, D. R. Nylon 6 Nanocomposites by Melt Compounding. *Polymer* **2001**, 42, 1083-1094.

V

DIPOLAR ORDERING OF CLAY PARTICLES IN VARIOUS CARRIER FLUIDS

ORDENAMIENTO DIPOLAR DE PARTÍCULAS DE ARCILLA EN DIVERSOS FLUIDOS

Z. Rozynek[a †], H. Mauroy[b], R. C. Castberg[c], K. D. Knudsen[b] and J. O. Fossum[a,d ‡]

a) Department of Physics, NTNU, Høgskoleringen 5, NO-7491 Trondheim, Norway, rozynek@ntnu.no†, jon.fossum@ntnu.no‡
b) Physics Department, IFE, NO-2027 Kjeller, Norway
c) Department of Physics, University of Oslo, P.O.Box 1048, NO-0316 Oslo, Norway
d) Centre for Advanced Study at the Norwegian Academy of Science and Letters, Drammensveien 78, NO-0271 Oslo, Norway
†, ‡ corresponding authors

We investigate here examples of complexity in composite materials. The objective of the paper is to show that clay particles can be aligned in different hosting media, such as: silicone oil, paraffin-wax, polystyrene and ambient air. The use of an electric field is an easily controllable, non-intrusive manner of inducing such an alignment. Depending on the medium used, a large span in time constants for the orientation and reorganization has been observed. Furthermore, the reorientation may be frozen into the material, thus permanently changing its properties.

Se investigan ejemplos de complejidad en materiales compuestos. El objetivo de este artículo es demostrar que se pueden alinear partículas de arcilla en diferentes medios como aceite de silicona, parafina-cera, poliestireno, y aire. El uso de un campo eléctrico resulta una vía fácilmente controlable y no-intrusiva de inducir el alineamiento. Se observa un amplio rango de constantes de tiempo para la orientación y la reorganización en dependencia del medio utilizado. Aún más, la reorientación puede congelarse en el material, de tal suerte que sus propiedades cambian permanentemente.

PACS: Granular materials rheology, 83.80.Fg; pattern formation in granular systems, 45.70.Qj; rocks magnetic and electrical properties, 91.25.F-; colloids, 82.70.Dd

INTRODUCTION

Application of an external electric field to a suspension of dielectric clay particles induces polarization of the particles. They will consequently re-orient and aggregate, and this results in the formation of a columnar structure parallel to the electric field direction. The clay particles polarize along their silica sheets, i.e. their stacking direction will be normal to the direction of polarization [1]. The mechanism of the polarization in clays is still under discussion, although one hypothesis is that the intercalated ions and water molecules, which are movable, could play a central role in particle electrical polarization. The resulting induced dipole is attached structurally to the clay particle, and this causes clay particles to reorient and interact, as suggested in [1]. However, recent measurements performed by us indicate that the contribution from the outer surface charges may be dominant, and the particle alignment is then determined by its shape, i.e. so that the longest axis of a single clay particle (or aggregate of particles) will be parallel to the direction of *E*-field lines [2].

The clay polarization is a rapid process ($< \mu s$) that is followed by a particle re-orientation with a rotation time proportional to the carrier fluid viscosity and inversely proportional to: firstly the difference in the dielectric constants between particle and medium; and secondly the electric field squared (see also [3]). The time scale for particle rotation is in the range of 10^{-3} to 10^{1} *s*, for *E*-field between 50 and 2000 *V/mm* and viscosity of carrier fluid such as silicone oil between 100 and 500 *mPa·s* [2]. If the particle concentration is high enough, and a minimum critical *E*-field is applied, chain formation occurs via a particle dipole-dipole interaction [4].

The phenomena described above may be utilized in many different ways and just a few examples are: (i) Electro-rheological fluids (clay particles in silicone oil) in which the so-called liquid-to-solid reversible transition occurs via the application of an external *E*-field. Such a transition is manifested by changes of ER properties, namely: viscosity, yield stress, storage and loss moduli, etc. [5, 6, 7]. Some examples of application of ER fluids are: fast acting hydraulic valves or clutches [8]. (ii) Nanocomposites (clay particles in polymers), since the aspect ratio of the clay platelets and the interfacial contact area between the clay and matrix are high, the incorporation of small amounts of such inorganic filler into a polymer medium can significantly improve the properties of the resulting polymer/clay nanocomposites. Such nanocomposites can attain a high degree of stiffness and strength [9]. Furthermore, the presence of the dispersed phase results in additional properties, such as flame retardancy or enhanced barrier properties (e.g. gas permeability), when compared to either component [10, 11]. In many situations it is not only the *presence* of the well-dispersed filler but also its *orientational* ordering that may improve certain physical and

chemical properties. The electric-field-induced alignment of clay particles can thus be used to obtain and control a range of the desired material properties.

The above examples have clearly an application-oriented character. However, the focus of our studies is on better understanding of basic physics of such complex systems. Apart from already mentioned hosting media, we also here report for the first time structuring from clays in atmospheric air. The common denominator, for all studied systems, is the clay particle alignment in the presence of an *E*-field.

SAMPLES

Two types of clay particles, namely laponite (Lp) and fluorohectorite (Fh) are used in the present investigations. The synthetic Lp clay was purchased from Laponite Inc. and the synthetic Fh clay was purchased from Corning Inc. They both belong to the smectite family of clay minerals. Smectites are 2:1 phyllosilicates that possess a net negative charge on the surface of each crystalline layer. Counter ions are located between these lamellar sheets to balance for that charge. Exchangeable cations such as Na^+, Li^+, Ca^{2+}, Mg^{2+}, Cu^{2+} or Fe^{2+} are common. The chemical formulas are: $Na^+_{0.7}[(Mg_{5.5}Li_{0.3})Si_8O_{20}(OH)_4]^{0.7-}$ for Lp clay and $Na^+_{1.2}[(Mg_{4.8}Li_{1.2})F_4Si_8O_{20}]^{1.2-}$ for Fh clay, respectively. They are silicates where a fraction of Mg^{2+} ions is substituted by Li^+ in trioctahedral sites resulting in a negative structural charge [12]. Fluorohectorite has been reported from X-ray data to retain a stacked structure of lamellar particles composed of between 20 and 100 unit layers when dispersed in water, whereas laponite is known to exfoliate into single unit layers in aqueous suspensions [13]. The individual Lp clay particle resembles a disc of average diameter around 30 *nm*, whereas the size of Fh clay can be as large as several *μm*.

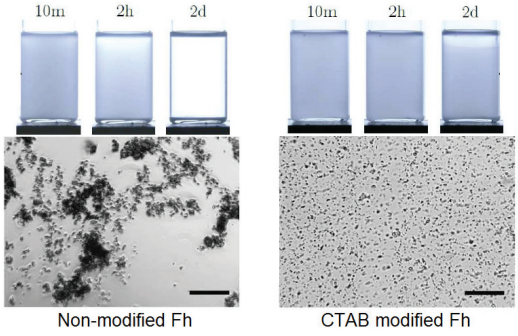

Figure 1: Microscope images of non-modified Fh (left) and organically modified CTAB-Fh (right) clay particles suspended in silicone oil. The length of the bar corresponds to 200 *μm*. The pictures of the glass vials with samples (top) illustrate the sedimentation dynamics. Adopted from [16].

Clays, in their natural forms, are hydrophilic, or depending on the context they may be referred to as organophobic. When suspended in a non-polar medium, such as silicone oil or polymeric matrix, they tend to form large agglomerates and consequently sediment (see Figure 1). Addition of surfactants is commonly used to prevent particle agglomeration, which then slows down particle sedimentation, or if the particles are small enough (i.e. magnetic particles in ferrofluids), ensures that they are held in suspension by Brownian motions [14]. Another reason for modifying clays is the ease of uniform dispersion in an apolar polymer matrix. To promote compatibility between the inorganic filler and apolar polymers, it is necessary to chemically modify the inorganic clays by intercalation of organophilic cations, which expand the interlamellar space of the clay, decreasing the interaction among the silicate sheets, and facilitating the diffusion and accommodation of polymeric chains [15].

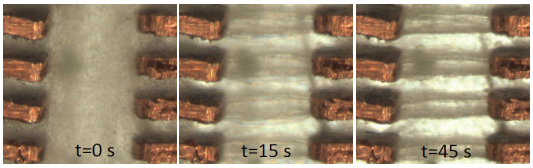

Figure 2: Optical microscopy images of clay/oil suspension without *E*-field applied (left) and a field of 1000 *V/mm* (middle and right).

RESULTS

Clays in silicone oil. The preparation of the ER fluid was undertaken by the following procedure. Na-Fh clay powder was crushed with a pestle and mortar, weighed and placed in an oven for 12 *h* at 110 *ºC*. The silicone oil was heated at the same conditions. Subsequently, the clay powder and silicone oil were mixed in glass tubes and sealed. The solutions were then vigorously hand-shaken for 2 *min* and placed in an ultrasonic bath for 1 *h*. Before each measurement the samples were hand-shaken again. The clay concentration was approximately 5 *wt.*%.

Firstly, optical observations were conducted. For that purpose the ER fluid was placed between two electrodes with pre-defined shapes as shown in Figure 2. The gap between the electrodes is roughly 1 *mm* and the electric field is applied horizontally.

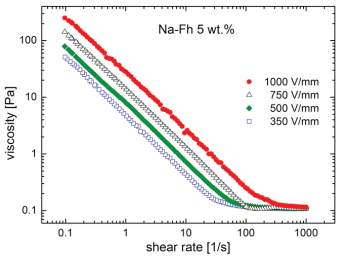

Figure 3: Flow curves for 5 *wt.*% clay particles suspended in silicone oil. Different electric field strengths are used, influencing the shear viscosity.

When no *E*-field is applied, the Fh particles are randomly dispersed into the silicone oil, as shown in Figure 2 (left). Microscopy images of the sample under a DC electric field of 1000 *V/mm* taken at different times, 15 *s* and 45 *s* are shown

in Figure 2 (middle and right). The formation of column-like structures aligning parallel to the field is clearly observed. Several thin chains are formed first, and these subsequently attract each other resulting in the creation of thicker columns. After a certain time (here several minutes) no major changes in the system are noticeable.

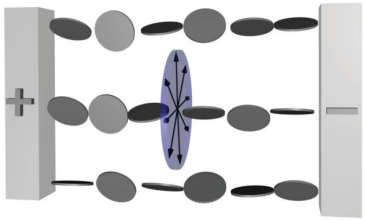

Figure 4: The sketch of the clay alignment in so-called anti-nematic configuration (see text for details).

Imagine now shearing the ER fluid perpendicular to the *E*-field direction. If the *E*-field is not present, the shear viscosity of such a sample (silicone oil and only 5 *wt.*% of clay) is close that of pure silicone oil. However, once the electric field is applied, so that the particles are oriented against the flow, the shear viscosity of a fluid containing clay particles is expected to increase. As the curves in Figure 3 show, this is also what is seen experimentally.

Clays in paraffin-wax. The particular type of paraffin-wax used here has its melting point around 65 *°C* and was chosen for two major reasons: (i) optimal melting and crystallization temperatures, providing both easy composite preparation and appropriate stiffness of the composite when in solid form at room temperature; (ii) a relatively non-polar and non-conductive material that can be used as an electrorheological carrier fluid when in the melted state. Fluorohectorite particles (~5 *wt.*%) were dispersed in the melted paraffin and then poured into a custom-made mould with two electrodes. The electric field strength of 500 *V/mm* was applied and kept for a few minutes until the paraffin crystallized and cooled down to room temperature. The solid composite was then investigated using wide-angle X-ray scattering.

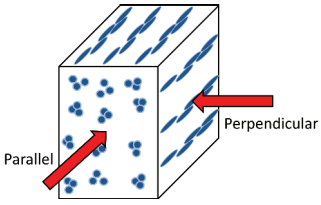

Figure 5: Simple sketch of what the X-ray beam probes in the sample.

When a 2-D X-ray pattern (like those shown in Figure 6) is integrated along the radial direction with a narrow *q*-range (2θ-angle) around the Bragg ring, one obtains a 1-D azimuthal plot which is then fitted using a parametric function. The fitting allows extracting parameters that are further used to calculate the nematic order parameter (S_2) (for details see [17]). This parameter ranges from -1/2 to 1, where 1 indicates perfectly oriented particles in the nematic configuration, 0 means no orientational order, and finally -1/2 indicates perfectly oriented particles in the anti-nematic configuration [6, 17, 18]. It is expected that the clay particles align in the anti-nematic geometry and the validity of such assumption is tested below.

Several 2-D X-ray images were taken from the same sample at different polar angles, with the rotation axis parallel to the reference direction, which is here the direction of the *E*-field. The nematic order parameter was calculated for four sample positions and the results are presented in Table 1.

Table 1.
Nematic order parameter as a function of the polar angle, with the rotation axis parallel to the direction of *E*-field lines.

Sample rotation	0	30	60	90	Avg
Order parameter	-0.37 ±0.01	-0.35 ±0.01	-0.37 ±0.02	-0.36 ±0.01	-0.36 ±0.01

We observe that the nematic order parameters do not differ significantly from each other indicating that there is no preferential orientation along the polar angle. The arrowed disc shown in Figure 4 represents the plane perpendicular to the *E*-field direction, and that is in fact the average particle stacking direction. The black arrows indicate that clay normals are oriented without any preferred polar direction.

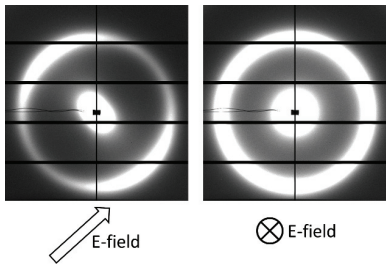

Figure 6: SAXS-patterns from PS/CTAB-Fh with permanently aligned clay chains. Remark: the sample is tilted 45 degrees in the *x-y* plane.

Clays in polystyrene. When aligning clay particles in liquid media the alignment may be lost after a while when the electric field is turned off. An approach to freeze the chain structure was tested by solidifying the matrix while the electric field was applied. The matrix, styrene monomer, polymerizes to give solid polystyrene polymer (PS). A 1 *wt.*% sample of organically modified CTAB-Fh (see [16] for details) was dispersed in styrene monomer and a small quantity of a radical initiator, benzoyl peroxide, was added. The clay/monomer suspension was filled in square shaped glass capillaries, which were sealed with a flame torch. The capillaries were then immersed in an 80 *°C* silicone oil bath, and placed between two plate electrodes. The electric field over the electrodes was set to 830 *V/mm*, and the samples were left to polymerize for 7 days. The resulting PS-clay composites were investigated with small angle X-ray scattering (SAXS) at the Dubble beam line at ESRF in Grenoble, France. The samples were probed with the X-ray beam perpendicular and parallel to the direction of clay chains

(see Figure 5). The main ring comes from the characteristic spacing between clay crystalline sheets, and d_{001}~4 *nm*. A pronounced anisotropy of the d_{001} peak is seen in Figure 6 (left) due to clay alignment, i.e. on average, particles orient with their stacking direction perpendicular to the *E*-field lines. When probed along the chains the pattern looks isotropic, as shown in Figure 6 (right), since there is no preferential orientation of clay particles along the polar angle (see also [18, 19]).

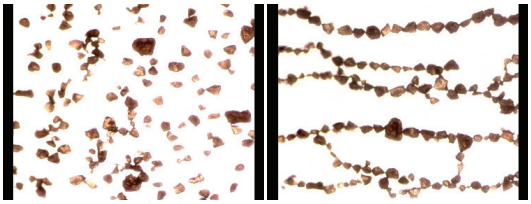

Figure 7: Laponite particle aggregates between two electrodes without *E*-field applied (left) and with an AC *E*-field of 500 *V/mm* (right). The images have been edited to enhance the contrast.

Clays in air. As the final example, we show laponite clay alignment in atmospheric air. Laponite clay powder stored in our laboratory at ~23 *ºC* and RH in range between 10 and 30 % was used. Such particles normally form aggregates and their sizes can span a few orders of magnitudes reaching a few *mm*. In the present work the size of the aggregates were between 10 and 100 *μm*. Figure 7 shows clay particle aggregates between two electrodes with no *E*-field applied (left) and with an AC *E*-field of 500 *V/mm* (right). The electrodes were kept horizontally and images were taken from above. Clay particles lied on a thin glass substrate, and when the electric field was applied the set-up was gently tapped, lowering the friction as the particles were momentarily suspended in air.

As can be seen, most of the clay particle aggregates align with their longest axis along the *E*-field direction. However, there are several particles disobeying that rule, and these making bridges between individual chains allowing for charge transport. It is possible that the dominant part of the clay polarization occurs only on the clay aggregate surface, not the bulk, i.e. in the clay galleries. However, it is difficult (if not impossible) to draw a firm conclusion on this point, since we deal here with large aggregates. Therefore our future work will be focused on reducing the complexity of the system by working with *single* clay particles, such as vermiculite.

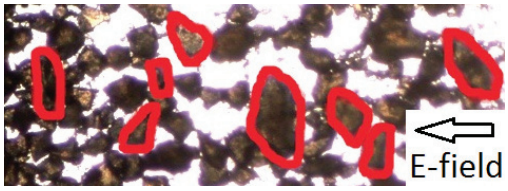

Figure 8: High concentration of laponite particle aggregates between two electrodes with an AC *E*-field of 500 *V/mm* applied. Several particle aggregates (red-color-marked) were not able to re-orient fully with their longest axis along the *E*-field lines due to jamming. This will effectively lower the value of the nematic order parameter.

In Figure 8 we also present structuring from particles in air, but this time the clay concentration is significantly higher. A possible jamming transition may occur where many particles have very little freedom to re-orient (see red-coloured particles). This is an ongoing study and more results are expected in the near future.

CONCLUSION

We have provided examples of recent results from our work on manipulation and orientation of asymmetric particles in external fields. Clay particles are ideal for this purpose due to their inherent large anisotropy and correspondingly high degree of polarizability. When placed in an apolar medium and subjected to an electric field, the particles will orient and organize within a time frame that depends principally on factors such as *E*-field strength and viscosity of the surrounding medium. We have shown how these effects may be induced in various media, with a large span in viscosity, from silicone oil, via polymer matrices to solidified wax, and even air. The clay particles may form chains that span the entire sample volume, thus changing the macroscopic properties of the material. Most notably, there will generally be a large change in the overall rheological behavior, and materials of this kind are therefore highly interesting for applications where the mechanical and structural properties should be manipulated via an electric field.

ACKNOWLEDGEMENTS

This work was supported by the Research Council of Norway through the Programs: NANOMAT project number 182075, and FRINAT project number 171300.

[1] J. O. Fossum, Y. Méheust, K. P. S. Parmar, K. D. Knudsen, K. J. Måløy and D. M. Fonseca, Europhys. Lett. **74**, 438 (2006).
[2] R. C. Castberg, Z. Rozynek, J. O. Fossum, K. J. Måløy and P. Dommersnes, work in progress
[3] R. C. Castberg, Z. Rozynek, J. O. Fossum, K. J. Måløy, P. Dommersnes and E. G. Flekkøy, Rev. Cub. Fis. **29**, 1E17 (2012).
[4] J. D. Jackson, *Classical Electrodynamics*, (Wiley 143, 1962).
[5] B. Wang, M. Zhou, Z. Rozynek and J. O. Fossum, J. Mater. Chem. **19**, 1816 (2009).
[6] Z. Rozynek, K. D. Knudsen, J. O. Fossum, Y. Méheust and B. Wang, J. Phys: Condens. Matter. **22**, 324104 (2010).
[7] Y. Méheust, K. Parmar, B. Schjelderupsen and J. O. Fossum, J. Rheol. **55**, 809 (2011).
[8] J. Madeja, Z. Kesy and A. Kesy, Smart Mater Struct. **20**, 105005 (2011).
[9] A. Esteves, A. Timmons and T. Trindade, Quim. Nova **27**, 798 (2004).
[10] S. S. Ray and M. Okamoto, Prog. Polym. Sci. **28**, 1539

(2003).
[11] S. Letaief and C. Detellier, J. Mater Chem. **17**, 1476 (2007).
[12] P. D. Kaviratna, T. J. Pinnavaia and P. Schroeder, J. Phys. Chem. Solids **57**, 1897 (1996).
[13] E. DiMasi, J. O. Fossum, T. Gog and C. Venkataraman, Phys. Rev. E **64**, 061704 (2001).
[14] Z. Rozynek, A. Jozefczak, K. D. Knudsen, A. Skumiel, T. Hornowski, J. O. Fossum, M. Timko, P. Kopecansky and M. Koneracka, Eur. Phys. J. E **34**, 28 (2011).
[15] K. S. Santos, S. A. Liberman, M. A. S. Oviedo and R. S. Mauler, J. Polym. Sci. B: Polym. Phys. **46**, 2519 (2008).
[16] Z. Rozynek, B. X. Wang, J. O. Fossum and K. D. Knudsen, Eur. Phys. J. E **35**, 9 (2012).
[17] Y. Méheust, K. D. Knudsen and J. O. Fossum, J. Appl. Cryst. **39**, 661 (2006).
[18] I. Dozov, E. Paineau, P. Davidson, K. Antonova, C. Baravian, I. Bihannic and L. J. Michot, J. Phys. Chem. B **115**, 7751 (2011).
[19] Z. Rozynek, R. C. Castberg, A. Mikkelsen and J. O. Fossum, work in progress.

VI

VII

Soft Matter

Cite this: *Soft Matter*, 2012, **8**, 11514

www.rsc.org/softmatter

PAPER

Complex coacervate micelles formed by a C18-capped cationic triblock thermoresponsive copolymer interacting with SDS†

Wei Wang,[a] Henrik Mauroy,[b] Kaizheng Zhu,[c] Kenneth D. Knudsen,[b] Anna-Lena Kjøniksen,[ac] Bo Nyström*[c] and Sverre Arne Sande[a]

Received 5th July 2012, Accepted 5th September 2012
DOI: 10.1039/c2sm26567b

We report on a new route for creating multi-component micelles employing a specifically designed triblock copolymer, $C_{18}PEG_{10}$-*block*-$NIPAAM_{54}$-*block*-$(AMPTMA(+))_{16}$, combining hydrophobic and hydrophilic segments as well as a polyelectrolyte end block. By interaction with an oppositely charged surfactant (SDS), the block copolymer will co-assemble with SDS creating a core–shell particle with the *core* formed by the alkane chain together with densely packed surfactant micelles that are kept in place by the polyelectrolyte block. In order to maintain a stable particle, the *corona* of the structure is constructed by bent hydrophilic/neutral segments of the block copolymer. Turbidimetry and zeta-potential measurements were used to elucidate interactions with SDS and to measure the stability of the co-assembled structure, whereas small-angle neutron scattering and dynamic light scattering were used to identify structural details of these particles.

Introduction

Polymer–surfactant systems have received public attention due to their wide range of use in various fields, such as in oil recovery, paints, and cosmetic products.[1,2] In these systems surfactants are used to decrease the surface tension, while the incorporation of polymers can assist in modifying the viscosity of the products. The *mixture* of a polymer and surfactant usually behaves very differently from the individual components. Two main categories of phase behavior, associative and segregative, are commonly found in such cases.[3] The interaction within oppositely charged polymer–surfactant systems is generally associative, driven by the columbic attraction and the entropy gain through counterion release.[4] In dilute solutions, this interaction may lead to a phase separation at the stoichiometric point, where the association complex of the polymer and the surfactant tends to separate from the water phase and forms a precipitate. However, for diblock copolymers composed of a polyelectrolyte block and a sufficiently hydrophilic neutral block, a macroscopic phase separation will generally not occur even if the charges on the copolymer are neutralized.[5,6] This is because the interaction between the polyelectrolyte block and charged surfactant can form a core–shell particle where the polyelectrolyte and the surfactant form the core, with the structure being stabilized by the neutral block as a corona. Using a diblock copolymer with a neutral and an anionic block together with an oppositely charged homopolyelectrolyte, Hofs *et al.*[7] reported the formation of complex core–shell structures, with the size increasing with the amount of polyelectrolyte present. This is one example of a co-assembled structure that has recently been named complex coacervate core micelles (C3Ms). Alternatively they may be referred to as polyion or block ionomer complexes, depending on the context. Basically, this is a micelle-like structure formed by the interaction between a block copolymer and another oppositely charged chemical species.[8–13]

Despite their interesting association properties in aqueous environments, the application of charged materials in drug delivery is limited because of their generally poor biocompatibility. However, complex coacervate core micelles provide a possibility to employ charged polymers in this field since the charges on the polymer become neutralized and hidden in the core and are covered by the neutral, preferably biocompatible segments of the copolymer. In addition, the corona contributes to a thermodynamical stabilization of the complex. The size and structure of these C3Ms is an important parameter as it may have effect on the bio-distribution, as well as the efficacy and safety.[7] Since the core of C3Ms is formed by the interaction between the polyelectrolyte block of the copolymer and the oppositely charged species, the size of the core may be modified by changing, *e.g.*, the length of the polyelectrolyte block on the copolymer. Furthermore, the combination of diblock copolymers and surfactants can produce a highly organized structure in the core because of the micelles formed by the surfactants. Berret *et al.* have combined neutron-scattering data with modeling to

[a]*Department of Pharmaceutics, School of Pharmacy, University of Oslo, P. O. Box 1068, Blindern, N-0316, Oslo, Norway*
[b]*Department of Physics, Institute for Energy Technology, P. O. Box 40, N-2027, Kjeller, Norway*
[c]*Department of Chemistry, University of Oslo, P. O. Box 1033, Blindern, N-0315, Oslo, Norway*

† Electronic supplementary information (ESI) available. See DOI: 10.1039/c2sm26567b

interpret the structure of the *core* of such a system, which is composed of the dense micelles formed by surfactants and dressed by the polyelectrolyte block.[5,6,14,15]

The structures of the *corona* of C3Ms and micelles formed by diblock copolymers are similar, thus the size of the corona may be changed by changing the length of the neutral block in the copolymer or by using different chemical structures. Interesting structures have been observed by applying a triblock copolymer with the same polyelectrolyte block at both ends and a neutral block in the middle.[16] When the polyelectrolyte block was adsorbed onto Pt nanoparticles, it formed a flower-like structure. This type of structure has also been proposed as one of the many possible aggregates of triblock amphiphiles of the type $C_nEO_mC_{n*}$.[17] In dilute aqueous solution, the flower-like micelles formed by the $C_nEO_mC_{n*}$ class require a sufficient length of the alkane chain and EO segments because the energy that is gained from moving the hydrophobic chain to the core of the micelles should be able to compensate for the entropy loss of the middle block due to bending. Therefore, the $C_nEO_mC_{n*}$ segment for such systems generally has a longer EO chain than the alkane chains.

In this work, a new approach is presented to achieve multi-component micellar structures by combining the route reported in the literature for making C3Ms with the independent procedure described above for creating flower-like micelles (employing $C_nEO_mC_n$). For this purpose, a C18 end-capped triblock copolymer was designed and synthesized by using atom transfer radical polymerization (ATRP). At one side of the block copolymer the alkane chain was replaced by cationic poly((3-acrylamidopropyl)-trimethylammonium chloride) (PAMPTMA). By mixing this with an oppositely charged surfactant, the charges on the block copolymer can be neutralized. This neutralized aggregate is hydrophobic, and will thus tend to aggregate in the core of the micelles together with the alkane chains. Between the PEO and PAMPTMA chains, a thermo-responsive block poly(*N*-isopropylacrylamide) (PNIPAAM) was introduced. This copolymer undergoes thermally induced deswelling when the solution temperature is raised above the lower critical solutions temperature (LCST for aqueous solutions of PNIPAAM is approximately 32 °C (ref. 18)). At temperatures well below the LCST, PNIPAAM is generally solvated owing to hydrogen bonding between water molecules and the amide residues of the polymer chains. This hydrogen bonding with water is increasingly disrupted on heating. It is therefore of interest to also look at temperature effects on the structure of the particles created.

In the nomenclature introduced by Voets *et al.*,[8] this type of block copolymers would correspond to an S-*b*-S-*b*-C structure, where S is a soluble and C is a cationic block. However, we employ in addition an alkane chain (C18) at one end, and the second S block shows a temperature-dependent hydrophobicity. Most studies of such systems have so far been focused on diblock copolymers. C3Ms have not been well-studied for triblock copolymer systems, and the particular combination used here, with an end-capped water insoluble block, is a novel aspect of this study.

The combination of small-angle neutron scattering (SANS) and dynamic light scattering (DLS), two of the techniques employed in this work, is very useful to elucidate the structure of the system, since SANS will generally probe the core of the particles, whereas DLS is sensitive to the overall size, including the corona.

Materials and methods

Materials

Poly(ethylene glycol) octadecyl ether (Brij®S10, M_n values of 711), 2-bromoisobutyl bromide and copper(II) chloride were purchased from Sigma-Aldrich and employed as received. *N*-isopropylacrylamide (NIPAAM, Acros) was recrystallized from a toluene–*n*-hexane mixture and dried under vacuum before use. The charged monomer (3-acrylamidopropyl)-trimethylammonium chloride, abbreviated as AMPTMA (75 wt% in H_2O, Aldrich), was purified from the trace inhibitor present in the sample by precipitating into cold acetone, followed by washing with cold acetone and finally drying under vacuum overnight. Triethylamine (TEA) was dried over anhydrous magnesium sulfate, filtered, distilled under N_2 and stored over 4 Å molecular sieves. Copper(I) chloride from Aldrich was washed with glacial acetic acid, followed by washing with methanol and diethyl ether and then dried under vacuum and kept under N_2 atmosphere. *N*,*N*,*N*′,*N*″,*N*‴,*N*⁗-(Hexamethyl triethylene tetramine) (Me_6TREN) was synthesized according to a previous description in the literature.[19] All water used in this study was purified with a Millipore Mill-Q system and the resistivity was approximately 18 MΩ cm.

Synthesis of the octadecyl-capped PEG initiator (C_{18}–PEG–Br)

The octadecyl-capped PEG macroinitiator (C_{18}–PEG–Br) was prepared by reacting poly(ethylene glycol) octadecyl ether (C_{18}–PEG–OH) with 2-bromoisobutyl bromide in the presence of triethylamine as outlined in Scheme 1.[20,21] The ^{1}H-NMR spectrum indicated that the degree of esterification was at least 99%. ^{1}H NMR (300 MHz, $CDCl_3$): $\delta = 0.72$ (t, 3H, CH_3–CH_2–), 1.12 (m, 30H, –$(CH_2)_{15}$–), 1.43 (m, 2H, $CH_3(CH_2)_{15}CH_2CH_2O$–), 1.8 (s, –$COC(CH_3)_2Br$), 3.3 (m, 2H, $CH_3(CH_2)_{16}CH_2O$–), 3.50 (m, 36H, –O–$(CH_2CH_2)_9$–O–CH_2CH_2O–), 3.58 (m, 2H, –O–$(CH_2CH_2)_9$–O–CH_2CH_2O–, 4.16 (m, 2H, –O–$(CH_2CH_2)_9$–O–CH_2CH_2O–); ^{13}C NMR (75 MHz, $CDCl_3$): $\delta = 171$ (C=O), 71–66 (–O–$(CH_2CH_2)_n$–O), 65 (–$OCH_2(CH_2)_{16}CH_3$), 56 (–$C(CH_3)_2Br$), 32 (–$C(CH_3)_2Br$), 22–30 (–$OCH_2(CH_2)_{16}CH_3$), 14 (–$O(CH_2)_{17}CH_3$).

The number of repeating units of the ethylene glycol (EG) in the PEG polymer was recalculated according to its proton NMR spectrum of the fully esterification product based on a simple formula: $n = (3I_a/2I_b)$, where I_a is the corresponding integral area of the methenyl group of EG (–O–CH_2CH_2–) at 3.7 ppm and I_b is the integral area of the end-capped methyl group (–$C(CH_3)_2Br$, 6H) at 1.8 ppm. The repeating units of EG are estimated to be 10 for Brij®S10, and it is denoted as C_{18}–PEG_{10}.[21]

Synthesis of the triblock copolymers

The triblock copolymer was prepared *via* a simple 'one-pot' two step ATRP procedure (Scheme 1).[21–24] Briefly, the polymerization was performed in a water–DMF (40 : 60, v/v) mixture solvent at 25 °C, and the initiator–catalyst system in the mixture contained a PEG derivative macroinitiator (C_{18}–PEG_{10}–MI),

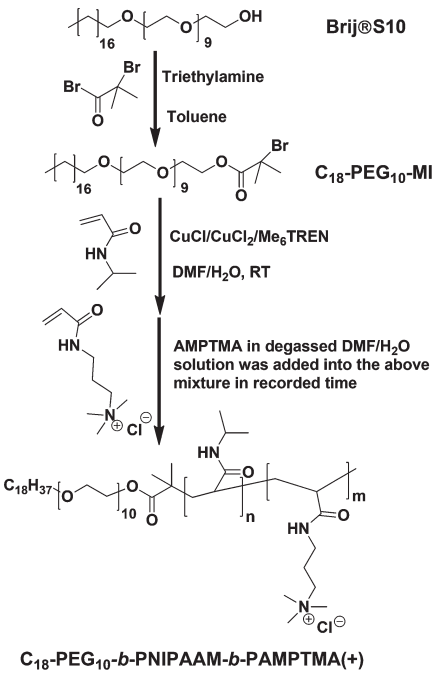

Scheme 1 Synthetic route for the preparation of C_{18} end-capped triblock copolymer C_{18}–PEG_{10}-*b*-P(NIPAAM)$_{54}$-*b*-P(AMPTMA(+))$_{16}$, *via* the 'one-pot' ATRP procedure.

CuCl, $CuCl_2$ and Me_6TREN (with molar feed ratio ([NIPAAM] = 2 M, [NIPAAM]/[AMPTMA]/[C_{18}–PEG_{10}–MI]/[CuCl]/[$CuCl_2$]/[Me_6TREN] = 60/30/1/1/0.6/1.6). The preparation and purification procedure of the polymer was conducted under similar conditions as described in detail previously.[21,24,25]

The chemical structure and composition of the triblock copolymer was also ascertained by its ^{1}H NMR spectra (Fig. 1). The number-average molecular weight and the unit numbers of *o*, *n* and *m* in C_{18}–P(EG)$_o$-*b*-P(NIPAAM)$_n$-*b*-P(AMPTMA)$_m$ were evaluated by comparing the integral area of the methyne proton (number **8** in Fig. 1) of PNIPAAM (δ = 3.85 ppm, –C*H*(CH$_3$)$_2$, I_a), the methyl group of AMPTMA (number **15** in Fig. 1) (δ = 3.10 ppm, –N(C*H*$_3$)$_3$, I_b), and the typical peak of the methenyl proton of EG (number **4** in Fig. 1) (δ = 3.70 ppm, –OC*H*$_2$C*H*$_2$O–, I_c) based on a simple equation: $m_{(NIPAAM)} = o4(I_a/I_c)$; $n_{(AMPTMA)} = o(4I_b/9I_c)$. The composition of the triblock copolymer is estimated to be: *o*/*m*/*n* = 10/54/16, *i.e.* C_{18}–PEG_{10}-*b*-P(NIPAAM)$_{54}$-*b*-P(AMPTMA(+))$_{16}$, based on our previous calculation results that the number of repeating units of the ethylene glycol of C_{18}–PEG–MI is 10.

Asymmetric flow field-flow fractionation

The asymmetric flow field-flow fractionation (AFFFF) measurements were carried out on an AF2000 FOCUS system (Postnova Analytics, Landsberg, Germany) equipped with an RI detector (PN3140, Postnova) and a multiangle (7 detectors in the range 35–145°) light scattering detector (PN3070, λ = 635 nm, Postnova). The sample (0.5 wt% in 0.1 M NaCl) was measured at 10 °C using a 350 μm spacer, a regenerated cellulose membrane with a cut-off of 5000 (Z-MEM-AQU-426N, Postnova), and an

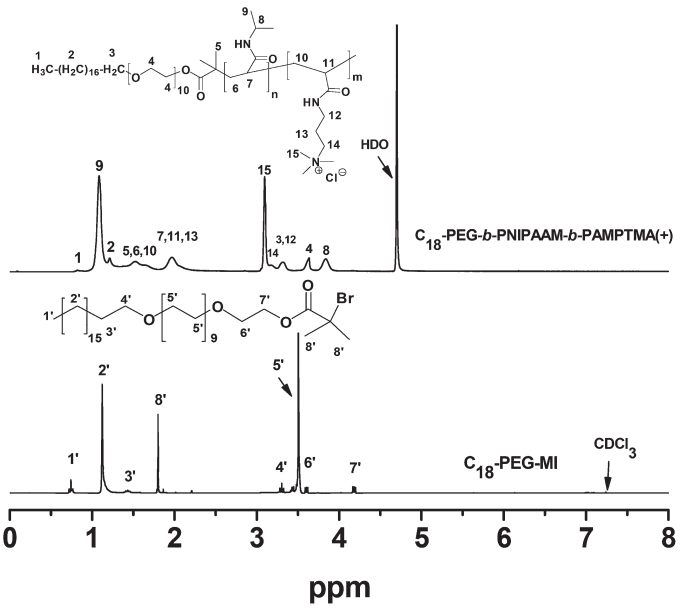

Fig. 1 ^{1}H NMR spectra of the octadecyl-capped PEG initiator (lower spectrum, $CDCl_3$-d as solvent, 300 MHz) and the triblock copolymer C_{18}-PEG-*b*-PNIPAAM-*b*-PAMPTMA(+) (upper spectrum, D_2O as solvent, 300 MHz).

injection volume of 20 μL. In the experiments a constant detector flow rate of 0.3 mL min^{-1} and a slot pump flow rate of 1.5 mL min^{-1} were used. The focusing time was 10 min at a cross-flow of 2.0 mL min^{-1}. The cross-flow was then linearly reduced to zero during a period of time of 7 min. Processing of the measured data was achieved by the Postnova software (AF2000 Control, version 1.1.011). The molecular weight and polydispersity of the sample (Fig. 2) were determined using this software with a Zimm-type fit. The molecular weight measured by AFFFF (4.1×10^4 g mol^{-1}) is higher than that of the structure determined by proton NMR would suggest (1.04×10^4 g mol^{-1}). This might be due to the presence of a small amount of residual C_{18}–PEG–MI in the sample. This impurity would interfere with the estimation of the PNIPAAM and PAMPTMA(+) block lengths estimated from the NMR spectra, but not show up in the AFFFF measurements since the size of C_{18}–PEG–MI is significantly smaller than the pores of the membrane used in these experiments. It is also possible that even though the AFFFF experiments were conducted at a low temperature and a low polymer concentration, the formation of very small aggregates (di- or trimers) may interfere with the molecular weight determination.

Turbidity and cloud point experiments

The cloud point was determined from measurements of turbidity using a NK60 cloud point analyzer from Phase Technology, Richmond, British Columbia, Canada. This apparatus utilizes a scanning diffusive technique to characterize phase changes of the sample with high sensitivity and accuracy. The light beam from an AlGaAs light source, operating at 654 nm, was focused on the measuring sample that was applied onto a specially designed glass plate coated with a thin metallic layer of very high reflectivity (mirror). Directly above the sample, an optical system with a light-scattering detector continuously monitored the scattered intensity signal (S) of the sample as it was subjected to prescribed temperature alterations. The relation between the signal and the turbidity (τ) can conveniently be expressed by the following empirical relationship as explained in ref. 26, $\tau(S) = 9.0 \times 10^{-9} S^{3.751}$. Here τ will be in units of cm^{-1} and S is the numerical output from this cloud point analyzer.

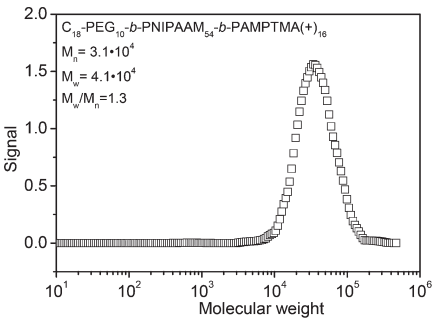

Fig. 2 The molecular weight distribution curve of C_{18}–PEG_{10}-*b*-PNIPAAM$_{54}$-*b*-PAMPTMA(+)$_{16}$ in a dilute aqueous solution (0.1 M NaCl) at 10 °C by means of AFFFF.

The incorporation of SDS into the copolymer solution (0.5%) was followed by a temperature-controlled Helios Gamma (Thermo Spectronic Cambridge, UK) spectrophotometer at a wavelength of 500 nm. The registered absorbance of the samples is an indirect measure of the turbidity of the solution.

Small angle neutron scattering (SANS)

Small-angle neutron scattering (SANS) experiments were carried out with the SANS installation at the JEEP II reactor, Kjeller, Norway. The wavelengths used were 5.1 and 10.2 Å, with a resolution ($\Delta\lambda/\lambda$) of 10%. The q range employed in the experiments was 0.008–0.25 $Å^{-1}$, where $q = (4\pi/\lambda)\sin(\theta/2)$ and θ is the scattering angle. The samples were filled in 2 mm Hellma quartz cuvettes (with stoppers), which were placed onto a copper base for good thermal contact and mounted on the sample chamber. The space between the sample and the detector was evacuated to reduce air scattering. In all the SANS measurements, D_2O was used as a solvent instead of light water to obtain a good contrast and low background for the neutron-scattering experiments. In addition, the deuterated version of the SDS (d-SDS) was employed in some experiments in order to mask the contribution from the surfactant to the scattering signal. Standard reductions of the scattering data, including transmission corrections, were conducted by incorporating data collected from an empty cell, a beam without a cell, and a blocked-beam background. The data were finally transformed to an absolute scale (coherent differential cross-section ($d\Sigma/d\Omega$)) by calculating the normalized scattered intensity from direct beam measurements. The measurements were performed at 25 °C and 50 °C on 1 wt% solutions of the copolymer $C_{18}PEG_{10}$-*block*-NIPAAM$_{54}$-*block*-(AMPTMA(+))$_{16}$ in D_2O and with SDS/d-SDS. The concentration of 1 wt% was employed in order to obtain a sufficient signal–noise ratio in the SANS measurements, and to simultaneously keep the concentration sufficiently low to ensure weak interactions between the different coacervate particles in solution.

Dynamic light scattering

The dynamic light scattering (DLS) experiments were conducted with an ALV/CGS-8F multidetector compact goniometer system, with 8 fiber-optical detection units. The beam from a Uniphase cylindrical 22 mW HeNe-laser, operating at a wavelength of 632.8 nm with vertically polarized light, was focused on the sample cell (10 mm NMR tubes, Wilmad Glass Co., of highest quality) through a temperature-controlled cylindrical quartz container (with two plane-parallel windows), which was filled with a refractive index matching liquid (*cis*-decalin). A standard cleaning procedure for the light scattering cells was followed, where they were first immersed in a detergent solution for one night, subsequently rinsed in Milli-Q water, and then steamed by ethanol for 40 minutes. Before steaming, the cell was covered with aluminum foil. All samples were prepared in a dust-free environment by employing syringes with attached 0.8 μm filters (Millipore).

The scattered light was detected at scattering angles of 22° to 141°, corresponding to a scattering vector regime of 5.0×10^{-3} $nm^{-1} < q < 2.5 \times 10^{-2}$ nm^{-1}. The measured intensity correlation

function $g^2(q, t)$ can be related to the theoretically amenable first-order electric field correlation function $g^1(q, t)$ by the Siegert relationship,[27] $g^2(q, t) = 1 + B|g^1(q, t)|^2$, where B is usually treated as an empirical factor. In this work, $B > 0.8$ for all considered systems and these values are close to the theoretical value. It was found that the decays of the 0.05 wt% samples were generally well described by a single exponential followed at longer times by a stretched exponential:

$$g^1(t) = A_f\exp(-t/\tau_f) + A_s\exp[-(t/\tau_{se})]^{\beta} \quad (1)$$

with $A_f + A_s = 1$. The decays of the correlation functions of the 0.5 wt% samples exhibited only one relaxation mode, and could be described as:

$$g^1(t) = \exp[-(t/\tau_{se})]^{\beta} \quad (2)$$

The fitted parameters at a scattering angle of 90° can be found in the ESI.† The variables τ_f and τ_{se} are the relaxation times characterizing the fast and the slow relaxation process, respectively, and the parameters A_f and A_s are the corresponding amplitudes. The results from the analyses of the correlation functions showed that for the 0.05 wt% samples the first term (short-time behavior) of $g^1(t)$ was q^2-dependent and thus associated with the mutual diffusion coefficient D_m ($\tau_f^{-1} = D_m q^2$), which in dilute solutions probe the diffusion of single entities or small clusters. If we assume that the species are sphere-like, the apparent hydrodynamic radius $R_{h,f}$ can be determined in the dilute concentration regime from the mutual diffusion coefficient *via* the Stokes–Einstein relationship $D_m = k_B T/6\pi\eta_0 R_{h,f}$, where k_B is the Boltzmann constant, T is the absolute temperature, and η_0 is the solvent viscosity. The second term (long-time behavior) of $g^1(t)$ in dilute solutions is associated with the diffusion or dynamics of large complexes and relaxation of chains or clusters.[28] The variable τ_{se} is the effective relaxation time, and β ($0 < \beta \leq 1$) is a measure of the width of the distribution of relaxation times. The mean relaxation time for the slow mode is given by $\tau_s = \Gamma(1/\beta)\tau_{se}/\beta$, where $\Gamma(1/\beta)$ is the gamma function of $1/\beta$. The slow mode (τ_s) was found to have a q-dependence that was somewhat larger than two (in the range 2–3), and in addition the relaxation times indicate that $qR > 1$ for some of the systems. Even though accurate sizes cannot be determined under these conditions, the general trends should be reliable. We have therefore chosen to represent the slow mode as an apparent hydrodynamic radius, $R_{h,s}$ ($\tau_s^{-1}/q^2 = k_B T/6\pi\eta_0 R_{h,s}$). In the analysis of the correlation function data, a nonlinear fitting algorithm was employed to obtain best-fit values of the parameters A_f, τ_f, τ_{se}, and β.

Zeta-potential

The electrophoretic mobilities of the samples were measured with a Malvern Zetasizer Nano ZS (Malvern Instruments, Malvern, UK). The measurements were performed at 20 °C and 50 °C by using the internal thermoelectric elements. To measure the mobility of the particles, both slow and fast, field reversal was applied to the sample, and the motion of the particles was detected by phase analysis light scattering. The sample cell used was a dip-cell for aqueous solutions. The value of the zeta potential (Z) was calculated from the measured electrophoretic mobility (U_E) *via* the Henry equation[29] $U_E = 2\varepsilon Z f(\kappa a)/3\eta$, where ε is the dielectric constant, η is the viscosity and $f(\kappa a)$ is Henry's function.

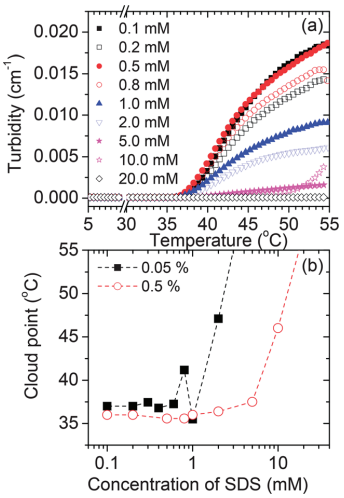

Fig. 3 (a) Change of turbidity *vs.* temperature of a 0.5% copolymer–water solution with SDS at the surfactant concentrations indicated. (b) Cloud point (CP) values of the 0.5% and 0.05% copolymer solution as a function of the concentration of SDS. The error in the cloud point determination is estimated to be ±0.5 °C.

Results and discussion

Turbidity and cloud point

The turbidity was first measured for the *pure* copolymer solutions at concentrations of 0.05% and 0.5% as a function of temperature. The cloud point (CP), measured as the point of initial rise in turbidity, was determined to be 37 °C and 36 °C for the 0.05% and 0.5% system, respectively, by means of the setup described earlier. Note that for the low concentration of 0.05%, the changes were very small and no sign of clouding could be detected by visual inspection alone. The cloud point is a useful probe here since it is a manifestation of the state where structures are formed – sufficiently distinct from the surrounding water – to be able to produce scattered light. For the block copolymer employed in this study, the *temperature-induced* formation of such structures is principally due to the PNIPAAM block, which shows a dominant sticky character at elevated temperatures. The slight difference in CP observed between the two concentrations is thus attributed to the increased probability (per unit time) of creating such structures in the 0.5% system compared to the lower concentration. With the addition of SDS, the turbidity behavior was found to be strongly modified, as shown in Fig. 3a for a series of surfactant concentrations for the 0.5% system. Also, the initial rise in turbidity, *i.e.* the cloud point, is seen to change. In the discussion that follows, one should keep in mind that the concentration of SDS used is generally lower than the

critical micellar concentration (cmc), *i.e.* the value needed to create micelles in a pure solution (8.2 mM at 25 °C). The presence here of the block copolymer will, however, strongly modify the behavior of the system, and effects will occur at significantly lower concentrations of SDS.

The evolution of the cloud point, as extracted from turbidity measurements for the two samples, is presented in Fig. 3b. We should note that with the employed experimental setup (*cf.* Materials and methods section) a very precise determination of the cloud point is possible, as well as a very accurate control of the temperature. At the lower SDS concentrations, only a slight difference in CP – approximately the 1 °C difference mentioned above – can be noticed between the two different concentrations of the block copolymer. However, for the 0.05% copolymer solution, a rise in CP is seen to commence around 0.8 mM of SDS, followed by a large drop at 1.0 mM. The drop is as much as 5 °C, and this feature shows that at this concentration of surfactant, there is a significant *increase* in the probability of creating compacted domains. As will be shown from zeta potential data in the next section, this is related to charge neutralization in the system, *i.e.*, the electrostatic repulsion that generally acts against attractive interaction at this point is no longer present. Furthermore, these observations are in line with results from DLS measurements that will be discussed later. For SDS concentrations higher than 1 mM the CP is seen to rise strongly, an effect that is due to the recharging of the assemblies by the negatively charged SDS when it is adsorbed to the complexes. Finally, at 20 mM any sign of microphase separation is totally suppressed, and the cloud point was not detectable in the temperature range of the investigation.

Such fine details in the evolution of the cloud point are not seen for the 0.5% copolymer solution. In this case the value of the cloud point is only slightly affected by SDS addition up to about 5 mM, after that a strong rise of the cloud point is found. The reason for this delayed effect is related to the correspondingly larger amount of SDS that is needed for recharging the copolymer complexes when the concentration of the polymer is 10 times higher.

Zeta potential

To further elucidate the interaction between the block copolymer and SDS, zeta-potential as well as absorbance measurements were performed. These results are presented in Fig. 4. For the 0.05% copolymer solution only the zeta-potential is presented, since no significant absorbance change could be detected. The measurements were made at 25 °C and 50 °C, *i.e.*, below and above the cloud point. For the *pure* copolymer solution (without SDS addition), the zeta potentials were found to be 59 and 74 mV at 25 and 50 °C, respectively. A slight decrease in the zeta potential could be observed already in the 0.01 mM SDS solution, which shows that the initial binding of SDS to the block copolymer actually starts at very low SDS concentrations. As the concentration of SDS rises, the binding of the negatively charged surfactant to the PAMPTMA blocks of the copolymer tends to neutralize the positive charges on the copolymer complex, and higher levels of SDS addition thus gradually lead to less positive values of the zeta potential, until it reaches zero. Upon further increase in the SDS concentration, a charge reversal takes place.

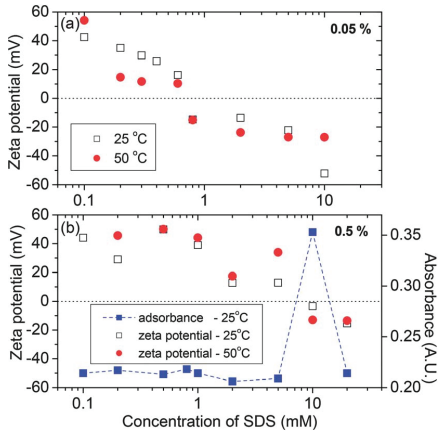

Fig. 4 Zeta potentials of SDS–copolymer complexes as a function of surfactant concentration at two temperatures. The concentrations of the copolymer were 0.05% (a) and 0.5% (b). The error in the zeta potential is approx. ±5 mV. In panel (b) the absorbance of the samples at 25 °C is displayed together with the zeta potential data.

This transition, referred to as the recharging point or the second critical aggregation concentration (cac2), is seen to be slightly below 1 mM of SDS for the 0.05% copolymer. Such charge reversal of the polymer–surfactant complex is generally due to the hydrophobic interaction between the tail of the surfactant and the neutral domains of the complex, showing a monotonic dependence on the concentration of polymer.[30] In Fig. 4b, we may observe that the charge-neutralization point is at 10 mM of SDS for the 0.5% copolymer, thus exactly ten times higher than the value for the 0.05% copolymer solution, as one would expect if this association is linear with concentration. Furthermore, the variation in absorbance for the 0.5% copolymer solution shows results consistent with those from the zeta-potential measurements. The charge neutralization leads to the formation of compacted aggregates at 10 mM of SDS, as seen from the peak in the absorbance data, an effect which is due to the elimination of electrostatic repulsion in the system. This parallels the pronounced compaction observed from the DLS data for this polymer concentration (*cf.* Fig. 10). Then, with a further increase in the SDS concentration, the recharged complexes dissolve in the solution, and the absorbance drops back to the original value. From this behavior, one may expect that there should also be a variation in the CP for this system around 10 mM. This was, however, not detected (*cf.* Fig. 3b), possibly because it is masked by the very large overall change in CP occurring at the higher concentrations of SDS.

Such redissolution of polymer–surfactant complexes as mentioned above has been observed in various polymer–surfactant systems. One observation is that the concentration of the surfactant at the onset of redissolution is usually near the critical micellar concentration.[31,32] However, in some other systems, the redissolution of the complexes could not be observed for concentrations above cmc. The redissolution process is now well understood in general terms,[33–35] but the structure of the redissolved species for a particular system and specific details of the

process are interesting topics of investigation. In our system we can observe in the 0.5% copolymer solution that cac(2) is higher than the cmc of SDS at 25 °C.

If we consider the effects of changing the temperature, the data seem to indicate a slightly larger reduction in the zeta potential at 50 °C than at 25 °C for a given SDS concentration (Fig. 4a). This behavior may be related to the surfactant becoming more strongly bound at higher temperatures. Since the hydrophobicity of the PNIPAAM block increases with temperature, this may contribute to an enhanced attractive interaction between the copolymer and the SDS tails, and facilitate charge neutralization. However, any systematic effect in this respect could not be detected for the higher polymer concentration (0.5%).

Small-angle neutron scattering (SANS)

Fig. 5a presents the SANS data for the copolymer solution with and without 20 mM SDS measured at 25 °C and 50 °C. Let us first consider the pattern for the pure copolymer (no SDS) at 25 °C (open squares). The plateau observed at low q is a clear sign of the presence of nano-sized entities in this system, with a characteristic size roughly on the order of $1/q_c$, where q_c is the q-value of the start of the plateau. This is seen to occur at approx. 0.02 Å^{-1}, thus already from visual inspection of the data one can estimate that these particles have a characteristic size of some tenths of Angstroms (a more detailed analysis follows below). Based on the structure of the copolymer (see Scheme 1), it is to be expected that in an aqueous environment these chains will assemble into micelles, with the hydrophobic groups (specifically C_{18}) in the core and the hydrophilic groups (*e.g.* PAMPTMA) at the surface. The SANS data for the pure copolymer therefore comply well with this model.

In the absence of SDS these micelles will be highly charged on the surface. In order to minimize the energy from the electrostatic interaction the charges will therefore contribute to an open corona around the micellar core. At a copolymer concentration of 1% as used here, one should therefore expect a measurable interparticle interaction between the micelles in solution. This is also what we find from the data. Assuming spherical micelles, the data were fitted with a core–shell model with a structure factor as developed by Hayter *et al.*,[36,37] where the Coulomb interaction is included. The fitting for the pure block copolymer is shown in Fig. 5b, and gives an overall radius of 41 Å or a diameter of 82 Å. The pure form factor for this micelle, *i.e.*, the modeled data assuming no interparticle interaction, is also plotted in Fig. 5b. This demonstrates how the electrostatic interactions strongly affect the SANS pattern at low q-values. Considering the chemical structure of the block copolymer as well as the presence of charges on the micellar surface, the corona is likely to be highly solvated at 25 °C, and thus gives very little contrast with respect to the surrounding water (D_2O).[38] The radius obtained from the SANS modeling therefore represents the size of the *core* of the micelles.

We now consider the system where the block copolymer is mixed with SDS at 25 °C (open circles in Fig. 5a). The amount of SDS used here (20 mM) corresponds to the point of charge neutralization for a 1% concentration of copolymer (*cf.* zeta-potential data in the previous section, where a 0.5% copolymer shows charge neutralization at 10 mM). This mixed system is

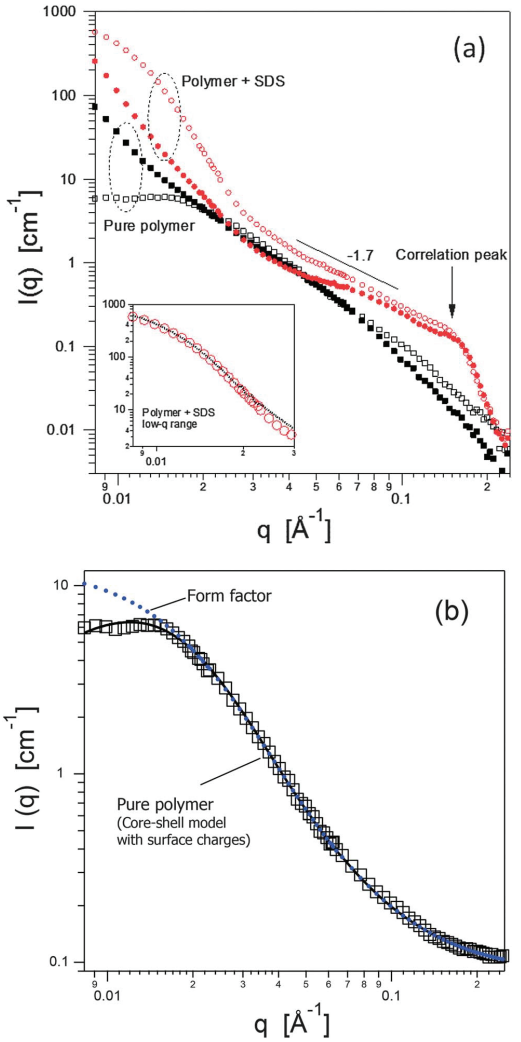

Fig. 5 (a) Scattered intensity *vs.* q for the pure copolymer samples (squares) and copolymer with 20 mM SDS (circles). The copolymer concentration was 1 wt%. The open symbols represent results at 25 °C and filled symbols represent results at 50 °C. The coherent background (high-q limit) has been subtracted from the data here in order to show better the high-q features. The inset shows a low-q model fit for the copolymer–SDS system at 25 °C. (b) Core–shell model with screened Coulomb interaction fitted to the scattering curve (including coherent background) for the pure copolymer solution at 25 °C. The dotted curve shows the contribution from the particles assuming no inter-particle interaction, *i.e.* the form factor alone.

seen to behave quite differently from the copolymer without surfactant addition. The additional scattering at low q-values demonstrates that the structures of the block copolymer–SDS mixtures are significantly larger than the micelles made from the copolymer alone. Due to the absence of a low-q plateau it is not

possible to get exact values for the core size here, but an estimate can be obtained from a best fit (core–shell model) to the low-q scattering, as shown in the inset of Fig. 5a. Here an approximate core radius of 190 Å (19 nm) was obtained, corresponding to a diameter of 380 Å. A Guinier regression fit (not shown here) gave a similar value. This is a size nearly five times larger than that found for the pure copolymer micelle (82 Å). Thus it is clear that when the charges on the copolymer become neutralized by the surfactant, the copolymer together with SDS is able to create large, stable polymer–SDS complexes for this system.

An important feature of the copolymer–SDS scattered intensity pattern – not present for the pure copolymer – is the peak observed at 0.15 $Å^{-1}$. This q-value corresponds to a short and well-defined repeating distance in the system, equal to $2\pi/q = 42$ Å. Depending on the actual block copolymer used,[6] the peak can be highly distinct or somewhat less defined, as here. The latter is due to it being superimposed by the power-law scattering coming from the particle corona (see discussion below). Such a correlation peak can, at high q, only appear if there is a tight packing of well-defined small objects, and as demonstrated by Berret *et al.*, the peak is a fingerprint of micelles that are closely packed in the core of the mixed copolymer–surfactant structure. The repeating distance found here, *i.e.* 42 Å, is just slightly larger than the SDS micellar diameter of 36 Å reported in ref. 39. Very recent simulation work by Lebard *et al.*[40] reports radii of gyration that would be equivalent to a range of diameters from 33 Å to well above 40 Å. In any case, this shows that the SDS micelles in our system are compactly organized in the coacervate core, possibly with a small average distance between them (approx. 6 Å if we compare our results with the data in ref. 39). Since the SDS micelles are stabilized in the core by the oppositely charged PAMPTMA blocks of the copolymer, this distance is then likely to be what is necessary for properly accommodating the polymer inside the coacervate core.

One important observation here is that since the PAMPTMA end of the copolymer is now located in the core of the micelles together with the other end (alkane group) that initiated the micelle formation, we have obtained a coacervate particle where the solvated part of the copolymer must bend back on itself, forming loops on the surface (corona) of the particles, *cf.* also the schematic illustration given at the end of the article (Fig. 11), that will be commented on later.

As mentioned earlier, the SANS scattering is dominated by the core of the micelles, but the polymer segments of the corona will give a measurable contribution at medium/high q-values where the signal from the core is low. This scattering will follow a $q^{-1/\nu}$ behavior, where ν is the Flory exponent. For an extending chain that obeys Gaussian statistics, ν equals 1/2,[41] thus a q^{-2} decay would be expected, whereas for chains in a good solvent ν equals 3/5, meaning that the decay should follow $q^{-1.67}$. For the copolymer–SDS sample at 25 °C, we observe in the SANS data a slope of −1.7 in the mid q-range (to the left of the correlation peak), which thus fits very well with the assumption mentioned earlier that the corona of the coacervate consists of highly solvated copolymer segments.

If we now compare the modeled size of the coacervate core (diameter $D_C = 380$ Å) with that of the average distance spanned by one SDS micelle taking into account that they experience a small separation as noted above ($D_M = 42$ Å), we may obtain an estimate of the average number of micelles inside the core as $\phi(D_C/D_M)^3$, where ϕ is the volume fraction of micelles within the core. The tightest possible random packing of spheres in 3 dimension has ϕ equal to 0.63,[42] but for typically densely packed system values below 0.5 can be expected. If we assume here that ϕ has a value around 0.5, we obtain a rough estimate of the number of micelles in the core equal as $0.5(380/42)^3 = 370$. This is likely to be an upper limit, but it is clear that for this system a significant number of micelles assemble together with copolymer chains to form one modified coacervate core. It should be noted that other authors have also found such large numbers of micelles (several hundreds) to be assembled into the core of C3Ms.[8]

Concerning the data at high temperature (filled symbols in Fig. 5a), a steep low-q scattering is observed for both the pure copolymer and the copolymer–SDS systems, with no sign of a plateau within the q-range accessible here. This is most likely due to the strong effect of hydrophobic associations for the PNIPAAM blocks at this temperature, well above the LCST. The PNIPAAM blocks create a dehydrated and compacted layer on top of the coacervate core, thus reducing the overall size of the particles, but at the same time giving a good contrast with respect to the surrounding water and effectively increasing the size seen by SANS. This corresponds well with results from DLS (discussed later), where a reduction in overall size (hydrodynamic radius) is seen upon a temperature increase from 25 to 50 °C.

In order to mask the contribution from the SDS in the copolymer–SDS complexes, additional SANS experiments were performed using deuterated SDS (d-SDS) and compared with hydrogenated SDS of the same concentration. A corresponding concentration of block copolymer (0.1%) around charge neutralization was employed here. These results are presented in Fig. 6a. Although the SANS signal quality is reduced due to the low concentration, as expected we observe that the scattered intensity for the SDS sample is higher than for d-SDS in most of the q-range. For the sample with d-SDS, where the only contribution to the contrast comes from the copolymer, the signal at 25 °C is very weak, about 0.6 cm^{-1} at the lowest q. This shows that the main contributor to the SANS signal is the SDS micelles, which is not surprising since they make up a large portion of the core.

When the temperature increases to 50 °C we observe the same behavior for both the d-SDS and SDS sample as was seen with the 1% copolymer concentration at high temperature (Fig. 5a). There is also now a strong excess low-q scattering from the copolymer when the temperature is well above the cloud point. Thus, the temperature induced association due to interaction between the hydrophobic PNIPAAM polymer segments now dominates over the scattering from the surfactant since both the d-SDS and SDS sample rise equally strongly at low q.

It is also of interest to see if there is any dependence on the amount of surfactant present. Therefore, Fig. 6b shows the samples with 5 mM and 10 mM of d-SDS at 25 °C, in addition to the 1 mM sample. Although the data are noisy due to the masked contribution from the surfactant, it is clear that the three d-SDS samples practically overlap at low temperature. Since with d-SDS only the contribution from the copolymer can be detected, the overlap of the three d-SDS curves indicates that no drastic changes occur in the polymer structure upon addition of surfactant in this concentration regime of copolymer and

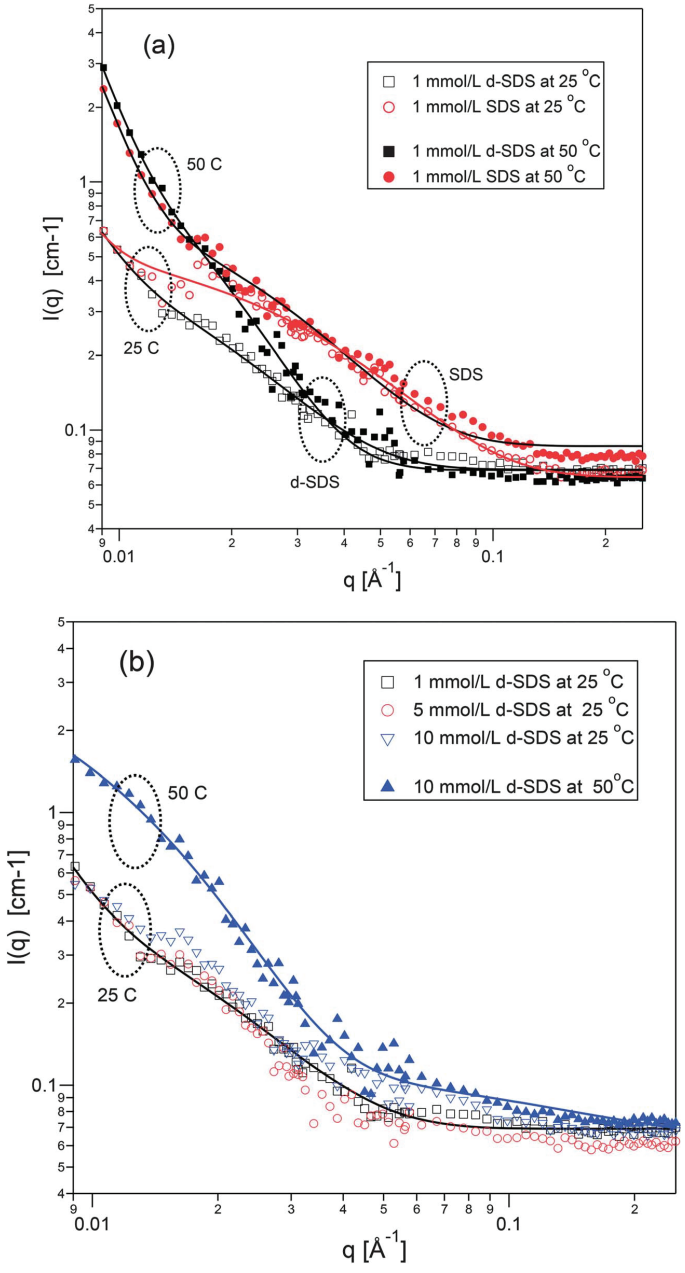

Fig. 6 (a) Scattered intensity *vs. q* for a 0.1% copolymer solution with 1 mM of SDS or d-SDS at 25 °C and 50 °C. (b) Scattered intensity *vs. q* for 0.1% copolymer solutions with 1, 5, and 10 mM of d-SDS at 25 °C, as well as 10 mM of d-SDS at 50 °C. The continuous lines are guides for the eyes. The dashed ovals around the data points mark data that are collected at the same temperature (25 or 50 °C), or with the same surfactant type (SDS or d-SDS), as indicated by the accompanying label.

surfactant. In Fig. 6b, one of the d-SDS samples (10 mM) is shown also at 50 °C. As for the 1 mM system at high temperature (*cf.* Fig. 6a), there is also now excess low-q scattering compared to the 25 °C pattern due to the hydrophobic interactions in the system. However, for 10 mM (Fig. 6a) there are indications of a low-q plateau being formed, which indicates that the presence of large amounts of surfactant (*ca.* 5 times the charge neutralization level) helps to maintain the copolymer in individual micelles, thus avoiding to some extent the intermicellar aggregation.

Dynamic light scattering (DLS)

Fig. 7 presents the results from DLS measurements at both 25 °C and 50 °C for 0.05% block copolymer solutions with varying amounts of SDS added.

At this low copolymer concentration, the correlation functions could be described by a sum of a single exponential function and a stretched exponential at longer times, $g^1(t) = A_f\exp[-t/\tau_f] + A_s\exp[-(t/\tau_{se})^{\beta}]$, see Materials and methods section. The first term represents the dynamics of unimers/micelles, whereas the second term probes the dynamics of larger complexes. It is evident that the tail of the correlation function is shifted to longer or shorter times, depending on the surfactant concentration but we may particularly note that the slowest decay is observed for the system with 1.0 mM SDS. As shown earlier, this value corresponds to the point of charge neutralization for a 0.05 wt% copolymer concentration, and thus fits well with the observation that compacted domains are created at this point (*cf.* discussion related to the turbidity and zeta potential data).

The apparent hydrodynamic radii as calculated from the DLS data as a function of the amount of SDS present are displayed in Fig. 8.

We first consider the behavior for the apparent hydrodynamic radii determined from the *fast* relaxation mode. At both temperatures, $R_{h,f}$ first decreases and then passes through a maximum at intermediate surfactant concentration. Our conjecture is that at 25 °C this is related to single copolymer molecules (unimers) that initially shrink because of the decrease in charge density as the oppositely charged SDS is added, and when charge neutralization is approached some unimers self-associate. Upon further addition of SDS, charge reversal occurs and disaggregation is observed.

At 50 °C, the hydrophobically induced attraction between PNIPAAM blocks induce self-association between unimers even in the absence of SDS, thus producing an increase in the apparent $R_{h,f}$. When SDS is added, the size decreases because of screening of the electrostatic interactions. Subsequently, when charge neutralization is approached, enhanced self-association occurs and $R_{h,f}$ rises. As the level of SDS addition increases even further, the structures disassemble due to charge recharging and solubilization of hydrophobic moieties (*e.g.* the isopropyl groups of PNIPAAM).

The apparent hydrodynamic radii calculated from the *slow* relaxation modes exhibit a similar profile when the surfactant concentration increases. The corresponding values for $R_{h,s}$ around 100 nm at low and intermediate concentrations of SDS are likely to be related to the overall size of the coacervate particles, although few of these are expected to form at this low polymer concentration. From SANS measurements we observed *core* diameters close to 40 nm for the copolymer–SDS system, and as discussed earlier the *corona* of these particles is highly solvated and extends far into the solvent. Thus the hydrodynamic radius will be substantially larger than the core alone. This observation is in line with that of Berret *et al.*[6] in their work on PTEA-PAM–SDS systems, where hydrodynamic radii up to five times the size of the core were observed.

The values of $R_{h,s}$ are found to be lower at 50 °C than at 25 °C, which is due to the attraction between the PNIPAAM segments and subsequent dehydration in the complex. The more drastic transition observed around the charge neutralization (1 mM) at 25 °C than at 50 °C is probably due to the initially more loose structure at 25 °C, thus the changes upon contraction will be more dramatic.

The DLS results for the higher concentration of 0.5% block copolymer solution at 25 °C and 50 °C for the same series of SDS concentrations are shown in Fig. 9.

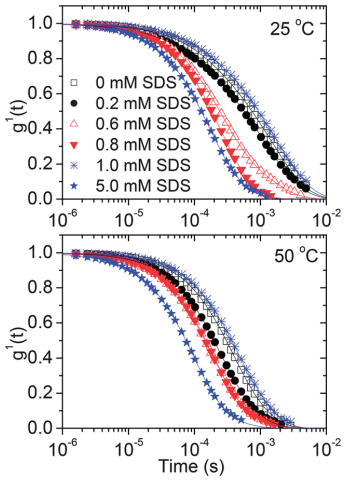

Fig. 7 Plot of the first-order field correlation function *versus* time for 0.05 wt% copolymer solutions at various levels of SDS addition and at the temperatures indicated. Every second data point is shown. The curves are fitted with the aid of eqn (1).

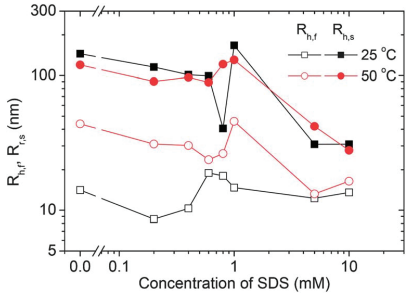

Fig. 8 Effect of surfactant addition on the apparent hydrodynamic radii determined from the fast ($R_{h,f}$) and the slow ($R_{h,s}$) relaxation mode at a copolymer concentration of 0.05 wt% and at two different temperatures.

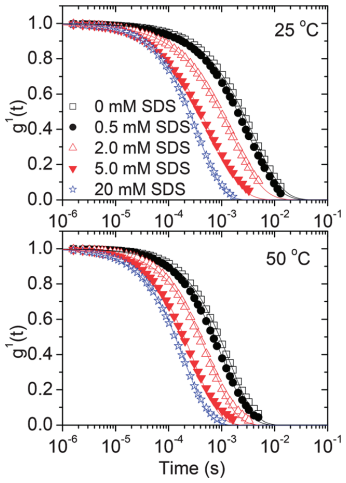

Fig. 9 Plot of the first-order field correlation function *versus* time for the 0.5 wt% copolymer solution at various levels of SDS addition and at the temperatures indicated. Every second data point is shown. The curves are fitted with the aid of eqn (2).

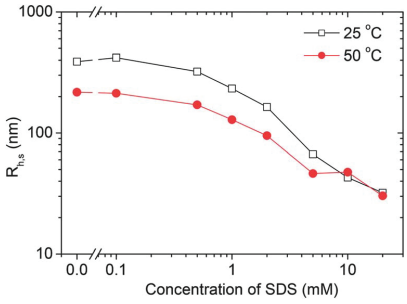

Fig. 10 Effect of surfactant addition on the apparent hydrodynamic radii determined from the decay of the correlation function at a copolymer concentration of 0.5 wt% and at two different temperatures.

These correlation functions exhibit a different behavior than the corresponding ones for the low copolymer concentration. At 0.5 wt%, coacervate complexes are easily formed and the decay of the correlation functions can be portrayed by a single stretched exponential (β = 0.8–0.9), indicating that there is a fairly narrow distribution of particle sizes in the system. The values for the hydrodynamic radius of the particles are found to increase somewhat compared to the lower copolymer concentration used (0.05%), probably since more copolymer is available for particle formation.

The apparent hydrodynamic radius $R_{h,s}$ drops with increasing surfactant concentration at both temperatures (Fig. 10), due to the same mechanism discussed earlier for the 0.05 wt% block copolymer concentration. At moderate surfactant concentrations the values of $R_{h,s}$ values are lower at 50 °C than the corresponding ones at 25 °C, due to the contraction of the PNIPAAM domains, similar to what was observed for the 0.05 wt% system. At the highest SDS concentrations, the data for the apparent hydrodynamic radii condense onto each other because the solubilization of hydrophobic microdomains due to the presence of SDS counteracts the hydrophobic contraction effect.

Conclusions

In summary, we have employed a specifically modified triblock copolymer to form complex coacervate particles (C3Ms) that bear some resemblance to the "flower-like" structures known to form from $C_nEO_mC_{n*}$ triblock amphiphiles. The C_{18} end-capped triblock copolymer initially forms micelles with a core consisting of the alkane chains, but upon addition of SDS there will be strong interactions between the AMPTMA end segments and the oppositely charged surfactant. This results in a co-assembled (coacervate) structure that was studied in a wide range of SDS concentrations by means of turbidity, zeta-potential, SANS, and DLS measurements. At 25 °C, a radius of 19 nm for the coacervate core was deduced from the SANS data. Furthermore, the data revealed the existence of compacted structures in the core, with a repeating distance of 4.2 nm, corresponding to the size of an SDS micelle plus the intertwined copolymer chain.

Fig. 11 presents a scheme to illustrate the possible evolution in the system upon addition of SDS. First, the unimers present in solution will tend to form micelles by self-assembly. The core of these micelles is small, with a radius of about 4.1 nm, but the

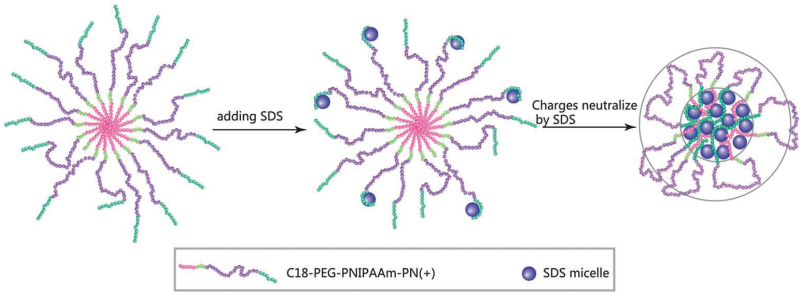

Fig. 11 Schematic illustration of the steps leading to formation of the coacervate structure.

corona is highly solubilized and extends far into solution, giving an overall apparent hydrodynamic radius of the micelles of about 100 nm. When the concentration of added SDS is higher than the critical aggregation concentration, SDS starts to co-assemble with the polyelectrolyte chains in the *corona*, and the hydrodynamic radius shows a slight decrease with SDS concentration due to the lowered Coulomb repulsion. If more SDS is added to the solution, the charges on the surface of the micelles will be neutralized, and the resulting hydrophobic coacervate will move to the core of the particle. The structure can then be stabilized by the neutral block of the corona. Moreover, in addition to the SDS micelles shown in the *core* in the schematic illustration, SDS will attach to the PNIPAAM segments of the corona, creating increasingly more thermodynamically stable particles upon further addition of surfactant.

Acknowledgements

This work is part of the SiteDel group activities. The authors also thank the Research Council of Norway for funds through the projects 191564/V30 and 190403. BN and KZ acknowledge financial support from Vista/Statoil for the project with the number 6506. WW thanks the School of Pharmacy for a post-doc position.

References

1 K. Kataoka, A. Harada and Y. Nagasaki, *Adv. Drug Delivery Rev.*, 2001, **47**, 113–131.
2 T. Hellweg, Block Copolymer Surfactant Mixtures in Aqueous Solution: Can we Achieve Size and Shape Control by Co-Micellization?, in *Self Organized Nanostructures of Amphiphilic Block Copolymers II*, Book Series: Advances in Polymer Science, 2011, Springer Berlin/Heidelberg, pp. 1–27.
3 L. Piculell and B. Lindman, *Adv. Colloid Interface Sci.*, 1992, **41**, 149–178.
4 P. Hansson, *J. Colloid Interface Sci.*, 2009, **332**, 183–193.
5 J. F. Berret, P. Hervé, O. Aguerre-Chariol and J. Oberdisse, *J. Phys. Chem. B*, 2003, **107**, 8111–8118.
6 J. F. Berret, B. Vigolo, R. Eng, P. Hervé, I. Grillo and L. Yang, *Macromolecules*, 2004, **37**, 4922–4930.
7 B. Hofs, A. de Keizer, S. van der Burgh, F. A. M. Leermakers, M. A. Cohen Stuart, P.-E. Millard and A. H. E. Müller, *Soft Matter*, 2008, **4**, 1473–1482.
8 I. K. Voets, A. de Keizer and M. A. Cohen Stuart, *Adv. Colloid Interface Sci.*, 2009, **147-48**, 300–318.
9 D. J. Yarusso and S. L. Cooper, *Macromolecules*, 1983, **16**, 1871–1880.
10 M. Annaka, K. Morishita and S. Okabe, *J. Phys. Chem. B*, 2007, **111**, 11700–11707.
11 J. F. Berret, O. Sandre and A. Mauger, *Langmuir*, 2007, **23**, 2993–2999.
12 A. Harada and K. Kataoka, *Macromolecules*, 1998, **31**, 288–294.
13 M. K. Yoo, Y. K. Sung, S. C. Chong and M. L. Young, *Polymer*, 1997, **38**, 2759–2765.
14 J. F. Berret, *J. Chem. Phys.*, 2005, **123**, 164703.
15 J. F. Berret, G. Cristobal, P. Hervé, J. Oberdisse and I. Grillo, *Eur. Phys. J. E*, 2002, **9**, 301–311.
16 L. M. Bronstein, S. N. Sidorov, V. Zhirov, D. Zhirov, Y. A. Kabachii, S. Y. Kochev, P. M. Valetsky, B. Stein, O. I. Kiseleva, S. N. Polyakov, E. V. Shtykova, E. V. Nikulina, D. I. Svergun and A. R. Khokhlov, *J. Phys. Chem. B*, 2005, **109**, 18786–18798.
17 S. Maiti and P. R. Chatterji, *J. Phys. Chem. B*, 2000, **104**, 10253–10257.
18 H. G. Schild, *Prog. Polym. Sci.*, 1992, **17**, 163–249.
19 M. Ciampolini and N. Nardi, *Inorg. Chem.*, 1966, **5**, 1150–1154.
20 S. Liu and S. P. Armes, *J. Am. Chem. Soc.*, 2001, **123**, 9910–9911.
21 N. Beheshti, K. Zhu, A.-L. Kjøniksen, K. D. Knudsen and B. Nyström, *Soft Matter*, 2011, **7**, 1168–1175.
22 A. Dedinaite, E. Thormann, G. Olanya, P. M. Claesson, B. Nyström, A.-L. Kjøniksen and K. Zhu, *Soft Matter*, 2010, **6**, 2489–2498.
23 A.-L. Kjøniksen, K. Zhu, R. Pamies and B. Nyström, *J. Phys. Chem. B*, 2008, **112**, 3294–3299.
24 A.-L. Kjøniksen, K. Zhu, G. Karlsson and B. Nyström, *Colloids Surf., A*, 2009, **333**, 32–45.
25 K. Zhu, H. Jin, A.-L. Kjøniksen and B. Nyström, *J. Phys. Chem. B*, 2007, **111**, 10862–10870.
26 A.-L. Kjøniksen, A. Laukkanen, C. Galant, K. D. Knudsen, H. Tenhu and B. Nyström, *Macromolecules*, 2005, **38**, 948–960.
27 A. J. F. Siegert, *Radiation Laboratory Report No. 465*, Massachusetts Institute of Technology, Cambridge, 1943.
28 K. L. Ngai, *Adv. Colloid Interface Sci.*, 1996, **64**, 1–43.
29 A. V. Delgado, F. González-Caballero, R. J. Hunter, L. K. Koopal and J. Lyklema, *Pure Appl. Chem.*, 2005, **77**, 1753–1805.
30 A. V. Svensson, L. Huang, E. S. Johnson, T. Nylander and L. Piculell, *ACS Appl. Mater. Interfaces*, 2009, **1**, 2431–2442.
31 I. Lynch, J. Sjöström and L. Piculell, *J. Phys. Chem. B*, 2005, **109**, 4258–4262.
32 J. Sjöström and L. Piculell, *Colloids Surf., A*, 2001, **183–185**, 429–448.
33 O. Anthony, C. M. Marques and P. Richetti, *Langmuir*, 1998, **14**, 6086–6095.
34 K. Thalberg, B. Lindman and G. Karlström, *J. Phys. Chem.*, 1991, **95**, 3370–3376.
35 S. dos Santos, C. Gustavsson, C. Gudmundsson, P. Linse and L. Piculell, *Langmuir*, 2011, **27**, 592–603.
36 J.-P. Hansen and J. Hayter, *Mol. Phys.*, 1982, **46**, 651–656.
37 J. Hayter and J. Penfold, *Mol. Phys.*, 1981, **42**, 109–118.
38 J. F. Berret, G. Cristobal, P. Hervé, J. Oberdisse and I. Grillo, *Eur. Phys. J. E: Soft Matter Biol. Phys.*, 2002, **9**, 301–311.
39 E. M. Woolley and T. E. Burchfield, *J. Phys. Chem.*, 1984, **88**, 2149–2155.
40 D. LeBard, B. G. Levine, P. Mertmann, S. A. Barr, A. Jusufi, S. Sanders, M. L. Klein and A. Z. Panagiotopoulus, *Soft Matter*, 2012, **8**, 2385–2397.
41 J. S. Pedersen and M. C. Gerstenberg, *Macromolecules*, 1996, **29**, 1363–1365.
42 C. Song, P. Wang and H. A. Makse, *Nature*, 2008, **453**, 629–632.

Appendix A

In situ SAXS furnace

Linkam TS1500 micro furnace with capillary heater

12/9/2011
MAX-Lab, I911
Henrik Mauroy

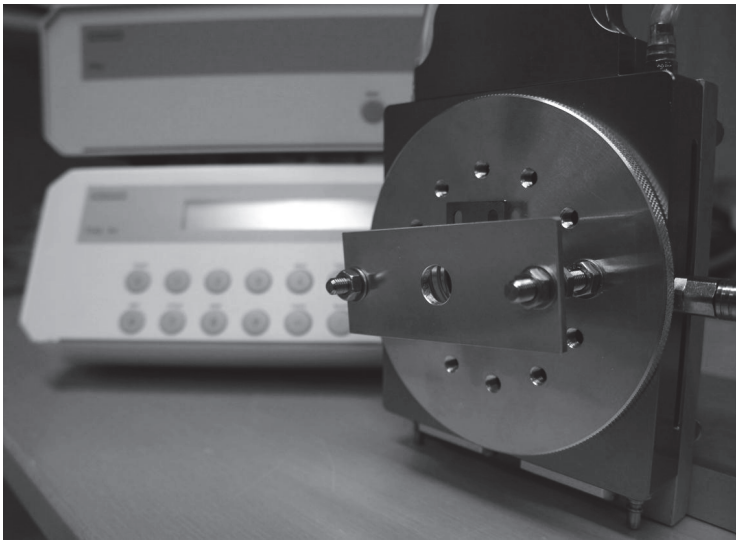

Contents

Introduction

The Linkam furnace is a high temperature heating-coil micro-furnace, operating in normal atmosphere. It has an integrated platinum-10% rhodium/platinum thermocouple inside which reads the temperature of the furnace to ± 1°C accuracy.

To be able to heat larger samples than what the furnace was intended for, a 25 gram copper block can be inserted into the furnace. The copper block is fixed with a clamp and a spring to lower the heat conduction to the surroundings. Figure 1 shows the complete set of parts with the Linkam furnace, base lid, sliding bracket and a spring connected to the copper block, and a mounting bracket. Because most of the copper block is situated outside the furnace the temperature of the copper block will be lower than the set-point of the furnace. The response is also lower. Different calibration ramps are found in the appendix.

With working temperatures of 100 °C, or higher, the Linkam furnace needs to be connected to water cooling.

Assembly

The two support screws are fastened to the base lid, which is then gently screwed onto the Linkam furnace (Figure 2). The sliding bracket is then fastened together with the spring to the copper block (Figure 2). Finally the mounting bracket is gently lowered on top of the spring, and fastened with the two support screws (Figure 3). Figure 4 show the complete setup mounted in the I911-4 SAXS-station at MAX-Lab.

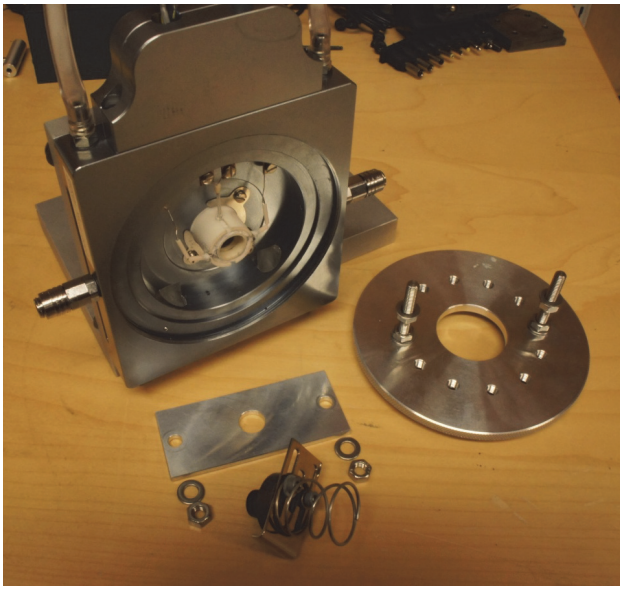

Figure 1: The Linkam furnace with the copper block assembly.

Figure 2: The copper block is inserted into the furnace.

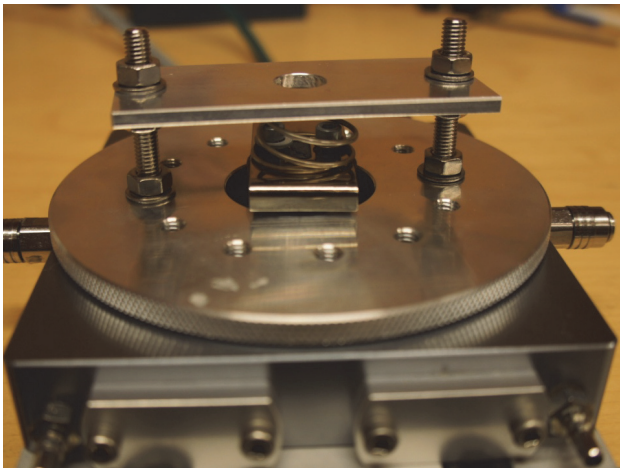

Figure 3: Mounting bracket securing the copper block to the Linkam furnace.

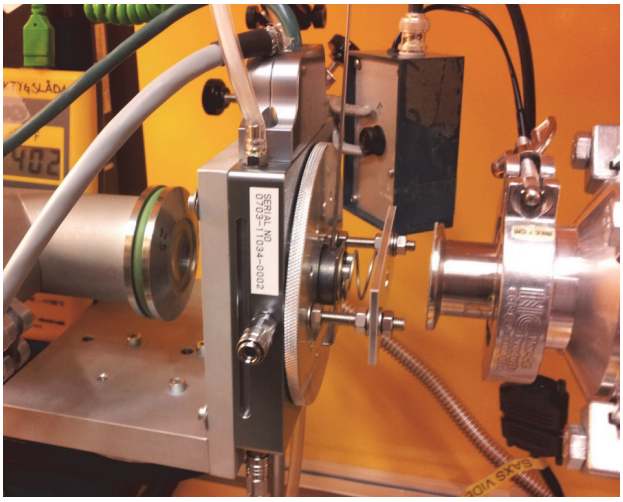

Figure 4: The modified Linkam furnace mounted in the I911-4 SAXS-station.

Specifications

Sample Size

The copper block can hold round capillaries up to 2 mm diameter. The position of the capillaries can be adjusted 12 mm with the sliding bracket connected to the copper block.

Heating/cooling rate

The maximum heating rate should never exceed 30 °C/min. The calibration is done with a heating rate of 30 °C/min. Maximum cooling rate should never exceed 10 °C/min to prevent damage to the furnace.

Maximum temperature

The furnace with copper block has been tested to 500 °C. At these temperatures the copper block oxidizes readily, and needs to be cleaned with sand paper after cooling. Any oxide will lead to lower heat conductivity between the base of the copper block and the bottom of the furnace.

Programming

The controller can hold up to 32 individual programs. They are run automatically in increasing order, always starting with program 1. A heating/cooling rate of zero will indicate the end of a profile.

Create/modify a program

Press RAMP and enter a number from 1-32. To change the heating/cooling rate, press RATE and enter a number between 0.1 and 30.

To change the temperature set-point, press LIMIT and enter a number between 0.1 and 500. 500 °C is the maximum temperature the modified furnace has been tested to.

To change the dwell time, press TIME and enter the desired time in minutes. The program will move to the next segment when the desired time has elapsed.

To save the program, press ENTER. The controller will then go back to the former activity; either the start screen, or back to the program which is running.

Start/stopping a program

To start the programs, press START. Pressing EXIT will stop the programs. To save the changes to the programs, press ENTER, or press EXIT one more time to discard any changes.

NB! If the furnace has a temperature of more than 300 °C while stopping, a cooling program with a cooling rate of 10 °C/min should be used to prevent damage to the furnace. For example if program 1 is running with a set-point of 350 °C, program 2 should be programmed like this: RATE of 10 °C/min, TEMP of 25 °C, and LIMIT 0 min.

Modify an executing program

A program can be changed while running. Press RATE to change the rate, press LIMIT to change the temperature set-point, or press TIME to change the dwell time. If the time is changed to zero, the controller will jump to the next program in the sequence, e.g. from program 1 to program 2.

To change another program while running, press RAMP and enter the desired program number. When finished changing the RATE, LIMIT and TIME parameters, press ENTER to save the changes.

Appendix

Temperature calibration performed with a heating rate of 30 °C/min.

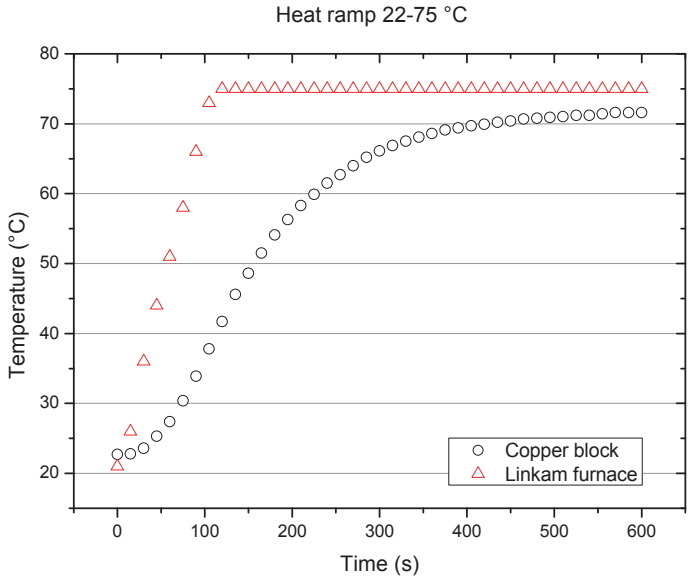

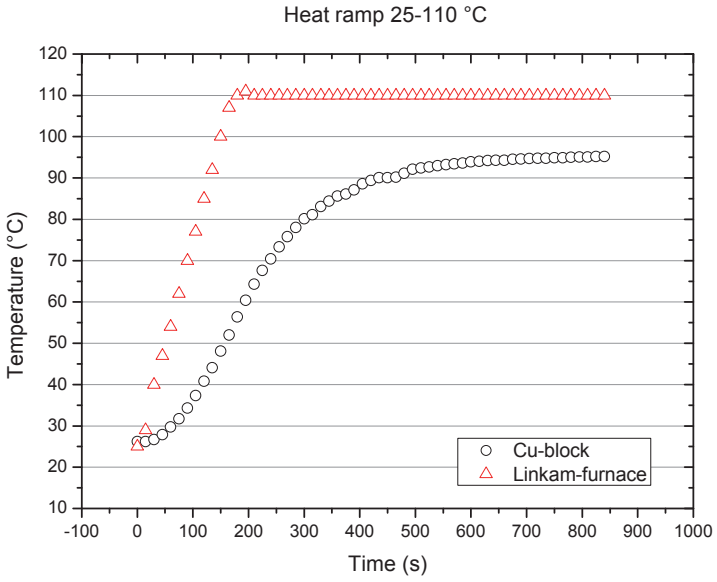

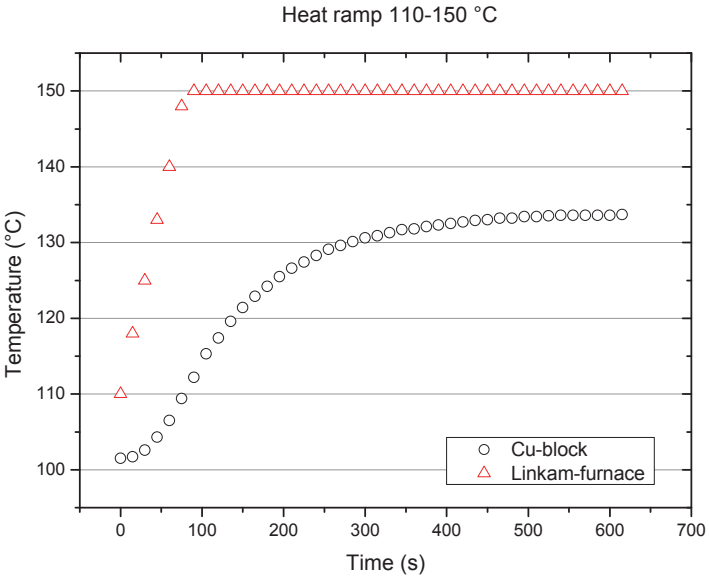
Heat ramp 110-150 °C
Temperature (°C)
Time (s)
Cu-block
Linkam-furnace
150
140
130
120
110
100
0
100
200
300
400
500
600
700

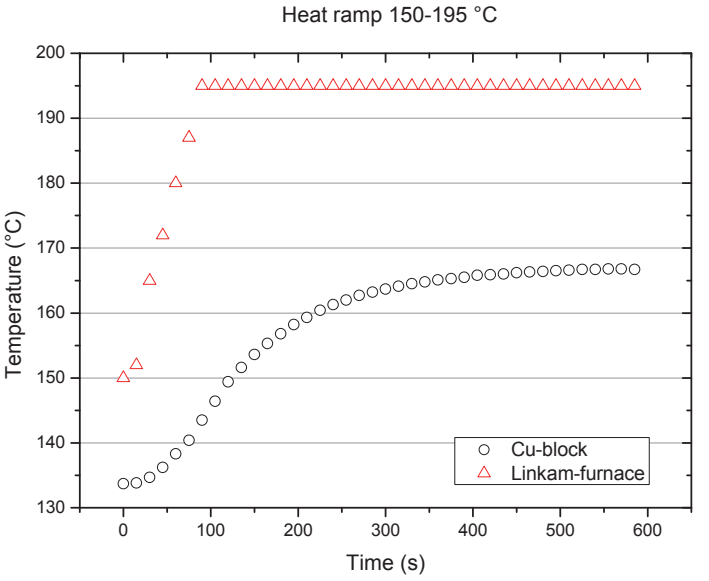
Heat ramp 150-195 °C
Temperature (°C)
Time (s)
Cu-block
Linkam-furnace
200
190
180
170
160
150
140
130
0
100
200
300
400
500
600

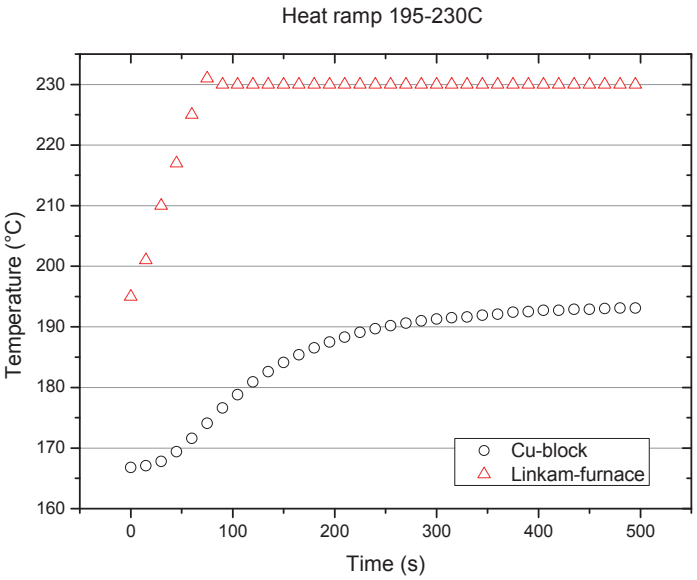
Heat ramp 195-230C
Temperature (°C)
Time (s)
Cu-block
Linkam-furnace
160
170
180
190
200
210
220
230
0
100
200
300
400
500

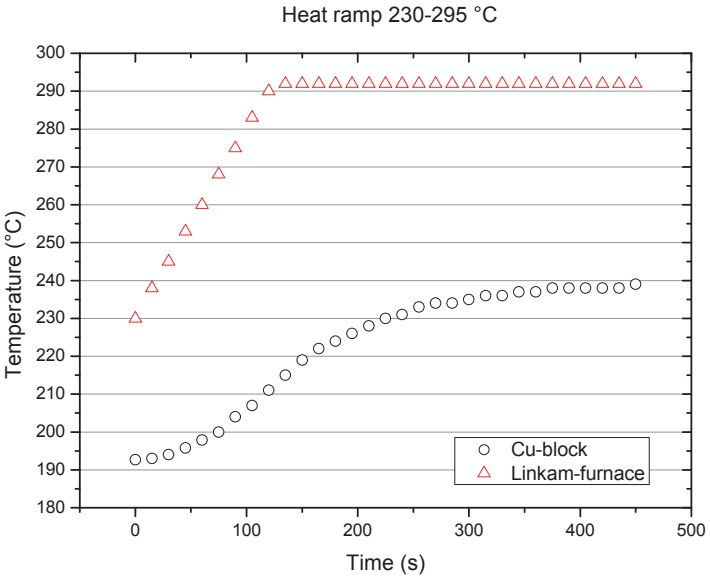
Heat ramp 230-295 °C
Temperature (°C)
Time (s)
Cu-block
Linkam-furnace
180
190
200
210
220
230
240
250
260
270
280
290
300
0
100
200
300
400
500

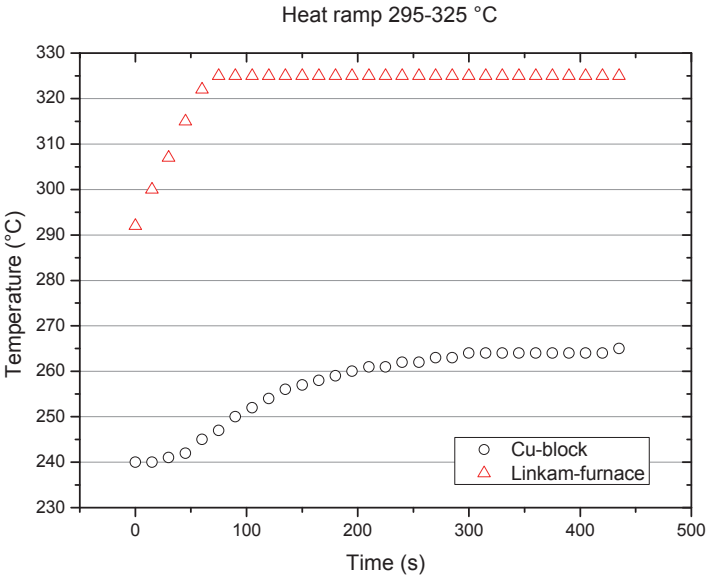
Heat ramp 295-325 °C
Temperature (°C)
Time (s)
Cu-block
Linkam-furnace

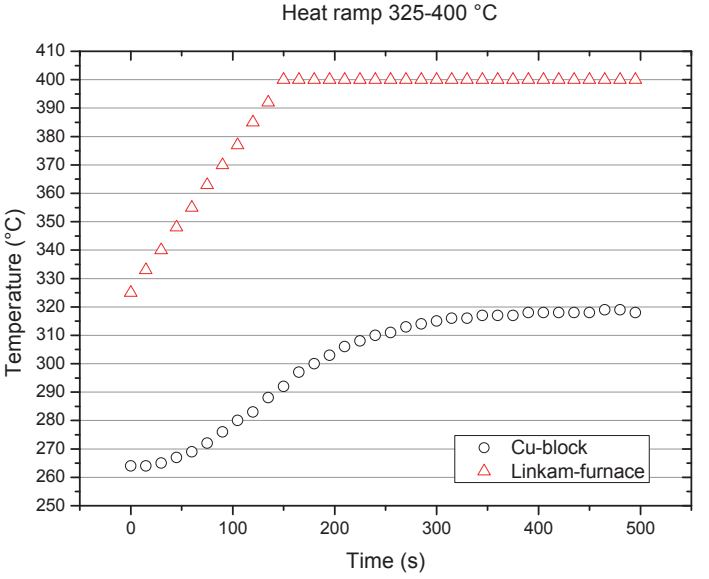
Heat ramp 325-400 °C
Temperature (°C)
Time (s)
Cu-block
Linkam-furnace

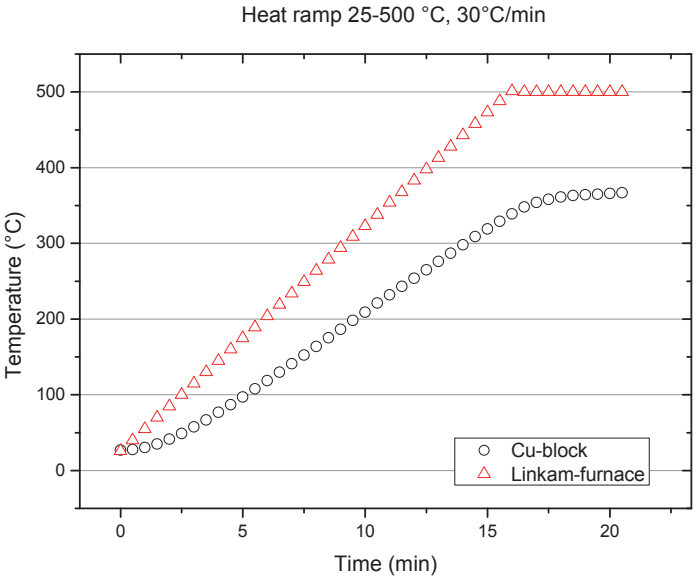

Temperature calibration performed with a heating rate of 10 °C/min.

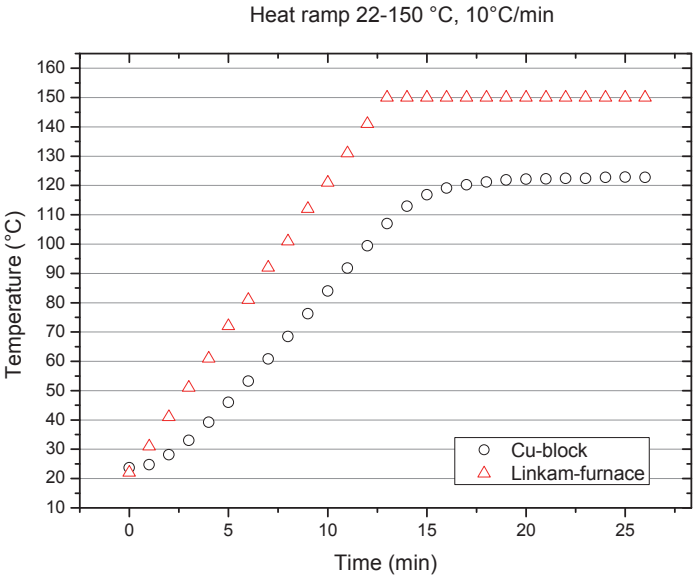

Appendix B

Matlab code: testGUI 5

The following code is a stripped down version of the main program, testGUI 5, which reads the input from a text file instead of from the graphical user interface. The full code would have been too lengthy to reproduce here, and it has thus been shortened to a minimalistic, but functioning code. It must be noted that several custom subroutines are used by the program to perform the actual data processing, and these, together with the full testGUI 5 code will be available from the author if requested.

```
function testgui5(foldername)
% Functioning stripped down code of testGUI 5
% The program reads an input file with the integration variables in stead
of
% getting them from the GUI. It then performs the integration and plots
the
% files according to their acquisition time.
%   Syntax: testgui5(foldername)
%
%   foldername = textstring with the full path of the folder
%   Example: testgui5('C:\matlab\work')

% The code uses several subroutines to function properly. Contact the
% author to receive the full code including all subroutines.

% Last Updated
% 19.06.2013
%
% Henrik Mauroy
% henrik.mauroy@ife.no

if isequal(nargin,0)
    error('No input arguments!')
end

%READS VARIABLES FROM A TEXT FILE ("cakevariables.mac")
inputfile = fullfile(foldername,'cakevariables.mac')
textexist = exist(inputfile); % Check if input file exists
if isequal(textexist,2)
    M=textread(inputfile,'%s'); % Reads the textfile
    cake.startazimuthvert  = str2double(M(2));
    cake.endazimuthvert    = str2double(M(3));
    cake.startazimuthhor   = str2double(M(4));
    cake.endazimuthhor     = str2double(M(5));
    cake.innerradius       = str2double(M(6));
    cake.outerradius       = str2double(M(7));
    cake.azimuthbins       = str2double(M(8));
    cake.radialbins        = str2double(M(9));
else
    error('No input file!');
end
```

```
extension = '';
datalist = '';
hdr_extension = '';
dointegrate = '';

%------------------------------------------------------------------------
%FILE INFO
tifflist=dir(fullfile(foldername,'*.tiff')); % MAX-Lab 911-4 scan files
hdrlist=dir(fullfile(foldername,'*.hdr'));   % MAX-Lab 911-4 header files
gfrmlist=dir(fullfile(foldername,'*.gfrm')); % NTNU Bruker Nanostar scan
files

%------------------------------------------------------------------------
%INTEGRATION PARAMETERS
params.maskthreshold=1;
integrationtype='CAKE';
macroname='maxlabCake.mac';         %name of the macro that shall be
generated by the matlabcreatemacro_cake
calibrationfile='fit2dcalib.log';   %name of the log file made when the
data was manually calibrated
params.maskfile='fit2d.msk';        %name of the mask file that was
manually created
params.subbkg = 'NO';               % YES, NO. Should backgroundfile be
used? Set in the GUI
params.scalewithionchamb = 'YES';   % NO, or YES. YES scales with
beamstop diode
params.applymask='YES';             % YES, NO, THRESHOLD (e.g.=1),
Threshold auto-masks pixels with a value
% lower than a set value. Ex: 100 masks all pixels with <100 counts

%------------------------------------------------------------------------
% CHECK OF INSTRUMENT TYPE
if ~isempty(tifflist)                % Max-Lab I911-4
    extension = '.tiff';
    datalist = tifflist;
    datalist=[19];
    hdr_extension = '.hdr';
    tiffsize= scansize(tifflist);     % Uses the subroutine SCANSIZE to
find the average size of the scan files
if isequal(tiffsize,8392704)
    params.xpixel = 79;            % Binning 2 of the scan files
    params.ypixel = 79;
elseif isequal(tiffsize,2101248)
    params.xpixel = 158;        % Binning 4 of the scan files gives 2x
bigger pixel size
    params.ypixel = 158;
elseif isequal(tiffsize,0)
    error('Multiple file sizes indicating different binning!'); % Aborts
due to different file types
end
    params.scanbins=1000;             %Resolution for the integration
(number of points along the radius)
elseif ~isempty(gfrmlist)             % NTNU Bruker Nanostar
    extension = '.gfrm';
    datalist = gfrmlist;
    datalist={datalist.name};
    params.xpixel = 105.2632;
    params.ypixel = 105.2632;
    params.scalewithionchamb = 'NO';     % Cannot scale this file type
because no header with info about beam intensity
```

```
    params.scanbins=500;
elseif isequal(extension,'')
    error('Nothing to integrate!');      % Aborts the program if there
are no scan files present
end

%-------------------------------------------------------------------------

% CREATES LISTS OF FILES THAT SHOULD BE INTEGRATED
% by checking against files that are already integrated)
chilistvert=dir(fullfile(foldername,'*_vert.chi')); % Reading and storing
all info of all vertically integrated files
chilisthor=dir(fullfile(foldername,'*_hor.chi'));   % Reading and storing
all info of all horizontally integrated files
chilistvert={chilistvert.name};                     % Creating a string
with all the _vert.chi names
chilisthor={chilisthor.name};
datalist=strrep(datalist,extension,'');             % strrep replaces the
extension in each object with a blank space ('')
chilistvert=strrep(chilistvert,'_vert.chi','');
chilisthor=strrep(chilisthor,'_hor.chi','');
integratedvert=intersect(datalist,chilistvert);     % intersect returns
the values common to datalist and chilistvert,
integratedhor=intersect(datalist,chilisthor);
dointegratevert=setdiff(datalist,integratedvert);   % Creates the final
list of files that should be integrated
dointegratehor=setdiff(datalist,integratedhor);

% Check if user only wants to integrate one set of data, e.g. a 360 deg
sector to integrate everything
if isequal(cake.startazimuthvert,cake.startazimuthhor)  % If the starting
angles are equal then only one direction will be integrated
    dointegratehor='';
end

%Check if the integration should be performed
dointegrate = 1;
if isempty(dointegratevert)         %Checking if the list is empty
    dointegrate = 0;
    if ~isempty(dointegratehor)     %Checking if the list is not empty
        dointegrate = 1;
    else
        error('Nothing to cake!');      % Aborts the program if all files
have been integrated
    end
end

% Getting beam center, distance, wavelength, and detector tilt from a
Fit2D log file
calibrationfilefullpath=fullfile(foldername,'fit2dcalib.log');
if ~exist(calibrationfilefullpath)
    dointegrate = '';
    error('No Fit2d log file!');    % Aborts if there is no log-file
else
    % Subroutine that reads the log file
    params=getvaluesfromfit2dlog(params,calibrationfilefullpath);
end

% Sorts the files according to acquisition time. It only works with files
that have information in separate header files
```

```
headerinfo = ''; % Creates the list so it can be checked later even if
it's empty
if isequal(extension,'.tiff') & ~isempty(hdrlist)
    for i=1:length(dointegratevert)  % puts on extensions on the names in
dointegrate list
        scan=sprintf('%s',dointegratevert{i},hdr_extension);
        dointegratevert{i} = scan;
    end
% Calls the headerread.m script to read headers, headerread outputs
several lists with information such as scan duration, time of data
acquisition etc.
    headerinfo = headerread(foldername,dointegratevert,hdr_extension);
    headertimes = headerinfo.scantime;   % extracs the date- and time-
list in the exact order as dointedograte
    sortedlist=sortdata(dointegratevert,headertimes);     % calls the
sortdata.m script to sort the dointegrate list
    % acording to data acquisition time
    dointegratevert = strrep(sortedlist,hdr_extension,'');   % Updates
the dointegrate-list
    hdrlist = sortedlist;    % Updates the header list which now gets the
same order as dointegrate
    for i=1:length(dointegratevert)  % puts on extensions on the names in
dointegrate list
        scan=sprintf('%s',dointegratevert{i},hdr_extension);
        dointegratevert{i} = scan;
    end
    % calls the function to read headers again for the sorted list
    headerinfo = headerread(foldername,dointegratevert,hdr_extension);
    dointegratevert = strrep(dointegratevert,hdr_extension,'');   %
deletes the extension
end

%-------------------------------------------------------------------------
% IF headerinfo IS EMPTY THE DEFAULT SCRIPT IS EXECUTED
if isempty(headerinfo)
    macro_def(foldername,macroname,datalist,extension,dointegratevert,...
    dointegratehor,params,integrationtype,cake);
else
macro_advanced(foldername,macroname,datalist,extension,...
dointegratevert,dointegratehor,params,integrationtype,cake,...
hdrlist,hdr_extension,headerinfo);
end

%-------------------------------------------------------------------------
%RUNNING THE MACRO IN FIT2D
fit2dpath='C:\matlabtmp\work\fit2d.exe';
system(sprintf('%s -dim5000x5000 -
mac%s',fit2dpath,fullfile(foldername,macroname))); %Opening Fit2d
disp('Done!');

% PLOTS ALL FILES IN THE FOLDER WITH plotFolderDef.m
plotFolderDef(foldername)  % Subroutine that plots all files and writes a
combined output file

end %END of program
```